Experimental Realisations of Energy Harvesters built from Quantum Dots and Quantum Wells

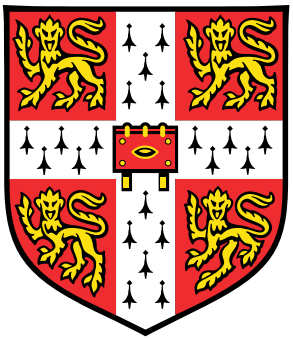

Gulizati Jialiele

Department of Physics

University of Cambridge

This dissertation is submitted for the degree of

Doctor of Philosophy

St.Edmund's College July 2019

Declaration

I hereby declare that except where specific reference is made to the work of others, the contents of this dissertation are original and have not been submitted in whole or in part for consideration for any other degree or qualification in this, or any other University. This dissertation is the result of my own work and includes nothing which is the outcome of work done in collaboration, except where specifically indicated in the text. This dissertation contains less than 60,000 words including appendices, bibliography, footnotes, tables and equations and has less than 150 figures.

Gulizati Jialiele
July 2019

Abstract

Title: *Experimental Realisations of Energy Harvesters built from Quantum Dots and Quantum Wells*.
Name: *Gulizati Jialiele*.

This thesis starts with an introduction to the background semiconductor physics required for carrying out this PhD research.

I have then presented the work that demonstrates, both theoretically and experimentally, an energy harvester built from two resonant-tunnelling quantum dots. A device, proposed by Jordan *et al.* [1], harvests energy from an area of $90\,\mu m^2$ of a two-dimensional electron gas (2DEG), using the energy-selective transport of electrons through a pair of quantum dots. It has proven to be an effective technique for harvesting energy at the micro/nano scales. Our energy harvester can generate a power of 0.13 fW in an estimated efficiency with a lower bound around $0.1\,\eta_C$. Our theoretical model (not affected by limitations of the Wiedemann-Franz law) suggests the actual efficiency to be about $0.5\,\eta_C$. Experimental observations of thermal power, voltage and efficiency at different values of I_{Heat} and R_{Load} have also been reproduced by this model. There are small quantitative differences between experimental results and theoretical modelling in terms of parameters, such as electrical temperatures and energy level difference. This may be explained by asymmetric barriers, accidental degeneracies or the lifetime-broadened width of the quantum dots, as well as charging effects in the non-linear regime. Overall, this proof-of-principle experiment demonstrates the basic soundness of the theory of mesoscopic energy harvesting with energy filtering techniques at the quantum level, realising a heat engine.

Then we investigate the thermometry study of such a quantum-dot energy-harvester device. This part of the thesis describes the characterisation and performance of a non-invasive single-electron thermometer, and extracts the electrical temperatures via three methods as below. First, we introduced the extracting of the electrical temperatures through fitting the differential-conductance peaks with theoretical models. The advantage of this method is that the quantum dot can directly serve as a thermometer. The disadvantage is that the excitation voltage, applied to trigger the currents through quantum dots, will unavoidably

heat the device. Then we introduce the use of the quantum point contact (qpc) to extract temperatures via monitoring the changes in electrostatic potential of a one-dimensional channel close to the quantum dot. It is easier to set up this measurement, and the signal through a qpc is usually several times greater than the current through a quantum dot, which means that the qpc thermometer is much more sensitive than the quantum-dot thermometer for a similar experimental set-up. The third method is to use the Mott relation as an insight into the thermometry of our energy-harvester device. It is supposed to have higher accuracy compared to previous thermometers, because of the same sets of circuits and data used as the thermopower measurements.

Then I have presented our attempt to experimentally demonstrate the theoretical proposal of building an energy harvester with two resonant-tunnelling quantum wells by Sothmann *et al.* [2]. This can scale up the quantum-dot energy harvester, increase its working temperature and the generated thermal power. The design and fabrication process have also been presented in detail. Measurements has proven that the split-gate and mid-gate combination can successfully give us access to each individual layer. This work can be improved by fabricating such an energy-harvester device with a double-quantum-well wafer with a narrow barrier width.

Both devices discussed in this thesis require a good thermal contact to two-dimensional electron gases. The electron temperatures are key to study their power and efficiency, and therefore it is important to study the thermometry of corresponding measurements.

Acknowledgements

Studying in Cambridge has been an inspiring and empowering experience to me. I have grown a lot both professionally and personally in past four years. I am very grateful to this opportunity given by Cambridge University and the Physics Department, as well as my financial supporters, the China Scholarship Council, the Great Britain-China Educational Trust, the Lundgren Fund, St.Edmund's College, as well as the SP group.

I could not have done this without the guidance and supports from my supervisor Prof. Charles Smith. During my PhD study, he has guided me, with great patience and kindness, to build a project, measure micro/nano devices, analyse data, write a scientific paper and so on. I did not start with a great set of experimental skills, and I have made so many mistakes while learning. Charles, however, has always been there and patiently waiting for my transform. It has been a privilege working with him, and I owed him a great deal for the physicist I am becoming. In past two years, I have also been challenged by some circumstance changes. I am embarrassed to admit I have burst into tears many times while facing them. Fortunately, I can always turn to Charles for some supports and advice. Meanwhile I want to thank my tutor, Dr. Anna Gannon, and my college (St.Edmund's College) for the supports they shown me during this period.

This PhD work is not possible without the help from my amazing collaborators, Dr. Rafael Sánchez, Prof. Andrew Jordan and Prof. Björn Sothmann. They have been very supportive and patient with me, and have taught me a lot about physics research. I am also grateful to help from the post-doc staff in SP. I thank Dr. Reuben Puddy for training me to use the clean-room equipment and the dilution refrigerator, as well as to his contributions to the quantum dot energy harvester device presented in this thesis. I also want to thank Dr. Joanna Waldie and Dr. Luke Smith for helping me sort the super leak issue found in the MX40. I am grateful to Joanna's help for the 10T maintenance as well as many kind suggestions she offered while I was struggling. I learnt a lot from Prof. Chris Ford, Dr. Ateeq Nasir, Dr. Harvey Beere and Dr. Yilmaz Gul during the small talks or meetings we had at the SP group.

I am glad I have met many interesting people in the physics department. I had a great time having coffee/tea or lunch with Shu-Wei, Ziwei, Fulden, Vivek, Jordan, Ankita, Hugo, Jinggao and many others. They always brought up novel stories and fun topics to discuss,

and truly brought much joy and laughter for my lab time. Special thanks to my dear friends Fulden and Shu-Wei, who have been great listeners and kind advisers at my difficult times. I also want to thank my friends outside of the laboratory, Qiaoling, Qihuan, Yuanyuan, and Gulmira, for the weekend tea or dinners with some fun and relaxing chats.

Last but not least, I want to thank my amazing parents for their unconditional love and supports. They are the most loving, the most caring and the kindest people I know, and the great role models I am blessed to have for life. There are no words that would be enough to express my love and gratitude, and I only hope this little poem could help me say how much I love them and have missed them.

I carry your heart with me

i carry your heart with me (i carry it in
my heart) i am never without it (anywhere
i go you go, my dear; and whatever is done
by only me is your doing, my darling)
i fear
no fate (for you are my fate, my sweet) i want
no world (for beautiful you are my world, my true)
and it's you are whatever a moon has always meant
and whatever a sun will always sing is you

here is the deepest secret nobody knows
(here is the root of the root and the bud of the bud
and the sky of the sky of a tree called life; which grows
higher than soul can hope or mind can hide)
and this is the wonder that's keeping the stars apart

i carry your heart (i carry it in my heart)

E. E. CUMMINGS

I would like to dedicate this thesis to my loving parents.

Table of contents

List of figures

List of tables

Chapter 1

Introduction

1.1 Motivation

Energy harvesting is the process by which energy is taken from the environment and transformed to provide power for electronics [3]. Specifically, thermoelectrics can play a crucial role in future developments of alternative sources of energy. In recent years there has been an increased interest in devices which can convert waste heat into useful work [3]. Thermoelectric generators where a temperature bias applied to an electric conductor gives rise to a charge current flow are good candidates [4, 5]. Unfortunately, current thermoelectric devices have relatively small efficiencies [6]. This issue can be overcome by nanoscale thermoelectrics where engineered bandstructures and quantum-mechanical effects can give rise to an increased efficiency [7–9]. Quantum dots constitute an important element in designing highly efficient thermoelectrics [10–13] because their discrete resonant levels provide excellent energy filters. Thermoelectric effects have been investigated in various quantum-dot setups [14–24].

Energy-harvesting devices require that the energy source is separated from the electrical circuit, so no charge is extracted from it [25]. This can be accomplished in three-terminal devices where a hot terminal injects heat but no charge into the setup, thus driving a charge current between two cold reservoirs. There have been a number of proposals for these kinds of energy harvesters [1, 2, 26–43]. Three-terminal heat engines based on Coulomb-coupled quantum dots [27, 28] have been realised experimentally recently [44–46]. Due to their design they are however limited to low power. A three-terminal energy harvester based on two resonant-tunnelling quantum dots with different energy levels overcomes this issue. It can in principle reach Carnot efficiency and can be optimised to achieve a large power in combination with a high efficiency at maximum power [1]. A similar device has also

been proposed [47, 48], and later demonstrated [49], as a building block of a nanoscale refrigerator.

In this manuscript, we experimentally realise a resonant-tunnelling energy harvester and demonstrate its ability to generate electrical power in an external load arising from energy exchanges between a hot and a cold reservoir. Importantly, no external drive or cycling is required; that is, the system is entirely autonomous and begins producing power as soon as a thermal gradient is present.

1.2 Thesis layout

This thesis will be continued through the following four chapters :

- **Chapter 2** introduces several topics that are of particular relevance to the work in this thesis. It includes explanations of a two-dimensional electron gas in GaAs/AlAs, quantum dots/wires/wells, electron-electron/electron-phonon interactions and the thermoelectricity of quantum dots.

- **Chapter 3** presents the experimental realisation of an efficient autonomous nanoscale energy harvester that utilises the physics of resonant-tunnelling quantum dots, following a proposal [1]. It details the design, fabrication and measurement of a quantum-dot energy-harvester device. Extensive characterisation of the device is presented to establish that it fulfills the known requirements for achieving such an device. At the end of the chapter, measurement results are presented including the thermal power characteristics.

- **Chapter 4** discusses the thermometry study of this quantum-dot energy harvester. It presents the measurement techniques as well as different theoretical approaches used to extract electron temperatures of nano devices at low temperatures.

- **Chapter 5** discusses the experimental attempt to scale up the quantum-dot energy harvester, presented in Chapter 3 and 4, with double quantum wells. It presents the theoretical proposal, device design, device fabrication and the measurements. It discusses the data analysis as well as the causes for the failure of the device operation.

- **Chapter 6** concludes what we discuss in previous chapters, with possible future work that can be done to improve the quantum-dot energy-harvester device.

1.3 Publications

The main results of the quantum-dot energy-harvester experiment have been published in:

- G. Jaliel, R.K. Puddy, R. Sánchez, A.N. Jordan, B. Sothmann, I. Farrer, J.P. Griffiths, D.A. Ritchie, C.G. Smith, *Experimental realization of a quantum dot energy harvester*, Phys. Rev. Lett. 123, 117701 – Published 9 September 2019.

Chapter 2

Background

2.1 The two-dimensional electron gas

One of the most widely studied low-dimensional electronic systems is the two-dimensional electron gas (2DEG) in semiconductors. This is a system in which electrons are confined to an interface between two materials, where in one direction (z) the confinement has a length scale comparable to the Fermi wavelength, and in the other two directions (x and y) the confinement has a large enough distance for the quantisation of momentum in the x-y plane to be neglected. Typically the 2DEG is formed at the interface between two semiconductors with different band gaps, or between a semiconductor and an insulator [50]. In both cases the conduction band edge has a discontinuity at the interface. A potential well is formed in the conduction band by bending the band structure with doping or an externally applied electric field. Once the bottom of the well is pulled below the Fermi energy, it becomes populated with electrons that form the 2DEG (see Fig. 2.1).

2.1.1 The 2DEG in a GaAs/AlGaAs heterostructure

A clean 2DEG can be formed in GaAs because the lattice constant of GaAs (5.653 Å) is very similar to that of AlAs (5.660 Å), but the band gap (the energy difference between the valence and conduction band) is different between the two. A whole range of band-gap values can then be produced by replacing a fraction, x, of Ga atoms in GaAs with Al atoms to produce $Al_xGa_{1-x}As$. This has a band gap that approximately follows $E_{gap} = (1.424 + 1.247x)eV$ at room temperature. Layers of AlGaAs and GaAs can therefore be grown on top of each other with very little lattice mismatch, minimising the strain and the density of misfit dislocations at the interface. The GaAs/AlGaAs system therefore provides an excellent way to produce

high-quality interfaces with a tunable band-structure [50]. This material can be produced by the development of molecular-beam epitaxy (MBE), a technique whereby individual atomic layers of $Al_xGa_{1-x}As$ with different doping and mole fractions (x) can be deposited on a GaAs wafer. This technique enabled band-gap engineering in the direction of growth and the resulting material is called a heterostructure, or 'High Electron Mobility Transistor' (HEMT) heterstructure.

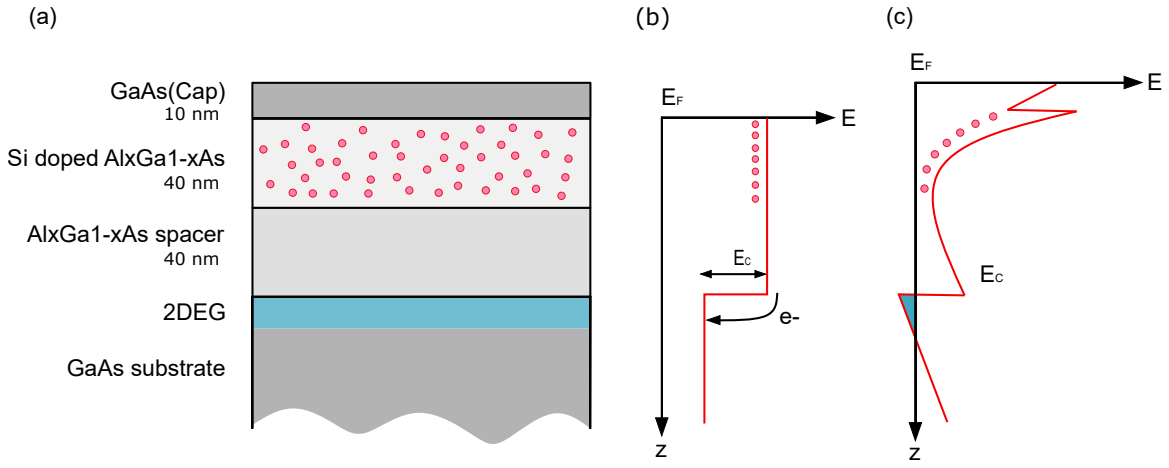

Fig. 2.1 Panel (a) shows a standard HEMT heterostructure, with layers of different materials. Typically the capping layer is 10 nm thick, used to protect the AlGaAs layer from oxidation. Both the spacer and dopant layers are 40 nm thick. The red dots depict the randomly positioned Si dopants. A typical value chosen for Al fraction in the AlGaAs is $x = 0.33$. The 2DEG is formed 90 nm below the surface, at the interface between AlGaAs and GaAs. The spacer layer of 40 nm is grown to keep the donor ions a certain distance from the 2DEG in order to reduce scattering and increase electron mobility. Panel (b) is the conduction band at the interface between $Al_xGa_{1-x}As$ and GaAs in a heterostructure before 2DEG formations. Electrons from the donors in $Al_xGa_{1-x}As$ migrate to GaAs and are trapped there. Panel (c) is the corresponding conduction-band edge of this $Al_xGa_{1-x}As$/GaAs after the formation of 2DEG. Electrons are trapped in a triangular potential well at the heterojunction at low temperatures.

Figure 2.1(a) illustrates a typical GaAs/AlGaAs heterostructure, where a 2DEG is created 90 nm below the surface of the wafer. For standard heterosturctures, a few microns of GaAs material is grown first, then followed by a spacer layer of 40 nm of undoped GaAlAs, to keep the donor ions a certain distance from the 2DEG in order to reduce scattering and increase electron mobility. The Si-doped GaAlAs donor layer of 40 nm is then grown to provide the electrons which form the 2DEG. A final GaAs capping layer of 10 nm is required to protect the AlGaAs layer from oxidation. A typical value chosen for the Al fraction in the AlGaAs is $x = 0.33$.

Figure 2.1(c) shows the corresponding conduction-band edge of this HEMT. The Fermi energy (E_F) of a semiconductor is the energy above which electron states are empty and below which they are filled (at low temperatures). AlGaAs has a different band gap compared to GaAs, as shown in Fig. 2.1(b). Free electrons move to the GaAs/AlGaAs interface from the the Si-doped AlGaAs layer, causing the boundary between the doped AlGaAs and GaAs to sink below the Fermi energy, forming a triangular well with free electrons in it. The positive charge left behind at the donor sites leads to band bending, in order for the system to achieve charge equilibrium again. This results in the conduction band being deformed as shown in Fig. 2.1(c). Since the electrons lose energy in equilibrium, they get trapped in the GaAs, due to the low temperatures and the height of the barrier E_C. A sheet of electrons (the 2DEG) parallel to the interface is then formed. The studies presented in later chapters are conducted at low temperatures ($\leq 4.2K$), where electrons occupy only the ground state (the lowest 2D subband), of the triangular potential well and are confined there.

The mobility of an electron gas is a measure of the drift velocity of the electrons in response to an applied electric field. Typically, mobilities in HEMT devices are $\sim 10^6$ $\mathrm{cm^2V^{-1}s^{-1}}$.

2.1.2 The contact and confinement of the 2DEG

The semiconductor 2DEG has been the foundation for many studies of mesoscopic 2D effects and lower-dimensional electron gases. This has been possible because of the fast development of semiconductor processing technology that gives access to the 2DEG and allows sub-micron scale patterning on the surface of devices.

As can be seen in Fig. 2.1, the 2DEG in a HEMT heterostructure resides a significant distance below the surface. To make an electrical contact to it, a conducting channel must be formed down through the material. This can be achieved by annealing certain material into the heterostructure that provide extra localised doping. A common choice is to pattern AuGeNi on the surface of the material, which on annealing diffuses downwards to form conducting paths that contact the 2DEG. These techniques are illustrated in Fig. 2.2(c).

There are two ways to create lateral confinement of a 2DEG. First, as shown in Fig. 2.2(a), gate electrodes can be patterned on the surface of a heterostructure, and by varying the voltage applied to them, the carrier density in the 2DEG beneath the gate is changed. If a sufficiently negative voltage is applied, the conduction band can be pushed back above the Fermi energy, and then the electron gas beneath the gate can be completely depleted. Thus, the depopulation of electrons can act as the confinement. Second, as shown in Fig. 2.2(b), lateral confinement can also be achieved by etching the heterostructure in certain places, leaving the 2DEG intact in only the un-etched regions. More specific details about how to fabricate electrode gates

and ohmic contacts on the GaAs/AlGaAs 2DEG systems will be discussed in the fabrication section in following chapters.

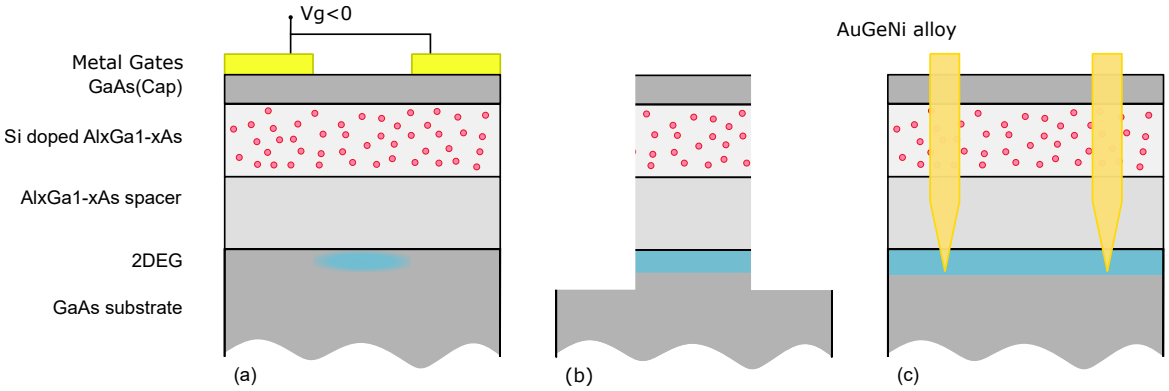

Fig. 2.2 Panel (a) shows the lateral confinement in a 2DEG using surface gates. The 2DEG is depleted below the gates when a sufficiently negative voltage is applied to them. Panel (b) shows the lateral confinement by etching. The 2DEG is removed from below the etched pits when they are deep enough to have a significant effect on the band structure. Etching away the doped layer from the heterostructure will ensure that this happens. Panel(c) shows an ohmic contact going from the HEMT surface to the 2DEG.

2.1.3 Dimensionality and Density of states

Quantum effects arise in systems which confine electrons to regions comparable to their de Broglie wavelength. When such confinement occurs in one dimension only, with free motion in the x- and y- directions, a 2DEG is created with techniques discussed above. Confinement in two directions (y and z, say), with free motion in the x-direction, gives a one-dimensional gas (1DEG) and confinement of its x-, y-, and z-motions at one gives a zero-dimensional system. The density of states and carrier concentrations also vary with dimensionality of electron gases.

An unconfined electron in free space is described by the Schrödinger equation

$$-\frac{\hbar^2}{2m}\Delta\phi = -\frac{\hbar^2}{2m}\left(\frac{\partial^2\phi}{\partial x^2}+\frac{\partial^2\phi}{\partial y^2}+\frac{\partial^2\phi}{\partial z^2}\right) = E\phi \tag{2.1}$$

where m is the free-electron mass. The solution of this equation, $\phi_{\mathbf{k}}(\mathbf{r}) = e^{i\mathbf{k}\cdot\mathbf{r}}$, are plane waves labelled by the wavevector, $\mathbf{k} = (k_x, k_y, k_z)$, and correspond to the energy:

$$E_{3D} = \frac{\hbar^2 k^2}{2m} = \frac{\hbar^2}{2m}(k_x^2 + k_y^2 + k_z^2). \tag{2.2}$$

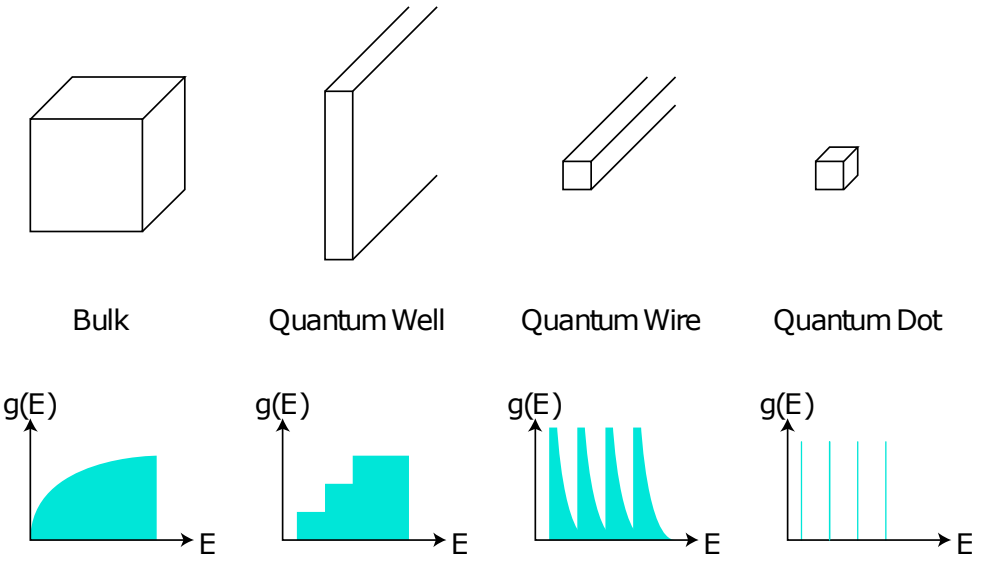

Fig. 2.3 Variation of the energy density of states as the number of confined directions increases. The continuum of states in the bulk material is replaced by quantised energy bands in the quantum-well structure and finally by atomic-like energy levels for the quantum dots. This figure is adapted from Ref [51].

The vector component of **k** are the quantum numbers for the free motion of the electron, one for each of the classical degrees of freedom. The number of states in a volume $d\mathbf{k} = dk_x dk_y dk_z$ of **k**-space is

$$g_{3D}(\mathbf{k})d\mathbf{k} = \frac{2}{(2\pi)^3}d\mathbf{k} \tag{2.3}$$

with the factor of 2 accounting for the spin-degeneracy of the electrons. To express this density of states in terms of energy states, we use the fact that the energy dispersion depends only on the magnitude of **k**. Thus, by using spherical polar coordinates in **k**-space, $d\mathbf{k} = k^2 sin\theta dk d\theta d\phi$, where the variables have their usual ranges ($0 < k < \infty$, $0 < \phi < 2\pi$, and $0 < \theta < \pi$) and, integrating over the polar and azimuthal angles, we are left with an expression that depends only on the magnitude k: $g(\mathbf{k})d\mathbf{k} = 2/(2\pi)^3 d\mathbf{k} = 1/(\pi^2)k^2 dk$. By invoking Equation (2.2), we can perform a change of variables to cast the right-hand side of this equation into a form involving the differential of the energy, and deduce the well-known density of states $g(E)$ of a free electron gas in three dimensions:

$$g_{3D}(E) = \frac{1}{2\pi^2}(\frac{2m}{\hbar^2})^{3/2}\sqrt{E}. \tag{2.4}$$

The carrier concentration, n, is given by

$$n_{3D} \equiv \frac{N}{V} = \frac{\int_0^{k_F} g(k)dk}{1} = \frac{k_F^3}{3\pi^2}. \tag{2.5}$$

An ideal 2DEG differs from free electrons in three dimensions in that the electrons have unrestricted movement in only two dimensions (x and y) with complete confinement in the z-direction, i.e. there is no degree of freedom at all in this direction. Ignoring the energy of z-confinement, the energy of an electron in a 2DEG is therefore

$$E_{2D} = \frac{\hbar^2 k^2}{2m^*} = \frac{\hbar^2}{2m^*}(k_x^2 + k_y^2). \tag{2.6}$$

Here m^* is the effective mass of the electrons, defined by $m^* = \hbar^2/(dE^2/dk^2)$, where the periodic potential due to the atoms is taken into account. In GaAs the effective mass is $0.067\, m_e$ [50]. The number of states within an area in k-space of $d\mathbf{k} = dk_x dk_y$ is $g(k) = 2/(2\pi)^2$, with the factor of 2 again inserted to account for the spin degeneracy of the electrons. Similarly above through *circular polar coordinates* and the relationship between E and k in Equation (2.6), the density of states in terms of the energy can be written as:

$$g_{2D}(E) = \frac{m^*}{\pi\hbar^2}. \tag{2.7}$$

Thus, for a 2DEG the density of states is a constant, i.e. independent of the energy. The carrier concentration, n, is given by

$$n_{2D} = \frac{k_F^2}{4\pi}. \tag{2.8}$$

When an electron is allowed only one-dimensional motions (along, say, the x-direction), the energy is given by

$$E_{1D} = \frac{\hbar^2 k^2}{2m^*} = \frac{\hbar^2 k_x^2}{2m^*}. \tag{2.9}$$

Similarly, the density of states can be expressed as:

$$g_{1D}(E) = \frac{1}{\pi}\left(\frac{2m^*}{\hbar^2}\right)^{1/2} \frac{1}{\sqrt{E}}. \tag{2.10}$$

This shows that the density of states of a one-dimensional electron gas has a square-root singularity at the origin. The carrier concentration, n, is given by

$$n_{1D} = \frac{k_F}{2\pi}. \tag{2.11}$$

An ideal zero-dimensional electron is one that exists in a single state of fixed energy E_0. The density of states is then given by

$$g_{0D}(E) = \delta(E - E_0) \tag{2.12}$$

where $\delta(x)$ is the Dirac delta-function. The dimensionality and the state density is depicted in Fig.2.3.

The reduction in dimensions to two, one and zero dimensions has introduced a wide range of new physics. Restricting electron transport in one direction, known as a 2DEG or a quantum well, has led to the discovery of the quantum-Hall effect [52] and the fractional quantum-Hall effect [53]. Restricting electron transport in two directions, known as quantum wires, has led to the discovery of the quantisation of conductance in units of $2e^2/h$, independently demonstrated by van Wees [54] and Wharam [55]. Further stronger confinement of the 2DEG in all directions can form a zero-dimensional system, known as quantum dots. These systems are a pool of trapped electrons, isolated and manipulated by electrode gates on the surface [56–58], or etched pillar structures [59]. They have attracted attention both for their versatility for studying fundamental physics, as well as being promising candidates for implementing several solid-state quantum-computation architectures [60–64].

2.2 Quantum dots

This section outlines the effects that dominate the behaviour of quantum dots, as observed in transport measurements. The discussions mainly focus on the regime of weak coupling between a dot and any nearby conductors, as it is most relevant to this thesis.

2.2.1 The Coulomb-blockade regime

As discussed in the previous section, a quantum dot is an isolated island of charge. Because of the small radius of quantum dots, the capacitance is very small, so that it requires a significant energy e^2/C to add an extra electron to the dot. Until this energy is somehow supplied, no charge may move onto or off the island and it is said to be *'Coulomb blockaded'*.

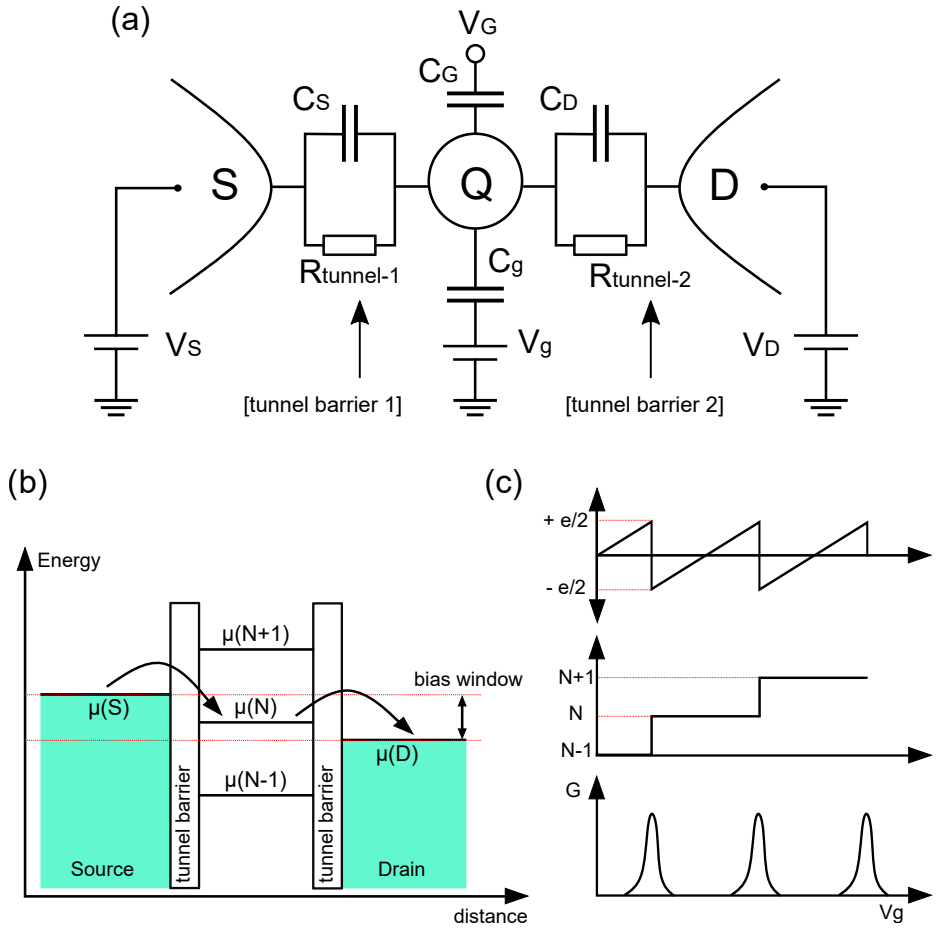

Fig. 2.4 (a) Equivalent circuit for a typical quantum dot. The dot has a charge Q, and it is connected by two tunnel barriers to Source and Drain reservoirs, which are at voltages of V_S and V_D respectively. The electrochemical potential of the dot can be controlled by the voltage of a capacitively coupled gate electrode (V_g). The charging energy is determined by the total capacitance: $C_\Sigma = C_S + C_D + C_g + C_G$. (b) Schematic diagram of the energies of a quantum dot system as a function of distance. Located between the tunnel barriers is the quantum dot, represented as a ladder of states. All the states below the source and drain chemical potentials are filled. Each state, separated by the single-particle energy E_{0D}, can hold an up and a down spin electron. The difference between source and drain voltages creates the so-called bias window: if a state falls within this window current can flow. (c) shows the charge (top), number of electrons (middle), and conductance (bottom) through a dot versus gate voltage.

Two conditions must be satisfied for Coulomb blockade to be observable. Firstly, the charging energy must be greater than any thermal fluctuations: $e^2/C \gg k_B T$, where k_B is Boltzmann's constant. Therefore, we must have a low enough temperature, and for a typical experimental temperature of 100 mk, this implies that the total island capacitance must be much less than 19 fF; Secondly, the barriers that constitute the electrostatic confinement

potential are sufficiently opaque. The Heisenberg uncertainty principle can be applied to the dot by using its charging energy $\Delta E = e^2/C$, and the time it takes to charge or discharge, $\Delta t = R_t C$ (here R_t is the resistance of the tunnelling barriers). The relation between the two therefore is: $\Delta E \Delta t > \hbar/2$ which yields a lower bound on the tunnelling resistance: $R_t \gg \hbar/2e^2$ ($R_t \gg 12k\Omega$) in order for the electronic states to be confined in the dot. The typical configuration of a quantum dot is depicted by an equivalent circuit diagram in Fig. 2.4(a). The total capacitance of the island (C_Σ) is small enough, and the tunnel-barrier resistances (R_t) large enough, that the dot will exhibit Coulomb blockade at its operating temperature. The dot is tunnel coupled to conducting source and drain reservoirs. The inclusion of a capacitively coupled gate electrode allows the potential of the dot to be controlled.

We use the *constant-interaction model* [62] to describe the quantum system shown in Fig. 2.4(a). It assumes firstly that interactions between electrons on the dot with one another and with the surrounding electrons can be described by a single, constant capacitance: $C_\Sigma = C_S + C_D + C_g$, where C_S, C_D and C_g are the parallel capacitances, shown in Fig. 2.4(a), of the source, drain and gate electrodes respectively. The tunnel barriers are represented by the resistors, $R_{tunnel-1}$ and $R_{tunnel-2}$ in Fig. 2.4(a). Stray capacitances C_G from the environment can be added in the same way but are ignored here. Secondly it assumes that the discrete energy levels of the dot are independent of the number of electrons [62, 64]. From these assumptions and using the equation for the electrostatic energy stored in a capacitor, $U = Q^2/2C$ and $Q = CV$ we have the electrostatic energy of the dot containing N electrons as:

$$U(N) = \frac{(-e(N-N_0) + C_S V_S + C_D V_D + C_g V_g)^2}{2C_\Sigma} + \sum_{n=1}^{N} E_n, \tag{2.13}$$

where e is the electron charge, N_0 is the charge on the quantum dot due to the positive background charge of the donors [65], E_n is the n^{th} occupied energy level of the dot and $V_{S,D,g}$ are the voltages on the source, drain and gate electrodes respectively. The change in energy as the dot goes from the $(N-1)$-electron ground state to the N-electron ground state is defined as the electrochemical potential:

$$\mu(N) \equiv U(N) - U(N-1) = (N - N_0 - \frac{1}{2})\frac{e^2}{C_\Sigma} - (C_S V_S + C_D V_D + C_g V_g)\frac{e}{C_\Sigma} + E_N. \tag{2.14}$$

The *addition energy* or *charging energy* of the dot, defined as the energy required to add one electron to the dot, is therefore given by:

$$\mu(N+1) - \mu(N) = \frac{e^2}{C} + \Delta E_N. \tag{2.15}$$

The term of ΔE_N is the spacing between the N_{th} and the $(N-1)_{th}$ single-particle states for the specific confinement potential of the dot. The value of ΔE_N can be found experimentally by observing variations in the addition energy $(\mu_{N+1}-\mu_N)$ [66]. From Equation 2.14 we can see that the electrochemical potential of the dot is linearly proportional to the voltage $V_{S,D,g}$, with a coefficient of $\frac{C_i}{C_\Sigma}$. This is called *lever arm*, and will be discussed in details in section 2.2.3.

Figure 2.4(b) depicts a schematic diagram of the energy across of a quantum-dot system. The energy levels are shown as a ladder of states between the two tunnel barriers. Each state can hold two electrons with opposite spin. The chemical potential of the leads is $\mu_{S,D} = eV_{S,D}$, and a bias windows is defined as $\mu_S - \mu_D$. Every time when a dot state lies within this window, a current, proportional to the tunnelling rates on and off the dot, will flow. This will result in a resonant peak in the conductance. When no state lies within the bias window no current can flow and the dot is in the Coulomb-blockade regime. The periodic peaks in the conductance of a quantum dot are commonly referred as *Coulomb-blockade peaks*. They are separated by a gate voltage that corresponds to a change in μ_N of the charging energy plus the energy spacing of the lowest available single-particle state. Because the charge is now quantised, the lowest energy state of the dot can only take integer values. Therefore, as the gate voltage is swept, the dot charge, taking into account the background donors, will oscillate from being charged $+e/2$ to $-e/2$ [50].

2.2.2 Coulomb-blockade peaks

The transport of electrons through a quantum dot can be largely understood by considering sequential tunnelling across the two tunnel barriers, where the duration of tunnelling events is far shorter than the time between them. A theory of linear transport ($V_{SD} = V_S - V_D = 0$) in this situation was given by Beennaker [67], and for non-linear transport ($V_{SD} \neq 0$) by Averin, Korotkov and Likharev [68]. In this section, we discuss the current through the quantum-dot system shown in Fig. 2.4(b) and the Coulomb peaks in this quantum Coulomb-blockade regime, $k_B T \ll \Delta E < e^2/C$, where only one or a few levels participate in transport.

The method is first to calculate the current due to electrons impinging on the barrier from the source and then to add that due to electrons arriving from the drain. The expressions for these are similar except for the Fermi levels. The current due to electrons from the source at the left is given by:

$$I_S = 2e \int_0^\infty f[\varepsilon(k), \mu_S] v(k) T(k) \frac{dk}{2\pi}. \tag{2.16}$$

This integration are carried out in the left lead, and the significance of each term can be understood as follows: i) the factor of e converts number current into electrical current (the

sign of the electronic charge $-e$ vanishes because conventional current flows from right to left in response to a positive bias on the right); ii) the integral is restricted to positive values of k because we include only electrons that impinge on the barrier from the left. the quotient $dk/2\pi$ is the usual one for counting k-states (section 2.1.3), and the factor of 2 in front accounts for the two spins; iii) $f[\varepsilon(k), \mu_S]$ is the Fermi-Dirac occupation function of the left lead: $(f(E,\mu) = 1/(1+e^{(E-\mu)/k_BT}))$. It gives the probability that each state is occupied, governed by the Fermi level μ_S of the source; iv) the factor of velocity $v(k)$ turns the charge density into a current density as in the usual expression $J = nqv$; v) finally, the (flux) transmission coefficient $T(k)$ gives the probability that an incident electron passes through the barrier (the quantum dot) and contributes to the current. If it is reflected it leaves the system to the left (source) and makes no contributions to the current [69].

It is usually more convenient to perform the integration over energy rather than wave number. This can be done by changing the variable of integration and using: $dk = \frac{dk}{dE}dE = \frac{1}{\hbar v}dE$. Inse'rting this into Equation 2.16, and denoting the bottom of the band in each lead by U_S and U_D, gives:

$$I_L = 2e\int_{U_S}^{\infty} f(E,\mu_S)vT(E)\frac{dE}{2\pi\hbar v} = \frac{2e}{h}\int_{U_S}^{\infty} f(E,\mu_S)T(E)dE. \tag{2.17}$$

The velocity cancels in this expression, and important feature that underlies the quantised conductance (section 2.3.1). The expression for the current due to electrons arriving from the right (drain) is almost identical. The only differences are the sign, as the electrons are travelling in the opposite direction, the Fermi level, and the lower limit of the integral over energy. Thus:

$$I_R = -\frac{2e}{h}\int_{U_D}^{\infty} f(E,\mu_D)T(E)dE. \tag{2.18}$$

The transmission coefficient is the same from both sides of a barrier, so the same function $T(E)$ appears in I_L and I_R. It is clear that electrons in the range from U_S to U_D cannot contribute to the current because there are no propagating states with these energies on the left. Thus the lower limit on both integrals can be taken as the higher of the two U in general (here it is U_D). Adding the two expressions gives the net current:

$$I = \frac{2e}{h}\int_{U_S}^{\infty} [f(E,\mu_D) - f(E,\mu_S)]T(E)dE. \tag{2.19}$$

If the bias is very small the difference in Fermi functions can be expanded to lowest order in a Taylor series [69]. Put $\mu_S = \mu + \frac{1}{2}eV$ and $\mu_D = \mu + \frac{1}{2}eV$ where μ is the Fermi level at equilibrium. Then:$f(E,\mu_D) - f(E,\mu_S) \approx eV\frac{\partial f(E,\mu)}{\partial \mu} = eV\frac{\partial f(E,\mu)}{\partial E}$. The last form follows

because $f(E,\mu)$ is a function only of the difference $E-\mu$. Then [69]:

$$I = \frac{2e^2V}{h}\int_{U_S}^{\infty}(-\frac{\partial f}{\partial E})T(E)dE. \tag{2.20}$$

The current is directly proportional to the applied voltage in this limit, so Ohm's law holds. The conductance $G = I/V$ is given by:

$$G = \frac{2e^2}{h}\int_{U_S}^{\infty}(-\frac{\partial f}{\partial E})T(E)dE. \tag{2.21}$$

The integral integral itself is dimensionless and the prefactor provides the dimensions of conductance. The quotient e^2/h is often described as the quantum unit of conductance, with magnitude $38.7\mu S$. The corresponding resistance $R_K = h/e^2 = 25.8k\Omega$. The factor of $-\partial f/\partial E$ emphasises that conduction takes place near the Fermi level in a degenerate system, as the derivative is peaked about the Fermi level with a width of a few times k_BT [69]. G, proportional to $\partial f/\partial E$, is theoretically expected when the conductance between two Fermion baths is limited by tunnelling through a narrow transmission resonance if the natural width of the resonance is $\ll k_BT$ [58].

Now we discuss how to calculate the transmission probability $T(E)$ in Equation 2.21, more specifically, the transmission probability of an incoming electron to transverse the two barriers defining the quantum dot. Since the barriers are not infinitely thick, an electron trapped in the well can leak out, giving a resonant or quasi-bound state rather than a true bound state. If the two barriers individually have transmission coefficient of T_L and T_R respectively, in general, the transmission probability T of two barriers is roughly the product of T_L and T_R. Near the resonance, however, T rises dramatically above the product, T_LT_R, and reaches its maximum value of unity if the structure is symmetric: there is a perfect transmission through the double barrier, however opaque the individual barriers [69]. This is called *resonant tunnelling*. The transmission coefficient a function of energy E with a full-width at half-maximum (FWHM) Γ can be written as:

$$T(E) \approx \frac{4T_LT_R}{(T_L+T_R)^2}[1+(\frac{E-\mu_{dot}}{\Gamma/2})^2]^{-1}, \tag{2.22}$$

where the resonance is centred on chemical potential of the dot, μ, with a height of $\frac{4T_LT_R}{(T_L+T_R)^2}$. This Lorentzian shape with FWHM of Γ is typical of resonant phenomena. It can be derived from elementary considerations. The velocity of an electron in the resonance is v and the distance of a round trip is $2a$, so it bumps against the left barrier $v/2a$ times per second. The probability of escaping is T_L on each occasion, so the average escape rate through the left

barrier is $vT_L/2a$. Including the right barrier gives the total rate, which can be converted into an uncertainty in the energy by multiplying by $\hbar$. The result is $\hbar v(T_L+T_R)/2a = \Gamma$, as found in the analysis. Alternatively, the lifetime of the quasi-bound state is $\tau = \hbar/\Gamma$ [69].

The transmission coefficient $T(E)$ also brings the Lorentzian shape with FWHM into the current (Equ. 2.20) and therefore the conductance (Equ. 2.21) of the quantum dot, which is found to be a good temperature detector to the leads [70]. This will be discussed later as a main topic to Chapter 4.

2.2.3 Coulomb diamonds

For biases larger than the blockade peak widths, the dot can no longer be characterised by a linear conductance. This is the non-linear transport regime. With the increase of the source-drain bias across the dot, more charge states will be available in the quantum dot for electrons to be transported through. This is called the *Coulomb Staircase*. With a large enough bias, the widened peaks from adjacent charge states overlap, leaving diamond-shaped regions of zero current between them. These are commonly referred to as *Coulomb diamonds*.

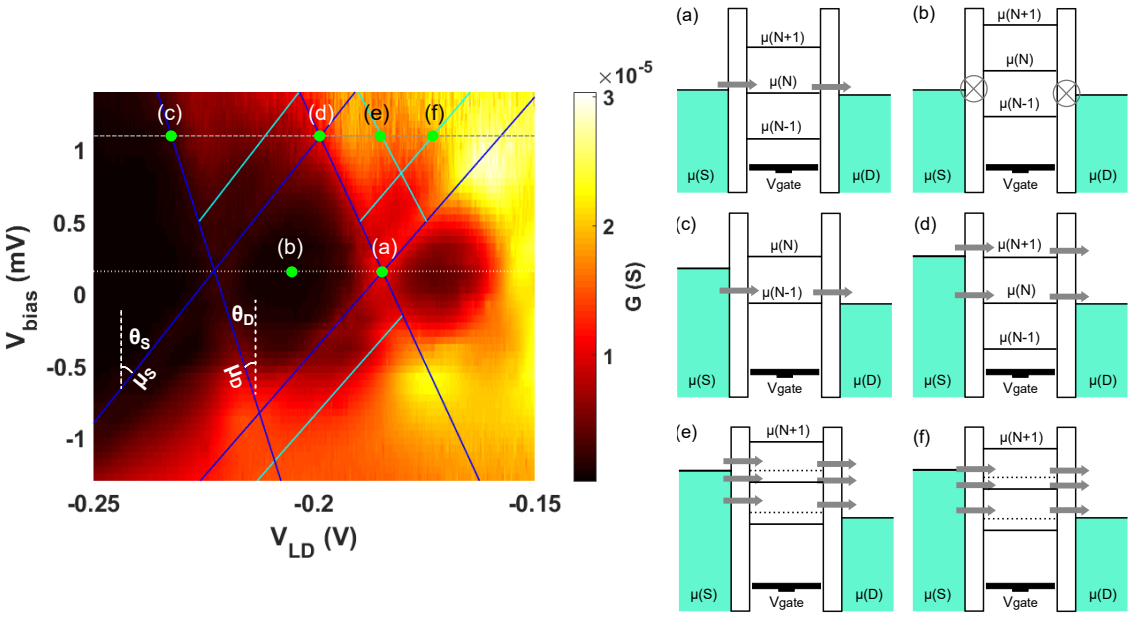

Fig. 2.5 Features of non-linear transport. On the left is a plot of the differential conductance (dI/dV) through a quantum dot with a biased drain. The blue lines label the Coulomb diamond where the tunnelling is blocked inside. Cyan lines label the excited states. The angles θ_S and θ_D are used to determine the conversion factor between V_G and dot energy. Inset (a)-(f) show the energy levels of the dot at the corresponding points on the axes.

Figure 2.5 shows the diamond-like shape at the left plot inside which transport through the dot is suppressed because of Coulomb blockade. At a $V_{SD} = 0$, the dot is in a charge-degenerate state (with the number of electrons changing from N to $N-1$). Panel (a) of Fig. 2.5 shows the linear transport while the bias voltage is zero. Panel (b) shows the Coulomb blockade while charge state lies within the bias window and no electron transport can occur. As the bias is increased, the transport window is widened until μ_N is also aligned inside it, as shown in Panel (d). This enables additional transport through the dot, and the dot charge state starts to fluctuate by not one, but two electrons. In reality, since $\Delta E < e^2/C$, the excited states, featured as cyan lines in the left plot, start contributing to transport before the transport window is wide enough to include the next charge state. Panel (e) shows where the excited state of $\mu(N)$ aligns with the electrochemical potential of the source, and panel (f) shows where the excited state of $\mu(N+1)$ aligns with the potential of the drain, while increasing the plunger-gate voltage to less negative. The energy spacing between the states is given by the distance between them in the direction of changing bias voltage, V_{SD}.

The boundaries of the Coulomb diamonds are labelled as 'μ_S' and 'μ_D' in Fig. 2.5. This is because they correspond to the energy level within the bias window being aligned with the source and the drain potentials respectively. The gradient of these resonances can be used to calibrate the conversion factor *lever arm*, between the change of gate voltage ΔV_g and the change in dot energy. From Equation 2.14, we can see that the electrochemical of the dot is linearly proportional to the voltages, $V_{S,D,g}$. For the quantum dot in Fig. 2.5, where the source is grounded ($V_S = 0, \mu_S = 0$), and a source-drain bias of V_{SD} is applied to the drain ($V_D = V_{SD}$, $\mu_D = -eV_{SD}$), Equation 2.14 can be written as:

$$\begin{aligned} \mu(N) &= -e\frac{C_D}{C_\Sigma}V_D - e\frac{C_g}{C_\Sigma}V_g + constant \\ &= -e\alpha_D V_D - e\alpha_g V_g \\ &\text{where } C_\Sigma = C_S + C_D + C_g, \alpha_S = C_S/C_\Sigma, \alpha_D = C_D/C_\Sigma, \end{aligned} \tag{2.23}$$

The drain resonance on a Coulomb-diamond plot is the line along which the electrochemical potential of the dot is aligned with that of the drain lead ($\mu(N) = \mu_D = -eV_{SD}$). Substituting this condition in Equation 2.23, differentiating with respect to the bias, and solving for the slope of the drain resonance we get:

$$m_D = \tan(\theta_D) = \left.\frac{dV_g}{dV_{SD}}\right|_D = \frac{1-\alpha_D}{\alpha_g}. \tag{2.24}$$

Similarly, the source resonance is the line along which the potential of the dot is aligned with that of the source ($\mu(N) = \mu_S = 0$). Differentiating Equation 2.23, and solving for the slope

of the source resonance we get:

$$m_S = \tan(\theta_S) = \left.\frac{dV_g}{dV_{SD}}\right|_S = -\frac{\alpha_D}{\alpha_g}. \tag{2.25}$$

We now solve Equation 2.24 and 2.25 to obtain the lever arm of the plunger gate and the source lead, respectively:

$$\alpha_g = \frac{1}{m_D - m_S}, \tag{2.26}$$

$$\alpha_D = \frac{1}{1-(m_D/m_S)}. \tag{2.27}$$

With the bias applied to only the drain reservoir, α_S cannot be found.

The lever arm of a gate or a lead quantifies the effect of the gate on the potential of the dot. It is a useful parameter to convert the experimentally measured voltage to energy.

2.2.4 Co-tunnelling and Kondo effect

So far we have discussed dots that are weakly coupled to their reservoirs and tunnelling events that occur one at a time. However, if the coupling is increased, higher-order processes involving two or more correlated tunnelling events can become important. Two examples are co-tunnelling and the Kondo effect. Both allow an electron to tunnel through a dot in an energetically unfavourable situation via an intermediate virtual state.

Co-tunnelling can give rise to the conductance inside the normally blockaded region of a Coulomb diamond [71–73]. Transport occurs when the dot temporarily occupies the energetically forbidden N-electron state. This is allowed by Heisenberg's uncertainty principle if a correlated tunnelling event quickly returns it to the original state. The net result

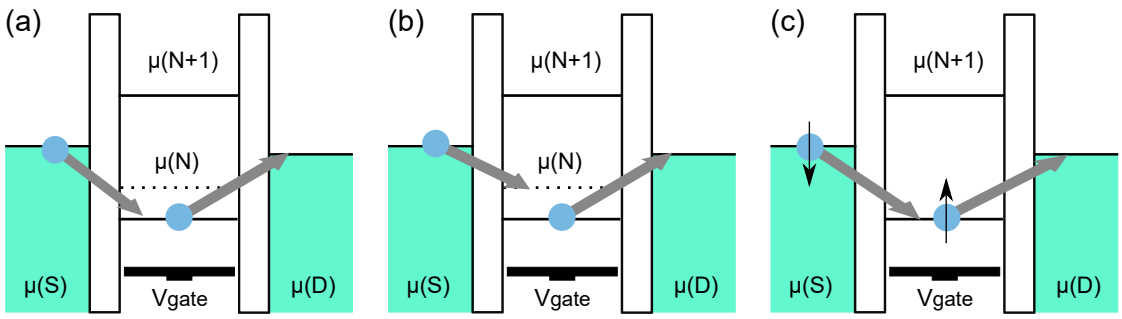

Fig. 2.6 Features of non-linear transport. (a) Elastic co-tunnelling; (b) Inelastic co-tunnelling; (c) Kondo effect.

is the transfer of an electron between the source and drain. Co-tunnelling can be either elastic or inelastic. In elastic co-tunnelling an electron leaves the dot at the same energy at which it enters, and the dot is left in its ground state, depicted in Fig. 2.6(a). In inelastic co-tunnelling an electron leaves with a lower energy, and the dot is left in an excited state, depicted in Fig. 2.6(b). Inelastic co-tunnelling may occur when an excited state lies within the bias window, and eventually connect to the first-order transport via an excited state at the edge of Coulomb diamonds. Co-tunnelling neglects contributions from spin that give rise to the Kondo effect in quantum dots.

The Kondo effect is a virtual tunnelling process that effectively flips the spin on the dot. One such example is depicted in Fig. 2.6(c). Successive spin-flip processes effectively screen the local spin on the dot such that the electrons in the leads and on the dot together form a spin-singlet state [74]. This macroscopically correlated state gives rise to the Kondo effect, which is well known from low-temperature resistivity measurements on metals containing a small fraction of magnetic impurities [75]. The Kondo effect was first observed experimentally in quantum dots in 1998 [74, 76, 77]. The typical signature of the Kondo effect in transport through a dot is finite conductance between blockade peaks that is suppressed by the application of a small bias. Kondo-mediated transport can only occur via a singly occupied, spin-degenerate energy level, and so only between alternate pairs of blockade peaks. The strength of the process is characterised by the *Kondo temperature*, above which it is suppressed. The Kondo effect in quantum dots has attracted continued interest as a controllable system in which many-body physics can be studied.

2.3 Quantum wires

This section gives an introduction to transport in a one-dimensional electron gas, known as *quantum wires*. Following the discussion of the 1D density of states in Section 2.1.3, a brief derivation of the conductance through an idealised 1D conductor is presented, within a non-interacting, single-particle picture. Electron transport is considered in the ballistic regime, where the length and width of the channel are much smaller than the electron mean free path, and conductance can be expressed in terms of the Landauer-Büttiker formalism.

2.3.1 The quantised conductance

Figure 2.7 shows a schematic representation of a 1D conductor, connected via 1D leads to two electron reservoirs. The chemical potentials in the 1D leads are μ_s and μ_d, and the arrows indicate the direction of current flow. In the following analysis it is assumed that there

is perfect transmission through the 1D conductor, and that current in each 1D subband does not scatter into another. Following the discussion on electron transport through a quantum dot in Section 2.2, the current flowing between the source and drain reservoirs is given by Equation 2.16, namely,

$$I = \frac{2e}{h}\int_0^\infty [f(E,\mu_D) - f(E,\mu_S)]T(E)dE.$$

The idealised 1D conductor has a perfect transmission ($T(E) = 1$), and at low temperature, where the electrons are highly degenerate, the Fermi occupation functions can be approximated by step functions [69]. Only electrons with energies between μ_S and μ_D contribute to the current. Thus, it simplifies to

$$I \approx \frac{2e}{h}(\mu_s - \mu_d) = \frac{2e^2}{h}V \tag{2.28}$$

where V is the potential applied between the source and drain reservoirs. The current through N subbands is simply the sum of the currents from each individual subband, i.e.

$$I = N\frac{2e^2}{h}V. \tag{2.29}$$

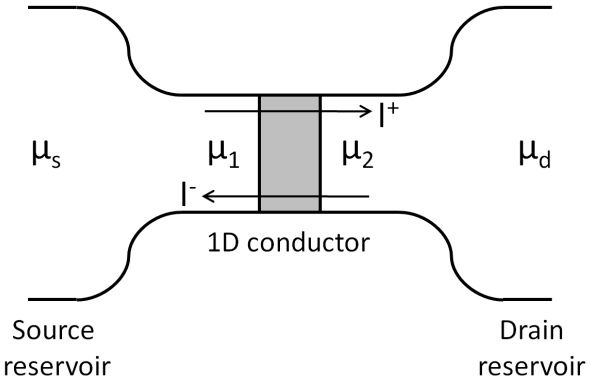

Fig. 2.7 Schematic diagram of a 1D conductor. The chemical potentials in the source and drain reservoirs are given by μ_s and μ_d, respectively. The chemical potentials in the 1D leads on either side of the 1D conductor are μ_1 and μ_2. The arrows represent the direction of current flow; right and left-going currents are labelled as I^+ and I^-, respectively. This figure is adapted from Ref [78].

The differential conductance is then given by

$$G = \frac{dI}{dV} = N\frac{2e^2}{h}. \tag{2.30}$$

This is the remarkable result that for a 1D conductor, conductance is quantised in units of $2e^2/h$. This arises from the cancellation of the energy-dependent terms in the density of states and group velocity, as discussed in section 2.2.2. In experimentally-realised 1D wires, the transitions between quantised steps are not perfectly sharp but are broadened by temperature and disorder.

The above discussion was based on a perfect 1D conductor, where there was no potential barrier between the source and drain reservoirs. However, in a real device the electrostatic confining potential in the 2DEG - generated by a split gate - is a smoothly varying function of position. The *Laudauer-Büttiker formalism* can be used to describe such a case.

Landauer presented a treatment of conductance in terms of transmission and reflection coefficients. Following Landauer, the conductance of a two-terminal 1D system which consists of a barrier and ideal 1D leads (having a flat potential) as given by Büttiker [79] is

$$G = \frac{e^2}{\pi\hbar}\frac{T}{R}, \tag{2.31}$$

where T and R are the transmission and reflection coefficients, respectively. This is the conductance through the barrier itself, where the chemical potentials used as those of the leads (μ_s and μ_d in Fig. 2.7). In the case of perfect transmission ($T = 1$, $R = 0$), the conductance tends to infinity. However, if the chemical potentials μ_s and μ_d in the electron reservoirs are used, one obtains [80],

$$G = \frac{e^2}{\pi\hbar}\,T. \tag{2.32}$$

Therefore, even in the case of perfect transmission, the conductance remains finite. This finite conductance was identified by Imry as the sum of two contact resistances (each equal to $h/4e^2$), which exist between each of the 1D leads and the reservoirs to which they are connected.

2.3.2 The 0.7 structure

In the above discussion, the quantisation of conductance in a quasi-1D channel was explained using the non-interacting, single-electron picture. However, electron interactions become increasingly important at low densities, and give rise to deviations from the non-interacting

picture, such as the shoulder-like feature near $0.7(2e^2/h)$ of the first conductance [81], called *0.7 structure*, as shown in Fig. 2.8. The 0.7 structure was first systematically studied by Thomas et al. in 1996 [81, 82], and since then a vast amount of experimental and theoretical literature has been published on the subject [83].

The 0.7 structure has a distinct magnetic-field and temperature dependence. As the magnetic field increases, the 0.7 structure continuously evolves into the e^2/h spin-split plateau, shown in Fig. 2.8(a). 0.7 structure at $B = 0\ T$ is marked by an arrow, and traces are offset horizontally for clarity. This behaviour was the primary reason for suggesting that the 0.7 structure is due to the spontaneous spin polarisation of the 1D electron gas at $B = 0\ T$. This suggestion conflicts with the Lieb-Mattis theorem, which states that an infinitely long 1D system of electrons cannot have a ferromagnetic ground state [84]. However, experimentally-realised 1D systems are not infinitely long, and are quasi-1D rather than strictly 1D therefore the Lieb-Mattis theorem does not necessarily apply. The temperature dependence of the 0.7 structure is shown in Fig. 2.8 (b). The 0.7 structure strengthens and becomes more pronounced as the temperature increases, while higher plateaux smear out due to the thermal broadening of the Fermi energy. This shows that the 0.7 structure can be induced by increasing temperature.

In addition to raising the temperature to produce a strong 0.7 structure, lowering the 2D density (n_{2D}) also causes a 0.7 structure to develop [82]. It therefore appears that the temperature scale of the 0.7 structure is related to the carrier density. At very low densities, it has been shown that the 0.7 structure tends to $0.5(2e^2/h)$ [85, 86]. Intriguingly, an enhancement of the 0.7 structure on increasing density has also been reported [87, 88],

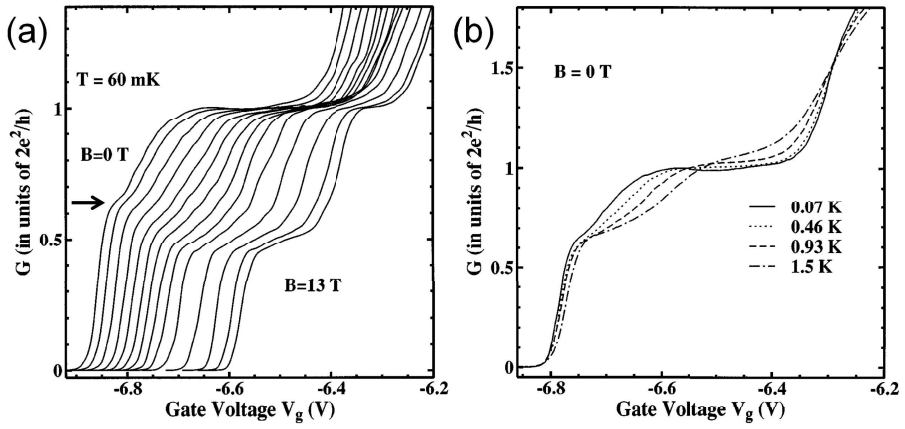

Fig. 2.8 (a) Evolution of the 0.7 structure as the magnetic field increases from $B = 0$ to 13 T, in steps of 1 T. Traces are offset horizontally for clarity, and the arrow marks the 0.7 structure at $B = 0\ T$. (b) Temperature dependence of the 0.7 structure at $B = 0T$. Both (a) and (b) are adapted from Ref. [81].

for which a certain device showed the 0.7 structure evolving to $0.55(2e^2/h)$ as the density was increased. Reference [88, 89] suggests that the strength and value of the 0.7 structure are not dependent on the absolute value of n_{2D}, but rather on the shape of the electrostatic potential in the region of the 1D constriction.

2.4 Double quantum wells

As discussed in Section 2.1.1, the MBE technique can engineer the band gap of GaAs-based materials by replacing a fraction, x, of Ga atoms in GaAs with Al atoms to produce $Al_xGa_{1-x}As$. Free electrons can therefore move to the GaAs/AlGaAs interface from the Si-doped AlGaAs layer, causing the boundary between the doped AlGaAs and GaAs to sink below the Fermi energy, forming a triangular well with free electrons in it. Through the same technique, double quantum wells can be grown in $Al_xGa_{1-x}As$. Figure 2.9 (a) shows the basic structure of the double quantum wells (DQW) wafer used in this work, which consists of two GaAs quantum wells (15 nm wide), separated by a 30 nm AlGaAs barrier. The two wells are sandwiched between AlGaAs spacer layers (75 nm wide) on each side. The spacer layer is wider than for the HEMT wafer, in order to increase the mobility. However, for a given density the mobility in a DQW structure is generally lower than a HEMT structure, because of increased interface-roughness scattering [78]. There are two doped AlGaAs layers (200 nm wide), above and below the wells. The above doped layer is closed with a 10 nm GaAs cap. A 1 μm wide GaAs buffer separates the active region from the substrate. An AlGaAs layer with a graded Al concentration (5 % to 33 %) is grown on top of the buffer, followed by an AlGaAs barrier, and then the lower doped layer. Figure 2.9(b) shows the band-structure diagram for a DQW wafer. The two 2DEGs form in the upper and lower quantum wells, where the conduction-band edge drops below E_F.

2.4.1 The barrier width and the tunnelling between two wells

The MBE-grown layer sequence in Fig. 2.9, contains two modulation-doped GaAs quantum wells separated by an undoped $Al_xGa_{1-x}As$ barrier. The separation of the wells (i.e. the thickness of the AlGaAs barrier) determines the physical regime in which the DQW device operates. For layer separations of more than 20 nm, the two quantum wells are essentially decoupled. Tunnelling between the two wells is inhibited and the Coulomb interaction between electrons in different wells is small. In samples with very wide barriers, $d > 200$ nm, momentum and energy are primarily transferred from one 2DEG to the other via phonons [90]. Independent contacts to the two 2DEGs can be made using the technique of selective depletion

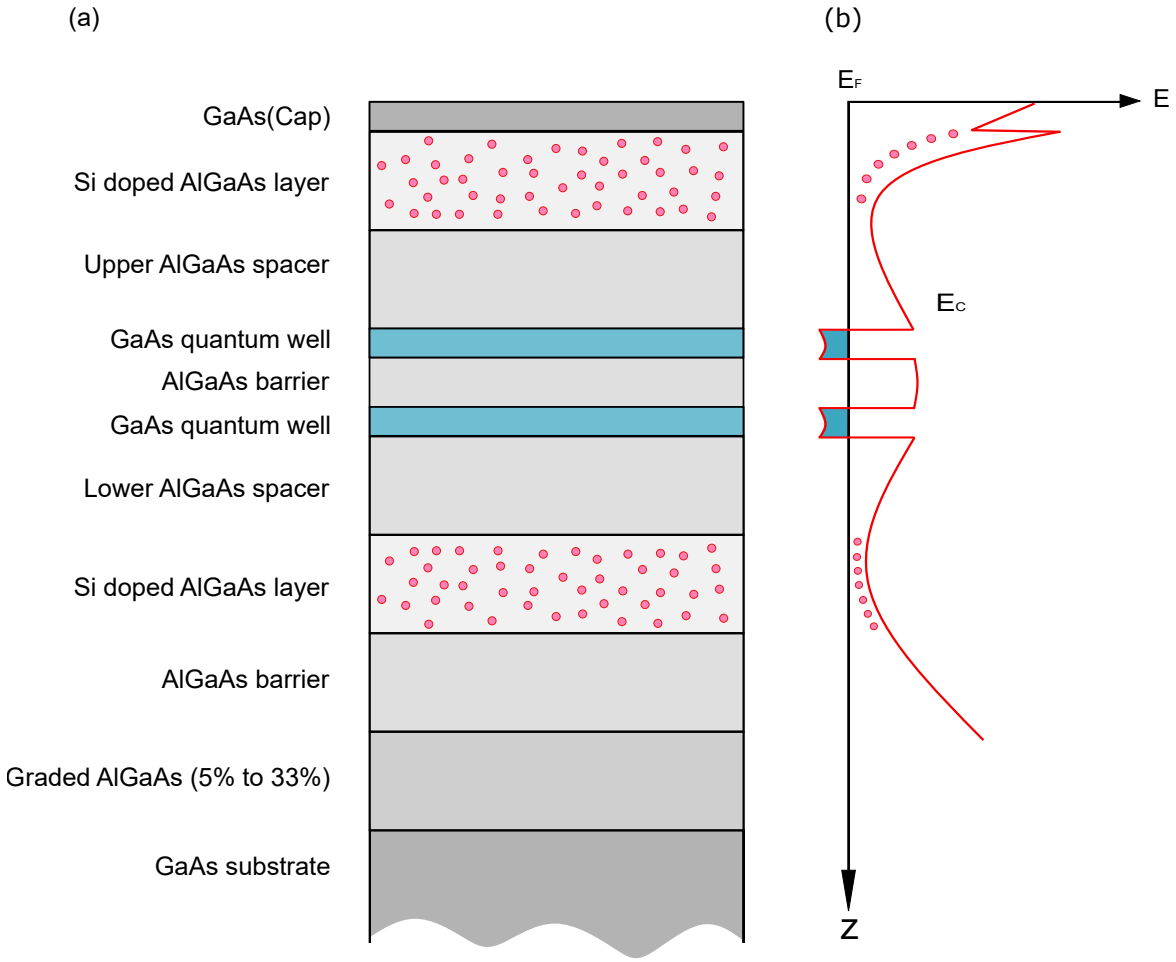

Fig. 2.9 Panel (a) shows the basic layer structure of epitaxially-grown Double Quantum Well wafers. The 2DEGs are shown in light blue. Panel (b) shows the band-bending diagram of a DQW wafer. The 2DEGs form in the two GaAs quantum wells, separated by the AlGaAs barrier. The wells are doped on either side; the red dots represent the ionised donors.

via the split-gate and middle-gate combination which will be discussed in Chapter 5. Samples with widely separated wells are used to study drag [91, 92] (momentum transfer) between electrons in the two 2DEGs. If the AlGaAs barrier thickness is reduced to less than 7 nm the layers become strongly coupled and the electronic wavefunctions in the two wells mix. It becomes inaccurate to say that an electron occupies a particular well (upper or lower); the particles occupy the symmetric and antisymmetric subbands of the double-well potential. The symmetric/antisymmetric subbands are analogous to the bonding/anti-bonding molecular orbitals formed from the distinct atomic orbital as two atoms are brought together. The previously degenerate groundstate is split; the splitting Δ_{SAS} is proportional to the overlap of the original upper/lower eigenstates [90]. Because the layers are so closely coupled, it makes no sense to form independent contacts. Samples with strongly coupled 2DEGs have

an interesting, disconnected Fermi surface [93] in parallel field, and form new quantum-Hall states [94] in perpendicular magnetic fields.

To make measurements of tunnelling between parallel 2DEGs requires devices containing two isolated, yet very closely spaced 2DEGs. An $Al_xGa_{1-x}As$ barrier of around 10 nm is sufficient to isolate the layers and prevent wavefunction mixing, but thin enough that there is a small amount of wave function overlap and tunnelling is not completely inhibited [90]. Turner *et al.* chose the barrier widths of 10 nm, 12 nm and 12.5 nm to measure resonant tunnelling between parallel 2DEGs [95].

The strong constraints imposed by energy and momentum conservation in two dimensions can potentially lead to very sharp features in the dependence of the equilibrium tunnelling conductance on the sheet densities in the quantum wells and on the strength of an in-plane magnetic field [96]. The two conservation requirements can be combined, and restated as a condition for the 2D subband energies to be aligned in both wells before tunnelling is allowed. If the left- and right- hand in both wells are denoted by the subscripts 1 and 2 respectively,

$$\left.\begin{array}{c} E_1(k_1) = E_2(k_2) \\ k_1 = k_2 \end{array}\right\} E_{0_1} = E_{0_2}, \tag{2.33}$$

expresses the energy and momentum conservation in terms of the subband energies. In the case of 2DEGs with different carrier densities in equilibrium, the conditions for tunnelling are not met. Momentum cannot be conserved by particles tunnelling at the Fermi level, and the tunnelling conductance can be low. There are two ways in which the tunnelling device can be brought onto resonance.

2.4.2 Resonance by the carrier density variation

Altering the gate voltages that control the carrier densities in the two wells will shift the bottom of the conduction band on one side of the barrier relative to the other. In the absence of a DC bias, the chemical potential is the same on both sides of the barrier, in which case the resonance condition (Equation 2.33) will be satisfied when there are equal densities in both 2DEGs. The equilibrium tunnelling conductance is therefore high at matched carrier densities. To calculate the conductance of resonant tunnelling between two wells, it is necessary to introduce the spectral function. The spectral function $A(k,E)$ is proportional to the probability that an electron in k-space should have energy E. In the absence of scattering between k-states, the lifetime of an electron is infinite and the state has a well-defined energy. The spectral function, in this case, takes the form of a delta function; $A(k,E) = 2\pi\delta(E-E_k)$, where $E_k = \hbar^2k^2/2m^*$ is the free-particle energy measured from the bottom of the 2D subband.

In the general case, $A(k,E)$ is strongly peaked at $E = E_k$, but a finite lifetime τ (e.g. due to disorder scattering) will broaden the k-space [95].

Tunnelling accesses the single-particle density of state (DOS) (the DOS available for the addition of another electron), compared to conventional transport measurement which provide information about the DOS available for the excitation of an electron from the Fermi sea into a conducting state. Zheng and MacDonald [96] showed theoretically that 2D-2D tunnelling characteristics in zero magnetic field can be used to determine the spectral function of an electron. Within layer i ($i = 1,2$ corresponds to the upper and the lower layers respectively) scattering introduces an energy broadening $\Gamma_i = \hbar/2\tau_i$, where τ_i is the scattering time. In the Born approximation the spectral function within each 2DEG will have the Lorentzian form [95],

$$A(k,E) \propto \frac{1}{\Gamma_i^2 + (\frac{\hbar^2 k^2}{2m^*} - E)^2}, \tag{2.34}$$

where E is measured from the bottom of the 2D subband. Using standard notation the tunnelling current $I(V_{SD})$ between the two layers is calculated from the two spectral functions to be

$$I(V_{sd}) \propto \int d^2k_1 \int d^2k_2 |T_{k_1,k_2}|^2 \int dE \\ A_1(k_1, E - E_{0_1}) A_2(k_2, E - E_{0_2}) \times [f(E-\mu_1, T) - f(E-\mu_2, T)], \tag{2.35}$$

where $f(E,T) = 1/[1+\exp(E/k_BT)]$ is the Fermi distribution function. The chemical potentials μ_i and the 2D subband energies E_{0_i} are defined in Fig. 2.10(a). The integral is simplified by the following assumptions: the absolute conservation of momentum (such that the interlayer tunnelling matrix element T_{k_1,k_2} is proportional to δ_{k_1,k_2}), low temperature ($k_BT \ll \Gamma$, with Fermi functions approximated by step functions), and weak disorder ($\Gamma \ll E_F$). Using these assumptions, substitution of Lorentzian spectral functions into Eq. 2.35 gives the tunnelling current,

$$I(V_{SD}) = \frac{G_0 \Gamma^2}{\Gamma^2 + (\Delta E_F + eV_{SD})^2} V_{SD}, \tag{2.36}$$

where $\Delta E_F = E_{F_2} - E_{F_1}$, and G_0 is a constant with the dimensions of conductance. The tunnelling linewidth is the sum, $\Gamma = \Gamma_1 + \Gamma_2$, of the widths of the Lorentzian spectral functions in the two layers. The zero-bias conductance obtained by differentiating Eq. 2.35 is

$$G(V_{SD} = 0) \propto \int d^2k A_1(k, E_{F_1}) A_2(k, E_{F_2}). \tag{2.37}$$

Using Lorentzian spectral functions, the differential conductance as one subband edge (controlled by a gate voltage V_g) is swept past the other is

$$G(V_g) = G_0 \frac{\Gamma^2}{\Gamma^2 + \Delta E_F^2}. \tag{2.38}$$

This predicts Lorentzian gate characteristics $G(V_g)$ with a linewidth Γ and peaked with magnitude G_0 at $\Delta E_F = 0$, when the carrier densities in the two wells are equal. Figure 2.10 (b) shows the zero-field differential tunnelling conductance G as a function of V_{g1}, the front gate voltage; by fixing V_{g2}, the carrier density in the bottom layer was held constant. The equilibrium measurements were taken at $T = 3.0K$ (squares) and $T = 19.0K$ (circles). The data at the two temperatures have been fitted to the Lorentzian line shape

$$G(V_{g1}) = \frac{G_0}{1 + (\frac{V_{g1} - V_0}{\delta V_g})^2}, \tag{2.39}$$

which is Eq. 2.38 rewritten explicitly in terms of the front-gate voltage V_{g1} [95].

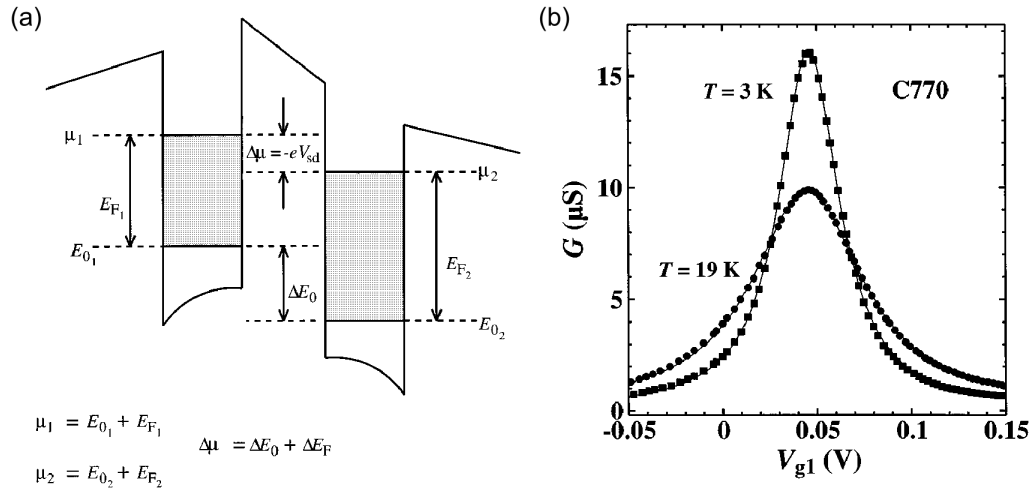

Fig. 2.10 (a) Conduction-band profile of the double-2DEG structure. (b) Equilibrium tunnelling conductance $G(V_{SD} = 0)$ as a function of the gate voltage V_{g1} controlling the carrier density in the upper layer, when the lower-layer density is fixed at $n_2 = 3.25 \times 10^{11}\,\mathrm{cm}^{-2}$. The traces were taken at $T = 3\,\mathrm{K}$ (squares) and $T = 19\,\mathrm{K}$ (circles), and the solid lines are the fits to Eq. 2.39. This figure is adapted from Ref. [95]

2.4.3 Resonant tunnelling in an in-plane magnetic field

Another commonly used technique, in double-quantum-well tunnelling measurements, is to apply in-plane magnetic field. It can not only give the shape of the Fermi surface [97] but also provide extra information concerning the individual 2DEGs. In particular, the scattering rates in the upper and lower 2DEGs can be determined independently, rather than an average rate [95].

In k-space a parallel magnetic field $B_{||}$ shifts the origins of the Fermi circles in the upper and lower layers with respect to one another. The displacement is propertional to the transverse momentum given to a classical particle, by the Lorentz force, as it traverses the barrier between the 2DEGs. The origin of the upper Fermi circle is shifted (along the x-axis if the field is applied along the y-axis) by an amount $k_B = edB_{||}/\hbar$, as shown in Fig. 2.11.

In the situation depicted in Fig. 2.11(b), very few states at the Fermi level in one 2DEG coincide in k-space with states at the Fermi level in the other; the displaced Fermi circles intersect in only two places in k-space. A parallel magnetic field suppresses resonant tunnelling at matched density. However, by altering the carrier densities, the overlap of the Fermi circles can be increased; this results in two resonant peaks in the tunnelling conductance, as a function of E_F or $B_{||}$. There are two conditions, as shown in Fig. 2.11(a) and (b), under which the Fermi circles are mutually tangential; intuitively, the overlap of the Fermi circles should be maximal and the tunnelling conductance should show a peak at these two points. Assuming $B_{||}$ and k_{F2} are fixed, and k_{F1} is being varied by sweeping a gate voltage, the touching condition is satisfied when $k_{F1} = k_{F1}^{\pm}$, where $k_{F1}^{\pm} = k_{F2} \pm k_B$. Here k_{F1} corresponds to the carrier density in the upper layer, and k_{F2} the lower. The touching condition can be expressed in terms of carrier density and magnetic field; two relationships

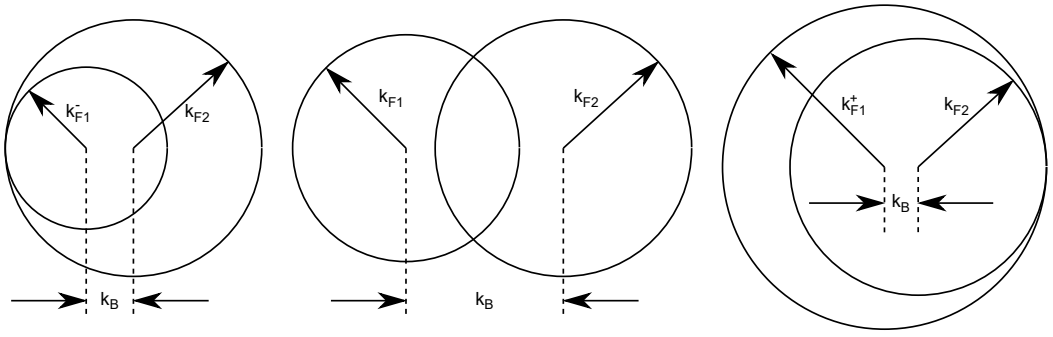

Fig. 2.11 The shift of one Fermi circle relative to the other by an in-plane magnetic field. The k vector of upper layer is changed via varying its carrier density. Panel (a) and (b) show the cases of mutually tangential Fermi circles of double quantum wells.

involving $n_1^{\pm} = (k_{F1}^{\pm})^2/2\pi$ can be expressed in terms of the other quantities [90],

$$n_1^+ - n_1^- = \frac{4ed}{\hbar}\sqrt{\frac{1}{2\pi}} \times B_{\|}\sqrt{n_2}, \tag{2.40}$$

$$\frac{n_1^+ - n_1^-}{2} = n_2 + \frac{e^2 d^2}{2\pi\hbar^2} B_{\|}. \tag{2.41}$$

i.e. the separation of the peaks split by the in-plane field and the average peak position.

Equation 2.40 and 2.41 describe the average peak positions and splitting only very approximately. There is no simple analytical expression for the tunnelling conductance in these circumstances, but Turner [90] applied the same methods as used in zero field to formulate an appropriate expression for the low temperature tunnelling conductance,

$$G(E_{F1}, E_{F2}; V_{sd} = 0) \propto \int d^2k A_1(k, E_{F1}) A_2(k - k_B, E_{F2}). \tag{2.42}$$

The equilibrium conductance is proportional to the overlap of two Lorentzian spectral functions (at the Fermi energies of the two layers), one Fermi circles having been displaced in the x-direction. Figure 2.12 shows results for the layer density dependence of the conductance at zero magnetic field and at several nonzero values of in-plane magnetic field [96].

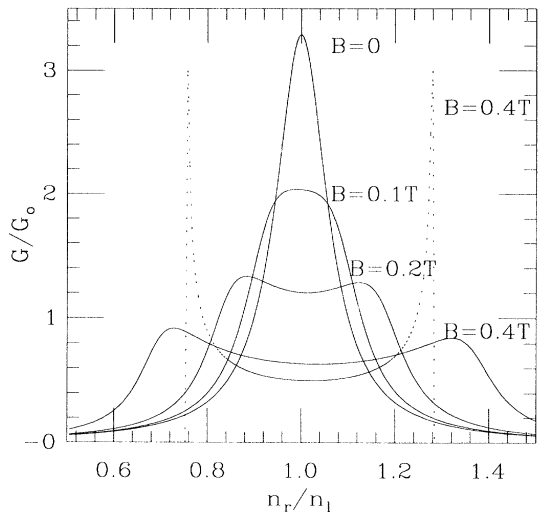

Fig. 2.12 Tunnelling conductance vs the ratio of electron densities in the two layers ($n_l = 0.9 \times 10^{11} cm^{-2}$). The dashed line shows the result obtained in the absence of disorder at $B = 0.4T$, $G_0/A = 0.9 \times 1.0^2(m^{*2}e^2t^2/\pi^4\hbar^5 n_l)$. This figure is adapted from Ref. [96].

2.5 Inelastic scattering of 2D electrons

The low-temperature mobility of semiconductor electron gases is limited by elastic scattering from impurities. However, the inelastic scattering has more importance to the work presented in this thesis, which is necessary for a 2DEG to be able to exchange energy with its environment and to achieve thermal equilibrium. This section briefly introduces several inelastic scattering mechanisms.

2.5.1 Electron-electron scattering

In low temperature 2D electron gases with finite disorder, electron-electron scattering is found to be dominated by two processes. The first is likened to a single electron scattering from the random, noise-like fluctuations in the background charge due to all the other electrons [98]. This is known as Nyquist scattering and it transfers only small amounts of energy between pairs of electrons, compared to the temperature or their excess energy, and after a few collisions the phase is randomized. The scattering rate in this mechanism is $\tau_{\phi N}^{-1} \propto T^{2/(4-d)}$, where d is the dimensionality of the system ($d = 1, 2$) [99] - in a 2D electron gas (2DEG) this rate is:

$$\tau_{\phi N}^{-1} = \frac{k_B T}{2\pi\hbar} \frac{\lambda_F}{l_e} \ln\left(\frac{\pi\lambda_F}{l_e}\right), \tag{2.43}$$

where λ_F is the Fermi wavelength and l_e is the elastic mean free path [100]. The second scattering mechanism transfers energy comparable with the temperature or the scatterers' excess energy [101–103]. For this process, the lifetime for an electron with an excess energy ε above the Fermi energy (ε_F) of a 2DEG at a temperature T is given by [101]:

$$\tau_{e-e}^{-1}(T) = -\frac{\pi\varepsilon_F}{8\hbar}\left(\frac{k_B T}{\varepsilon_F}\right)^2 \ln\left(\frac{k_B T}{\varepsilon_F}\right) \text{ [for } \varepsilon_F \gg k_B T \gg \varepsilon] \,, \tag{2.44}$$

$$\tau_{e-e}^{-1}(\varepsilon) = -\frac{\varepsilon_F}{8\hbar}\left(\frac{\varepsilon}{\varepsilon_F}\right)^2 \ln\left(\frac{\varepsilon}{\varepsilon_F}\right) \text{ [for } \varepsilon_F \gg \varepsilon \gg k_B T] \,. \tag{2.45}$$

Measurements of electron dephasing have explored the behaviour of these scattering mechanisms and broad agreement with theory is found [100, 104, 105]. Quantitative agreement with the predicted large-energy-transfer scattering rate (i.e. the combination of Equations 2.44 and Equation 2.45, but excluding Nyquist scattering) has also been measured directly by tunnelling spectroscopy [95, 106].

2.5.2 Electron-phonon scattering

Phonons are the quanta of vibrations of the ions of the lattice away from the positions of minimum energy. In a crystal with more than one atom per unit cell, the spectrum of phonon states has multiple branches. These are divided into *acoustic* and *optical* branches [107]. For an acoustic phonon the atoms in a unit cell move in the same direction by almost the same distance, while for an optical phonon they vibrate towards their neighbours. Acoustic phonons have zero energy at zero wavevector, while optical phonons always have some minimum energy, and a higher energy than acoustic phonons of the same wavevector. In GaAs, the energy of (longitudinal) optical phonons is approximately 36 meV [108]. At temperatures $T \ll 100K$, mostly acoustic phonons will be present [109]. At the energies and temperatures we are concerned with in this thesis, it is safe to neglect optical phonons entirely.

Acoustic phonons give rise to a perturbing potential in two different ways: the *deformation-potential interaction* and the *piezoelectric interaction*. In the first, small changes in the relative positions of the atoms perturb the electrostatic potential experienced by the electrons, resulting in a change in the electron energy. In the second way, changes in the relative positions of oppositely charged ions, such as Ga and As, produce an electric polarization and hence long-range electric field which again affects the electron energy [109]. The relative importance of the two interactions depends on temperature, and for a GaAs 2DEG, the piezoelectric interaction dominates below approximately 2.5 K [110].

In the temperature range where optical-phonon modes are not thermally populated ($\ll 100K$), the strength of electron-phonon scattering in a 2D electron gas splits into two regimes: *equipartition* and *Bloch-Grüneisen*. In the first, k_BT in much greater than the energy of phonons with a wave vector of $2k_F$ (k_F is the Fermi wave vector of the electron gas). There is therefore a thermal population of phonons available over the whole range of electron energies. The thermal occupation of phonons results in an energy of approximately k_BT per phonon mode, hence the name *equipartition*. The energy relaxation rate of 2D electrons in this regime is proportional to T. With temperature falling, short-wavelength phonons ($q \approx 2k_F$) cease to contribute to the electron-phonon scattering processes, and only electron-phonon scattering with small angles remains ($q < 2k_F$) [111]. This is the Bloch-Grüneisen regime, where the electron-phonon scattering becomes dramatically suppressed by the decreasing availability of empty states near the Fermi surface of the electron gas. The crossover temperature between these two regimes is the *Bloch-Grüneisen temperature*, which is defined as $T_{GB} = 2\hbar v_s k_F/k_B$, where v_s is the tranverse sound velocity and k_F is the Fermi wave vector [112]. For a typical high-mobility 2DEG of carrier density of $(1-2)\times 10^{11}\mathrm{cm}^{-2}$, the transition temperature is $T_{GB} \approx 5-8$K [113]. The transition from a high-temperature

to a low-temperature regime can be viewed as a result of the phase-space restriction for electron-phonon interaction processes imposed at temperatures less than T_{BG} [111].

In Bloch-Grüneisen regime, the function form of the energy relaxation rate is expected to be T^n, where $n = 7$ for screened deformation potential and $n = 5$ for a screened piezoelectric mechanism. The unscreened deformation potential and piezoelectric mechanism occur with $n = 5$ and $n = 3$, respectively [112]. Since the screening radius is usually larger than the Fermi wavelength, the temperature below which screening is significant is lower than the cross-over to the Bloch-Grüneisen regime. In typical-density GaAs 2DEGs, this temperature is expected to be approximately 4 K [112].

All the experiments that will be presented in this thesis were performed at temperatures less than 0.5 K. We therefore expect electron-phonon scattering to be dominated by a screened piezoelectric interaction with acoustic phonons in the Bloch-Grüneisen regime. In this case, the energy-loss rate from a 2D electron gas at a temperature T_e to phonons at temperature T_l is predicted to be [110, 114]:

$$\dot{Q}_P = \sum A(T_e^5 - T_l^5), \tag{2.46}$$

where A is the area of the 2DEG, and $\sum$ is a material-dependent parameter. Including the effect of phonon spectrum anisotropy in GaAs, $\sum$ is found to be [114, 115]:

$$\sum = (43.3n^{-1/2}) f W \mu m^{-2} K^{-5} \tag{2.47}$$

where n is the 2DEG carrier density in units of $10^{11}\mathrm{cm}^{-2}$. Experimental results have shown reasonable agreement with these theoretical predictions [112, 116–118].

The weak electron-phonon coupling also makes it possible to locally increase the temperature of a 2DEG using a local source of heat. This has been used as a tool to study the thermal conductance and thermopower of various devices, as well as energy relaxation of hot 2D electrons [119–124]. This usual technique is to pass a current through a long, narrow region of a 2DEG. This balance between Joule heating in the channel and thermal conduction out of its ends results in an increase in T_e at its middle. A device placed in contact with this part of the channel then has access to a hot 2D reservoir, the temperature of which is controlled by the heating current. By modulating the heating current at a known frequency (f), it is also possible to identify purely thermal signals in the measurement: since Joule heating depends on I^2, the temperature will be modulated at twice the frequency of the current. Any signals due to the temperature change can be detected by a lock-in measurement at a frequency of $2f$.

2.6 Thermoelectric properties of a quantum dot

In this section, our discussions will focus on the thermoelectric properties of quantum dots. It starts with the Landauer-Büttiker formalsim within the linear response and within the quantum limit, and close at how the low dimensionality affects the Wiedemann-Franz law and figure of merit ZT.

2.6.1 Landauer-Büttiker formalism of thermoelectricity

The Landauer-Büttiker formalism [125, 126] relates the transport properties of a conductor to the transmission probabilities between reservoirs that are in local equilibrium. Let us assume that only two such reservoirs are present. In equilibrium, the reservoirs are at chemical potential E_F and temperature T. In the regime of linear response, the current I and heat flow Q are related to the chemical-potential difference $\Delta\mu$ and the temperature difference ΔT by the constitutive equations [127]:

$$\begin{pmatrix} I \\ Q \end{pmatrix} = \begin{pmatrix} G & L \\ M & K \end{pmatrix} \begin{pmatrix} \Delta\mu/e \\ \Delta T \end{pmatrix}. \tag{2.48}$$

The thermo-electric coefficients L and M are related by an *Onsager relation*, which in the absence of a magnetic field is

$$M = -LT. \tag{2.49}$$

Equation 2.48 is often re-expressed with the current I rather than the electrochemical potential $\Delta\mu$ as an independent variable [127]:

$$\begin{pmatrix} \Delta\mu/e \\ Q \end{pmatrix} = \begin{pmatrix} R & S \\ \Pi & -\kappa \end{pmatrix} \begin{pmatrix} I \\ \Delta T \end{pmatrix}. \tag{2.50}$$

The resistance R is the reciprocal of the isothermal conductance G. The thermopower S is defined as

$$S \equiv (\frac{\Delta\mu/e}{\Delta T})_{I=0} = -L/G. \tag{2.51}$$

The Peltier coefficient Π, defined as

$$\Pi \equiv (\frac{Q}{T})_{\Delta T=0} = M/G = ST \tag{2.52}$$

is proportional to the thermopower S in view of the Onsager relation 2.49. Finally, the thermal conductance κ is defined as

$$\kappa \equiv -(\frac{Q}{\Delta T})_{I=0} = -K(1+\frac{S^2GT}{K}). \tag{2.53}$$

The thermo-electric coefficients are given in the Landauer-Büttiker formalism by [128, 129]

$$G = -\frac{2e^2}{h}\int_0^\infty dE \frac{\partial f}{\partial E} t(E), \tag{2.54}$$

$$L = -\frac{2e^2}{h}\frac{k_B}{e}\int_0^\infty dE \frac{\partial f}{\partial E} t(E)(E-E_F)/k_BT, \tag{2.55}$$

$$\frac{K}{T} = \frac{2e^2}{h}(\frac{k_B}{e})^2\int_0^\infty dE \frac{\partial f}{\partial E} t(E)[(E-E_F)/k_BT]^2. \tag{2.56}$$

These integrals are convolutions of the transmission probability $t(E)$, which characterises the conductor, and a kernel of the form $\varepsilon^m df/d\varepsilon$, $m = 0, 1, 2$, with $\varepsilon \equiv (E-E_F)/k_BT$, and f the Fermi function: $f(\varepsilon) = [\exp(\varepsilon)+1]^{-1}$ [127].

Following the discussion by X. Zianmi [130], we will next focus on the calculation of the electron thermal conductance of a quantum dot (QD) weakly coupled to two electrode leads in the sequential-tunnelling regime within linear response. Two major simplifications are applied in this model. First, virtual tunnelling processes are neglected; second, the electrostatic energy is described by the classical charging energy: $(Ne)^2/2C$, where N is the number of electrons in the dot and C is the capacitance of the surroundings. We consider a double-barrier tunnel junction. It consists of a quantum dot that is weakly coupled to two electron reservoirs via tunnel barriers. Each reservoir is assumed to be in thermal equilibrium and there are a voltage difference V and a temperature difference ΔT between the two reservoirs. A continuum of electron states is assumed in the reservoirs that are occupied according to the Fermi-Dirac distribution: $f(E-E_F) = [1+\exp[(E-E_F)/k_BT]]^{-1}$, where the Fermi energy, E_F, in the reservoirs is measured relative to the local conduction band bottom. The tunnelling rates through the left and right barriers from level p to the left and right reservoirs are denoted by Γ_p^l and Γ_p^r, respectively. It is assumed that energy relaxation rates for the electrons are fast enough with respect to the tunnelling rates that we can characterise the state of the dot by a set of occupation numbers, one for each energy level. It is also assumed that inelastic scattering takes place exclusively in the reservoirs not in the dot. The transport through the dot can be described by rate equations.

Due to the voltage difference V and the temperature difference ΔT between the two reservoirs, electric and thermal currents pass through the dot. The stationary current I and

the heat flux Q through the left barrier are respectively given by the following equations:

$$I = \frac{e}{k_B T} \sum_{p=1}^{\infty} \sum_{N=1}^{\infty} \frac{\Gamma_p^l \Gamma_p^r}{\Gamma_p^r + \Gamma_p^l} P_{eq}(N) F_{eq}(E_p/N) \times [1 - f(\varepsilon_p - E_F)][eV - \frac{\Delta T}{T}(\varepsilon_p - E_F)], \tag{2.57}$$

$$Q = -\frac{1}{k_B T} \sum_{p=1}^{\infty} \sum_{N=1}^{\infty} \frac{\Gamma_p^l \Gamma_p^r}{\Gamma_p^r + \Gamma_p^l} P_{eq}(N) F_{eq}(E_p/N)[1 - f(\varepsilon_p - E_F)] \times (\varepsilon_p - E_F)[eV - \frac{\Delta T}{T}(\varepsilon_p - E_F)], \tag{2.58}$$

where $\varepsilon_p \equiv E_p + U(N) - U(N-1)$, $P_{eq}(N)$ is the probability that the quantum dot contains N electrons in equilibrium and $F_{eq}(E_p/N)$ is the conditional probability in equilibrium that level p is occupied given that the quantum dot contains N electrons. The above equilibrium probabilities are respectively defined as

$$P_{eq}(N) = \sum_{\{n_i\}} P_{eq}(\{n_i\}) \delta_{N, \sum_i n_i}, \tag{2.59}$$

$$F_{eq}(E_p/N) = \frac{1}{P_{eq}(N)} \sum_{n_i} P_{eq}(n_i) \delta_{n_{p,1}} \delta_{N, \sum_i n_i}. \tag{2.60}$$

$P_{eq}(\{n_i\})$ is the Gibbs distribution in the grand canonical ensemble

$$P_{eq}(\{n_i\}) = Z^{-1} exp[-\frac{1}{k_B T}(\sum_{i=1}^{\infty} E_i n_i + U(N) - NE_F)], \tag{2.61}$$

where $N \equiv \Sigma_i n_i$ and Z is the partition function

$$Z = \sum_{\{n_i\}} exp[-\frac{1}{k_B T}(\sum_{i=1}^{\infty} E_i n_i + U(N) - NE_F)]. \tag{2.62}$$

By comparison of the above definitions of the transport coefficients in the previous section and the linearised expressions for I and Q, the following expressions are extracted for coefficients:

$$G = \frac{e^2}{k_B T} \sum_{p=1}^{\infty} \sum_{N=1}^{\infty} \gamma_p P_{eq}(N) F_{eq}(E_p/N)\{1 - f[E_p + U(N) - U(N-1) - E_F]\}, \tag{2.63}$$

$$S = -\frac{e}{k_B T^2 G} \sum_{p=1}^{\infty} \sum_{N=1}^{\infty} \gamma_p [E_p + U(N) - U(N-1) - E_F] \\ P_{eq}(N) F_{eq}(E_p/N) \{1 - f[E_p + U(N) - U(N-1) - E_F]\}, \tag{2.64}$$

$$K = -\frac{1}{k_B T^2} \sum_{p=1}^{\infty} \sum_{N=1}^{\infty} \gamma_p [E_p + U(N) - U(N-1) - E_F] \\ P_{eq}(N) F_{eq}(E_p/N) \{1 - f[E_p + U(N) - U(N-1) - E_F]\}, \tag{2.65}$$

where $\gamma_p \equiv \frac{\Gamma_p^l \Gamma_p^r}{\Gamma_p^r + \Gamma_p^l}$.

2.6.2 Quantum limit

In the quantum limit, where $\Delta E \gg k_B T$, the discreteness of the energy spectrum of the quantum dot plays a predominant role. In this limit, the term with $N = N_{min}$ gives the dominant contribution to the sums over N in Equation (2.57-2.58), where N_{min} is the integer that minimises the absolute value of

$$\Delta(N) = E_N + U(N) - U(N-1) - E_F. \tag{2.66}$$

Then, we define $\Delta \equiv \Delta(N_{min})$ and $\Delta_p \equiv E_p - E_{N_{min}}$.

In the quantum limit, the distribution functions for non-degenerate energy levels can be approximated by the following expressions:

$$P_{eq}(N_{min}) = \frac{1}{1 + e^{\Delta / k_B T}}, \tag{2.67}$$

$$F_{eq}(E_p/N_{min}) = \begin{cases} 1, & \text{for } p \leq N_{min}, \\ e^{-\Delta_p / k_B T}, & \text{for } p > N_{min}, \end{cases} \tag{2.68}$$

and

$$1 - f(\Delta_p + \Delta) = \begin{cases} 1, & \text{for } p > N_{min}, \\ e^{(\Delta_p + \Delta)/k_B T}, & \text{for } p > N_{min}, \\ \frac{e^{\Delta / k_B T}}{1 + e^{\Delta / k_B T}} & \text{for } p = N_{min}. \end{cases} \tag{2.69}$$

Using the above approximations in Eqs. (2.63-2.65), we obtain for G and κ for an equidistant energy-level spectrum ($E_p = p\Delta E$) and level-independent tunnelling rates, i.e., $\Gamma_p^{l,r} = \Gamma^{l,r}$:

$$G^{QL} = \frac{e^2}{k_B T}\gamma\frac{1}{4\cosh^2(\Delta/2k_BT)}, \tag{2.70}$$

$$S^{QL} = -\frac{1}{eT}[-\frac{\Delta E}{2}\mathrm{Int}(\frac{\Delta_{min}}{\Delta E}) + \Delta_{min}], \tag{2.71}$$

$$\kappa^{QL} = k_B\gamma(\frac{\Delta E}{k_BT})^2\frac{e^{-\Delta E/k_BT}}{1+4\cosh^2(\Delta/2k_BT)e^{-\Delta E/k_BT}}, \tag{2.72}$$

where $\gamma \equiv \frac{\Gamma^l\Gamma^r}{\Gamma^l+\Gamma^r}$. Here $Int(x)$ is the integer part of x for $x > 0$, and minus the integer part of $|x|$ for $x < 0$ [130].

2.6.3 Mott relation

The thermopower oscillates around zero in a sawtooth manner as a function of the Fermi energy [67]. For Equation (2.71), since $|\Delta_{min} \leq \frac{1}{2}(\Delta E + e^2/C)|$, it reduces to $S = -\Delta_{min}/eT$ if $e^2/C \leq \Delta E$. The thermopower thus has only the long-period oscillations (consisting of a sawtooth with periodicity $\Delta E + e^2/C$ and amplitude $(\Delta E + e^2/C)/eT$), if the charging energy is less than the level spacing. The short-period oscillations appear as soon as $e^2/C > \Delta E$. For $e^2/C \gg \Delta E$, the short-period oscillations are a fine structure on the envelope $S_{envelope} = -\Delta_{min}/2eT$, obtained from the classical expression of the thermopower [67].

The periodicity of the thermopower oscillations is the same as that of the Coulomb-blockade oscillations in the conductance, but the amplitude and lineshape of the thermopower oscillations are different [67]. When both charge and heat are exclusively carried by electrons, it has been shown both for diffusive and ballistic transport that the thermopower S is related to the energy derivative of the conductance G [116]:

$$S = \left.\frac{\Delta V}{T_C - T_L}\right|_{\mathrm{I}=0} = -\frac{\pi^2 k_B^2}{3e}(T_C + T_L)\frac{\partial \ln G}{\partial E_F}. \tag{2.73}$$

where μ is the chemical potential of the contacts relative to 2DEG regions of interest. It is assumed that features in the thermopower are not subject to thermal broadening, and that the electrons are noninteracting [116]. This is also called the *Mott relation*.

Beenakker and Staring [10] computed the thermopower of a quantum dot from Eq. (2.64) for parameters between the classical and the quantum regimes, and plotted the results in figure 2.13 (a) and (b). Notice that in figure 2.13(b) the slope $dS_{envelope}/dE_F = \frac{1}{2eT}$ of

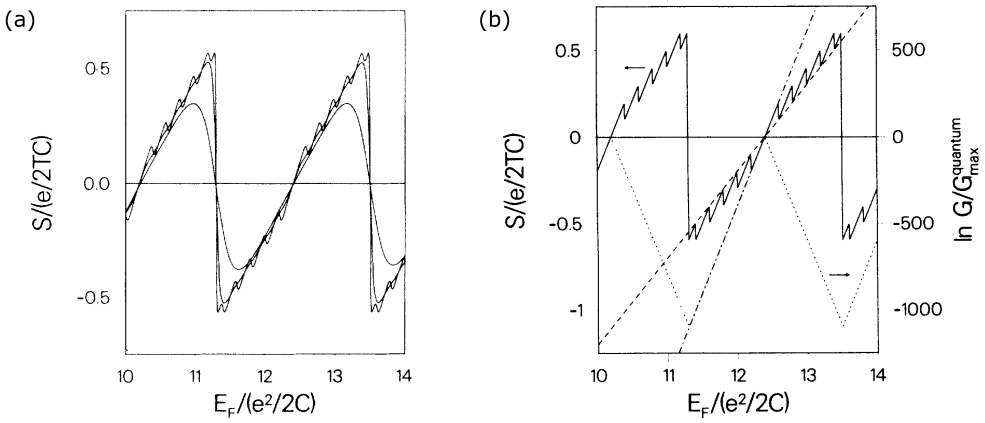

Fig. 2.13 (a) Development of fine structure on the thermopower oscillations on lowering the temperature from $k_BT = (0.2 \text{ to } 0.05 \text{ to } 0.01) \times e^2/2C$. The curves are computed from Eq. (2.64), for a series of equidistant nondegenerate levels with $\Delta E = 0.2e^2/2C$, taking level-independent tunnel rates. (b) Low-temperature limit of the thermopower oscillations of panel (a) (solid curve). The conductance oscillations are shown for comparison (dotted). The curves are computed from Eqs. (2.63) and (2.64), for a series of equidistant non-degenerate levels with $\Delta E = 0.2e^2/2C, k_BT = 0.001e^2/2C$, and taking level-independent tunnel rates. The dash-dotted line has slope $dS/dE_F = 1/eT$, and the dashed line has a slope which is twice as small [10].

the envelope (dashed) is twice as small as the slope $dS/dE_F = 1e/T$ of the piecewise-linear segments (dash-dotted). The conductance (calculated from Eq. (2.63)) is plotted in the same figure, for comparison (dotted curve). The fine structure in thermopower has a corresponding fine structure in the conductance, consisting of a step-like feature with periodicity ΔE. The steplike fine structure on the conductance is however not visible, because of its exponentially small magnitude. The spacing of the fine structure is determined by the level spacing, and is only equally spaced if the levels themselves are equally spaced [10].

2.6.4 Violation of the Wiedemann-Franz law

The thermal conductance κ is defined by $Q = \kappa T$ for $I = 0$, i.e., $\kappa = K - GTS^2$. For macroscopic samples of ordinary metals, the Wiedemann-Franz law provides a universal relation between the two conductances by stating that the Lorenz ratio

$$L \equiv \frac{\kappa}{GT}, \tag{2.74}$$

is a constant given by the Lorenz number $L_0 = (\pi^2/3) \times (k_B/e^2)$. It is a consequence of Fermi-liquid theory, which is applicable when screening renders Coulomb interactions sufficiently

weak. The Wiedeman-Franz law indicates that both charge and heat currents are supported by the same underlying scattering mechanisms with only weak energy dependence [131]. The situation is fundamentally different in mesoscopic systems in which level quantisation and Coulomb interaction drastically affect transport. The thermopower has been measured in small dots with discrete level spectrum [123], chaotic dot [132], carbon nanotubes and molecules [17], and dots close to metallic (quasicontinuous) limit [121], and calculated for various mesoscopic systems [10]. Deviations from the Wiedemann-Franz law have been predicted for tunnelling transport through quantum dots for weak coupling [130, 133], in the Kondo regime [130, 134] and for open dots [135].

Erdman *et al.* studied the thermoelectric properties of an interacting quantum-dot-based heat engine [136]. Using Equ. (2.63-2.65), they find that for the interacting case:

$$L = \frac{L_0}{\pi}(\frac{\Delta E}{k_B T})^2 \begin{cases} |N|(|N|+2), & \text{if } N \neq N_{min} \\ 12e^{-\Delta/k_B T}, & \text{if } N = N_{min}, \end{cases}; \tag{2.75}$$

and for the non-interacting model:

$$L_{NI} = L_0(\frac{\Delta E}{k_B T})^2 \frac{24}{\pi^2} e^{-\Delta/k_B T} \cosh^2(e^{\Delta_{min}/2k_B T}) \cosh(e^{\Delta_{min}/k_B T}). \tag{2.76}$$

In both cases, the Wiedemann-Franz Law is strongly violated; At Δ_{min}, the Lorenz ratio is exponentially smaller than L_0 thanks to the factor $(\Delta E/k_B T)^2/\exp(\Delta E/k_B T)$. In both cases the Lorenz ratio exponentially increases with Δ_{min}. In the non-interacting model the exponent is $2\Delta_{min}/(k_B T)$ (twice the interacting case), and the maximum value, achieved at $\Delta_{min} = \Delta E/2$, is the of the order of $L_{NI} \approx (\Delta E/k_B T)^2 L_0$. Interesting, in the interacting case, when $|\Delta_{min} > \Delta E|, i.e., N \neq N_{min}$, they find plateaus whose height increases with N [136].

Kubala *et al.* discussed the violation of the Wiedemann-Franz Law in a single-electron transistor [131], and showed that the Coulomb interaction with weak tunnel couplings affects the Wiedemann-Franz law in two ways. First, the finite charging energy to add or remove an electron to or from the island suppresses some transport processes. This dramatically affects the charge and thermal conductance individually, but leaves the Wiedemann-Franz law untouched since the same transport processes are suppressed for both electric and thermal conductance. Second, however, Coulomb interaction leads to a strong energy dependence of the scattering processes. This yields, in general, a violation of the Wiedemann-Franz law [131].

Figure 2.14 shows the analytical results for the dimensionless thermoelectric coefficients, $g_V, g_T = M, K$, and the Lorenz ratio L normalised by L_0, as a function of gate voltage for

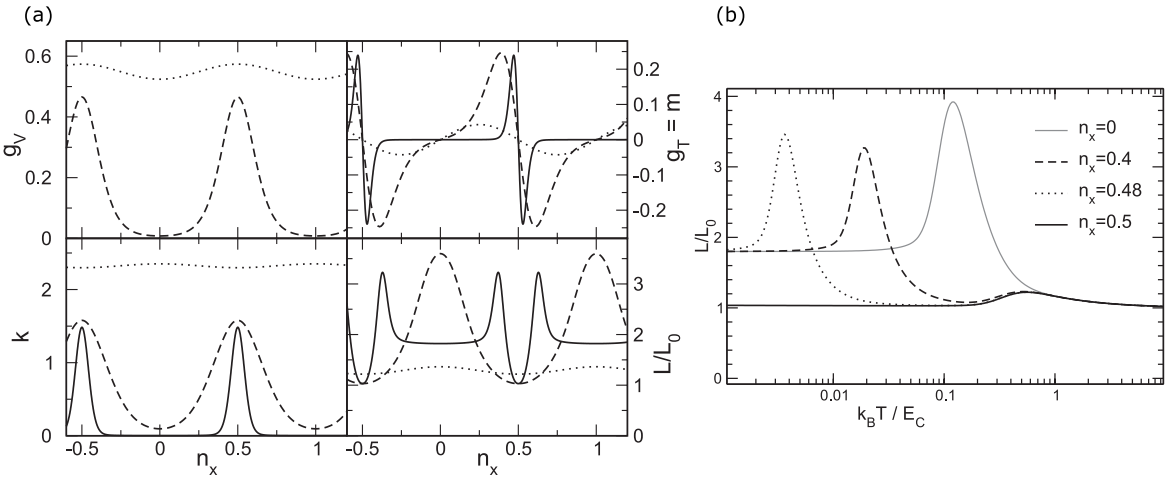

Fig. 2.14 (a) Coulomb blockade oscillations of thermoelectric coefficients and the Lorenz ratio. For high temperatures ($k_BT = E_C/2$ – dotted line) oscillations are washed out. In the sequential-tunnelling regime ($k_BT = E_C/10$ – dashed line) the Lorenz ratio is given by Equ. 2.78 around each resonance. For low temperatures ($k_BT = E_C/40$ – solid line) the new universal Lorenz ratio $9/5L_0$ is reached in the co-tunnelling regime. (b) Temperature dependence of Lorenz ratio for different gate voltages. Two maxima separate different tunnelling regimes. The rise to the maxima starts at $k_BT \approx E_C$ and $k_BT \approx \Delta_0$, respectively. For $n_x = 0 \Longleftrightarrow \Delta_0 = E_C$ the two maxima coincide, whereas at resonance ($n_x = 5 \Longleftrightarrow \Delta_0 = 0$) the lower maximum is moved to the left. The figure is adapted from Ref [131].

various temperatures, as well as the temperature dependence of L/L_0 for various gate voltages. The tunnel coupling is chosen as $\alpha_0^{L/R} = 0.01$. Temperature and gate-voltage dependence of the Lorenz ratio can be elucidated by deriving analytical expressions for various limits. (i) In the high-temperature regime, $E_C/k_BT \ll 1$, Coulomb oscillations are washed out; i.e., there is no gate-voltage dependence. To calculate corrections to the Wiedemann-Franz law in this regime, they expanded the gate-voltage average of all thermo-electric coefficients in powers up to $(E_C/k_BT)^2$ to find

$$\frac{L}{L_0} = 1 + \frac{2}{\pi^2} E_C/k_BT - \frac{1+24\alpha_0}{3\pi^2} (E_C/k_BT)^2. \tag{2.77}$$

Deviations from the Wiedeman-Franz law are visible before Coulomb oscillations set in, see Fig. 2.14(b), where for $k_BT \geq E_C$ the curves coincide for all gate voltages while $L > L_0$. (ii) In the on-resonance low-temperature regime, $E_C/k_BT \gg 1$ but $\Delta N \ll 1$ for one N (say $N = 0$), transport is dominated by sequential tunnelling and only the charge states 0 and 1 occur. The sequential-tunnelling contribution then yields

$$\frac{L}{L_0} = 1 + (\Delta_0/k_BT)^2/(2\pi)^2, \tag{2.78}$$

The Wiedemann-Franz law is only fulfilled for a vanishing charging-energy gap, $\Delta_0 = 0$, with corrections quadratic in Δ_0/k_BT away from resonance. These corrections indicate that the contribution of each transported particle to the heat current scales with the charging-energy gap Δ_0 instead of temperature k_BT as in bulk transport. In the off-resonance low-temperature regime, transport is dominated by co-tunnelling. Because of the weak energy dependence of the co-tunnelling scattering rate, proportionality between charge and heat conductance is recovered, however, with a different prefactor, as $L/L_0 = 9/5$.

2.6.5 Figure of merit

The efficiency of a device to convert heat into electricty and vise versa is measured by the dimensionless figure of merit of ZT given by

$$ZT = \frac{S^2GT}{\kappa}. \tag{2.79}$$

There are two contributions to κ: the electronic, κ_e, and the phonon, κ_{ph}. Good thermoelectric materials are considered to be those with $ZT > 3$ at room temperature [133]. Early theoretical work pointed out the possibility of enhancing ZT in structures of reduced dimensionality due to increased density of states near the Fermi level [7]. Mahan and Sofo [9] predicted a maximization of the thermoelectric efficiency in materials with a delta-like density of states. This suggests that quantum dots and molecular junctions are promising candidates for good thermoelectric materials.

Tsaousidou and Triberis [133] made a comprehensive analysis of the thermoelectric properties of a weakly coupled multi-level quantum dot in the sequential-tunnelling transport regime and suggests the possibility of a huge increase of ZT in the Coulomb-blockade regime due to the violation of the Wiedemann-Franz law. They found that ZT shows two strong maxima at $\Delta_{min}/k_BT = \pm 2.4$ of magnitude

$$(ZT)^{max} = \frac{(S^2GT)^{max}}{\kappa_e} = 0.44\exp(\Delta\varepsilon/k_BT)/(\Delta\varepsilon/k_BT)^2. \tag{2.80}$$

The structure of ZT is shown in Fig. 2.15(c). The exponential dependence of these maxima can be readily explained by the fact that, in the energy interval where S^2GT exhibits the peak structure shown in Fig. 2.15(a), κ_e remains constant and is shown in Fig. 2.15(b).

This shows that the thermoelectric efficiency can be dramatically enhanced by controlling the size of the dot and consequently $\Delta\varepsilon$ (the energy spacing between successive energy levels). For small dots (or molecules) the requirement that the system is in the quantum limit is fulfilled even at room temperature. Practically speaking, the quantum limit is approached

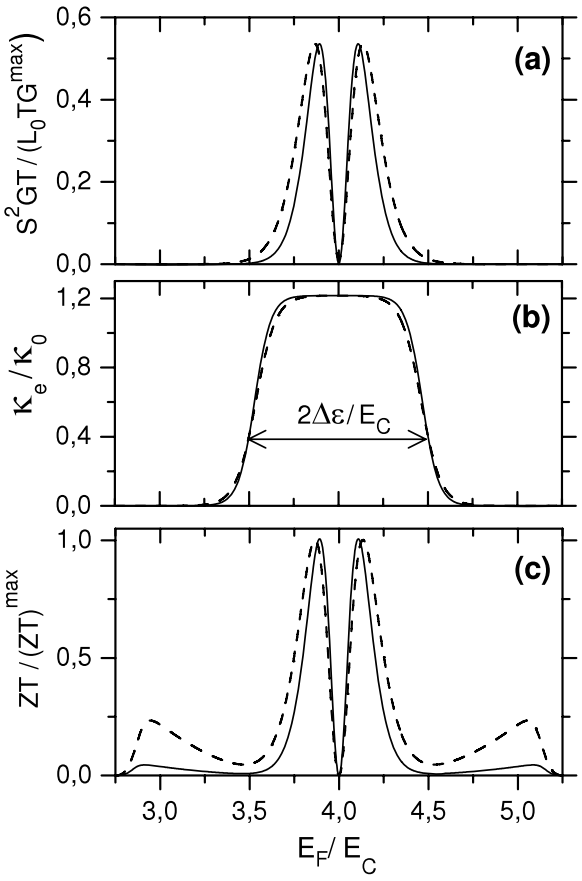

Fig. 2.15 Calculated values of S^2GT, κ_e and ZT as a function of E_F for a three-level dot. The level spacing is $\Delta\varepsilon = 0.5E_C$. The solid and dashed lines correspond, respectively, to $\Delta\varepsilon/k_BT = 11$ and 9. The results are plotted around $E_F = 4E_C$ that corresponds to $\Delta_{min} = 0$ when an electron enters the dot at the level $n = 2$. In (b) $\kappa_0 = L_0TG^{max}(\Delta\varepsilon/k_BT)^2\exp(-\Delta\varepsilon)$ where $G^{max} = G_0/4$ and in (c) $(ZT)^{max} = 0.44\exp(\Delta\varepsilon/k_BT)/(\Delta\varepsilon/k_BT)^2$. This figure is adapted from Ref. [133].

when $\Delta\varepsilon/k_BT \gg 5$. High values of ZT in the range of $2.6-97$ at $T = 300K$ ($k_BT = 0.26eV$) can be obtained when $\Delta\varepsilon$ varies between 5 and 10 k_BT (namely, between 0.13 and 0.26 eV). It is noted that the energy separation between the first two energy levels in a spherical dot for a material with electron effective mass of the order of $0.1m_e$ (m_e is the electron mass) is greater than $0.15\,eV$ when the diameter is less than 5 nm [133].

Chapter 3

A quantum-dot energy harvester

This chapter demonstrates the experimental realisation of an autonomous nano-scale energy harvester that utilises the physics of resonant tunnelling through quantum dots that are used as energy filters for electron transport. It details the theoretical proposal, design, fabrication and measurement results of this proof-concept Quantum Dot Energy Harvester (QDEH).

3.1 Theoretical proposal

Coulomb-blockaded dots can be ideally efficient converters of heat to work, both in two-terminal [13] and three-terminal [27] cases; however, since transport occurs through multiple tunnelling processes, the net current and power are very small. Thus, the physics of resonant tunnelling has attracted attention to optimise the nonlinear system [1]. Resonant tunnelling is a quantum-mechanical effect, where constructive interference permits an electron tunnelling through two barriers to have unit transmission. This is only true if the electron has a particular energy equal to the bound state in the quantum dot, or within a range of surrounding energies, whose width is the inverse lifetime of the resonant state [137]. Electrons with any other energy are effectively forbidden from being transmitted across the quantum dot. In this way, a resonant-tunnelling barrier acts like an energy filter, which only electrons that match the resonant condition are permitted to pass. For simplicity, the resonant-tunnelling barriers (of the dot) are assumed to be symmetrically coupled [1].

The geometry considered in this model is related to a quantum-dot refrigerator device, experimentally realised by Prance *et al.* [49], based on the theoretical proposal of Edwards *et al.* [47, 48]. They demonstrated that applying bias to the system results in cooling of a large $6\,\mu\mathrm{m}^2$ cavity from 280 mK to below 190 mK [49]. It is preferable to have cavities made as small as possible while still having good thermal contact with the heat source. This

further miniaturization permits many heat engines to be put in parallel and give a large output power [1].

3.1.1 Model

Figure 3.1 shows the model considered in this proposal [1]. It consists of a central cavity connected to a quantum dot on either side, each with a resonant level of width γ and energy $E_{L,R}$. These two quantum dots are assumed to have the same widths and are tuned to have different energy levels by gate voltages. The energy difference $\Delta E = E_R - E_L$ is an important energy scale of this composite system, and is referred to as the energy gain. It is distinct from the level spacing δ in the individual dots as well as from the level width. The central cavity is considered to be in equilibrium with a heat reservoir of temperature T_C that is hotter than the left and right electron reservoirs with chemical potentials $\mu_{R,L}$ and equal temperatures $T_L = T_R$. Electrons that enter and leave the cavity are assumed to relax their energies through strong electron-electron interactions. Therefore, the cavity's occupation function may be described with a Fermi function, $f(E-\mu,T) = 1/(1+\exp[(E-\mu)/k_BT])$, where μ_C is the cavity chemical potential μ_C, T_C is the cavity temperature and k_B is the Boltzmann constant. This process of inelastic energy mixing is assumed to occur on a faster time scale than the dwell time of an electron in the cavity. Thermal energy flows from the coupled hot bath into the cavity as a heat current, and keeps the temperature different from that of the electron reservoirs. The nature of the heat reservoirs is not specified in this model, but refers quite generically to any heat source we wish to harvest energy from.

The chemical potential of the cavity and its temperature (or equivalently, the incoming heat current) are constrained by conservation of global charge and energy. These constraints are given by the simple equations $I_L + I_R = 0$ and $J_L + J_R + J = 0$ in the steady state, where $I_{L,R}$ is the electrical current in the left or right contact, and $J_{L,R}$ the energy current. The energy current is seemingly not conserved because of the heat current J flowing from the hot reservoir. The currents I_j, $j = L,R$, are given by the formulas $I_j = (2e/h)\int dE T_j(E)[f_j - f_C]$ and $J_j = (2/h)\int dE T_j(E)E[f_j - f_C]$[1], where $T_j(E)$ is the transmission function of each contact for incident electron energy E. In this quantum dot geometry, the resonant levels give rise to a transmission function of Lorentzian shape [137],

$$T_j(E) = \frac{\Gamma_1\Gamma_2}{(E-E_j)^2 + (\frac{\Gamma_1+\Gamma_2}{2})^2} \tag{3.1}$$

where $\Gamma_{1,2}$ are the tunnel rates (multiplied by Planck's constant h) of the two barriers of the resonant quantum dot(s). Here we assume symmetric coupling for simplicity, $\Gamma_1 = \Gamma_2 = \gamma$,

so γ is the width of the level, or inverse lifetime of an electron in the dot. Note that the Lorentzian energy dependence applies if the level width γ is small compared to the level spacing δ in the individual quantum dots.

In the limit where the width of the level is smaller than the thermal energy in the cavity/dot system, $\gamma \ll k_B T_C, k_B T_R$, the transmission will pick out only the energies E_L or E_R in the above energy integral expressions for the currents giving simple equations. Consequently, the conservation laws for charge and energy give equations:

$$0 = f_L - f_{CL} + f_R - f_{CR}, \tag{3.2}$$

$$0 = Jh/(2\gamma) + E_L(f_L - f_{CL}) + E_R(f_R - f_{CR}), \tag{3.3}$$

where $f_L = f(E_L - \mu_L, T_R)$, $f_R = f(E_R - \mu_L, T_R)$, $f_{CL} = f(E_L - \mu_C, T_C)$, and $f_{CR} = f(E_R - \mu_C, T_C)$. From these two equations, the quantity $f_{CR} - f_R = Jh/(2\gamma\Delta E)$ can be extracted. This quantity is proportional to the electrical current through the left lead $I_L = -I_R \equiv I$, the net current flowing through the system [1].

3.1.2 The small-level-width regime of $\gamma \ll k_B T_C, k_B T_R$

In this section, the regime of $\gamma \ll k_B T_C, k_B T_R$ will be discussed. In terms of the physics of this nano-engine, an electron comes in the left lead at energy E_L and exits the right lead with energy $E_R > E_L$. Thus, in the steady state, any incoming heat current J must be associated

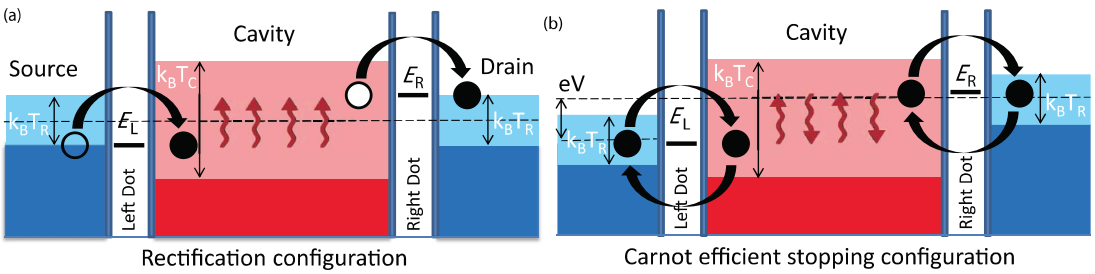

Fig. 3.1 Nanoscale heat engine created from a hot cavity connected to cold reservoirs via resonant-tunnelling quantum dots, each containing a single relevant energy level at energies E_L and E_R respectively. The cavity is kept hot through coupling to an energy reservoir at temperature T_C which is considered larger than the reservoir temperature T_R. Thermal broadening of Fermi functions in the three regions (source, cavity, and drain) is shown by the light shading. (a) Rectification configuration. In the absence of bias (short circuit), electrons enter the cavity via the left lead, gain energy $\Delta E = E_R - E_L$ from the cavity, and exit through the right lead, transferring an electrical charge e through the system. (b) Carnot efficiency stopping (open circuit) configuration. This figure is adapted from Ref. [1].

with an electrical current I, with a conversation factor of the energy gain, ΔE, to the unit of charge, e,

$$I = \frac{eJ}{\Delta E}. \tag{3.4}$$

This result holds regardless of what bias is applied or what the temperature is.

The efficiency of this heat engine, η, is defined as the ratio of the harvested electrical power $P = |(\mu_L - \mu_R)I|/e$ to the heat current from the hot reservoir, J. Therefore, for this system it can be written as,

$$\eta = \frac{|(\mu_L - \mu_R)I|}{\Delta E}. \tag{3.5}$$

In the limit of $\gamma \ll k_B T_R, k_B T_C, \Delta E$, if the cavity temperature T_C is considered to be fixed, the harvesting heat current J can be written in terms of the hot-cavity temperature and other system parameters as,

$$J = \frac{eJ}{\Delta E}[f(\Delta E/2, T_C) - f(\Delta E/2 - \mu/2, T_R)], \tag{3.6}$$

which satisfies charge and energy conservation shown in Equations (3.2) and (3.3). Importantly, without bias there is a rectified electrical current given by

$$I = eJ/\Delta E \approx \frac{e\gamma\Delta E}{4h}[(k_B T_R)^{-1} - (k_B T_C)^{-1}], \tag{3.7}$$

in the limit where $k_B T_R, k_B T_C \gg \Delta E$. Here h is Planck's constant. The current is driven solely by the fixed temperature difference between the systems. Both the heat and electrical currents are proportional to γ, the energy width of the resonant level. Consequently, the currents and power produced in this system will tend to be small since γ is assumed to be the smallest energy scale. It is also clear that both are controlled by the size of ΔE, so increasing this energy gain will improve the power until it exceeds the temperature.

In order to harvest power from this rectifier, a load should be placed across it. Equivalently, a bias voltage could be applied to this system tending to reduce the rectified current. At a particular value, μ_{stop}, the rectified current vanishes, giving the maximum load or voltage one could apply to extract electrical power at fixed temperatures T_R, T_C. This value is found when J and I vanish, given by Equation 3.5:

$$\mu_{stop} = \Delta E(1 - \frac{T_R}{T_C}). \tag{3.8}$$

Consequently, the voltage applied must not exceed μ_{stop}/e, and therefore from Equation 3.4 the efficiency is bounded by $\eta \leq 1 - \frac{T_R}{T_C} = \eta_C$. At the stopping voltage, the thermodynamic efficiency attains its theoretical maximum, the Carnot efficiency, η_C, showing this system

is an ideal nano-scale heat engine. Naturally, at this point [see Figure 3.1(b)] the system is reversible with no entropy production.

Also interesting is the efficiency at the bias point where power is maximum. For temperature larger than ΔE or $eV = \mu$, the Fermi functions can be approximated to find $P \approx (\gamma/4hk_BT_R)\mu(\mu_{stop} - \mu)$, resulting in a parabola as a function of μ, with maximum power

$$P_{max} \approx \frac{\gamma(\Delta E)^2\eta_C^2}{16hk_BT_R}, \tag{3.9}$$

and efficiency $\eta_{maxP} = \eta_C/2$, which is in agreement with general thermodynamic bounds for systems with time-reversal symmetry [5, 13].

3.1.3 Optimization

One can go beyond this limit for the efficiency by solving the conservation law in Equations (3.2) and (3.3) numerically. The total power produced by the heat engine can be optimised by varying the resonance width γ, as well as the energy gain ΔE and applied bias $V = \mu/e$, with fixed temperature T_R, T_C. These results are shown in Figure 3.2(a), where T is the

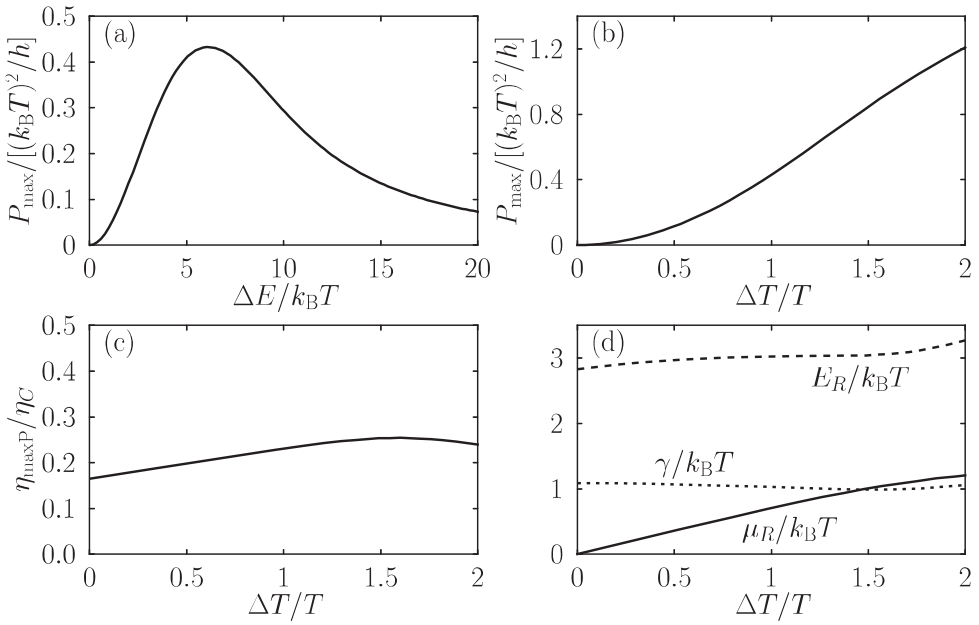

Fig. 3.2 (a) Scaled maximum power as a function of energy gain ΔE for $\Delta T = T$ and level width γ and μ_R optimized to give maximum power. (b) Scaled maximum power as a function of $\Delta T/T$ for optimized values of $E_R = \Delta E/2$, γ and μ_R. (c) Efficiency at maximum power for the values of $E_R = \Delta E/2$, γ and μ_R chosen to maximize power. (d) The optimized values are plotted versus $\Delta T/T$. Here $E_R = \Delta E/2$, $\mu_R = \mu/2$. This figure is adapted from Ref. [1].

average temperature defined as $T = (T_R + T_C)/2$, ΔT is the temperature difference defined as $\Delta T = T_C - T_R$. Figure 3.2 shows that if $\Delta E < k_B T$ the power increases as $(\Delta E)^2$, as indicated in Equation 3.9, but then levels off and decays exponentially, attaining its maximum around $\Delta E = 6k_B T$. Similarly, the choice $\gamma = k_B T$ gives optimal power. Here, ΔE and the level width are two essentially independent energy scales of this system. As a matter of fact the energy gain $\Delta E \approx k_B T$ is almost an order of magnitude larger than the level width $\gamma \approx k_B T$. These considerations suggest an experimental strategy for maximising the power of such a device: measure what the resonant level widths are, and tune the reservoir temperatures and energy gain to them.

Figure 3.2(b) shows that the efficiency at maximum power drops from half the Carnot efficiency to about $0.2\eta_C$ when the parameters are optimised. However, when γ is kept small, in the nonlinear regime the efficiency can exceed the bound $\eta_{maxP} \leq \eta_C/2$ found in the linear regime. This small drop in efficiency is more than compensated by the extra power it obtains. According to Figure 3.2, the power reaches a maximum of $P_{max} \sim 0.4(k_B \Delta T)^2/h$, or about 0.1 pW at $\Delta T = 1$ K. This jump in power can be attributed to the highly efficient conversion of thermal energy into electrical energy by optimising both the level width and energy-level difference [1].

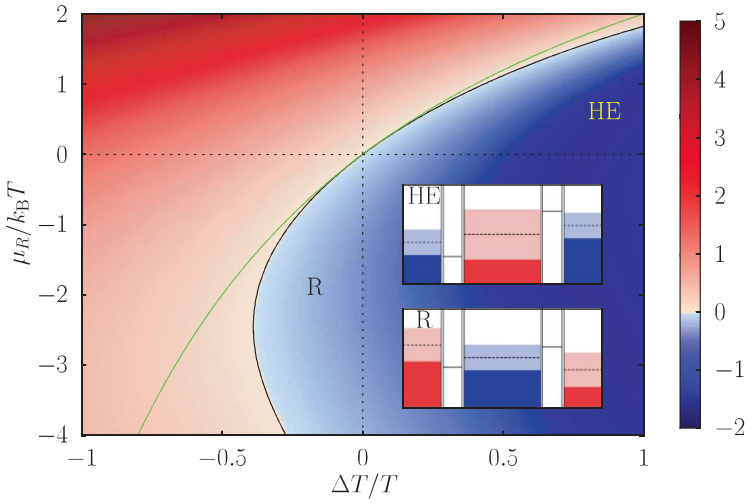

Fig. 3.3 Scaled heat current $J/[2(k_B T)^2/h]$ leaving (blue) or entering (red) the central cavity vs temperature difference (x axis) and applied bias (y axis) divided by average temperature. The plot is for system parameters optimized for maximal power output, an energy gain of $\Delta E \approx 6k_B T$ and level width $\gamma \approx k_B T$. The green line is the $J = 0$ curve for $\gamma \to 0$ while the black curve is the $J = 0$ line for the optimised γ. The system can work as a heat engine (HE) in the blue region for $\Delta T > 0$, $\mu_R = \mu/2 > 0$ (configuration shown in the inset labelled HE), or as a refrigerator (R) in the blue region for $\Delta T < 0$, $\mu_R = \mu/2 < 0$ (configuration shown in the inset labelled R). This figure is adapted from Ref. [1]

In Figure 3.3, the heat current J is plotted versus temperature difference and applied bias. It is found that when the system parameters are optimised to give maximum power, the system can be operated in the mode of a heat engine (HE) or a refrigerator (R). However, in contrast to the case where the levels are narrow compared to the other energy scales (and consequently the cavity can cool to arbitrarily low temperatures in principle; see solid green line, Equation 3.8), for this choice of parameters the cavity will only cool to the temperature where the $J = 0$ curve (solid black line) bends back.

3.2 Device Design

The designs for this QDEH device are based on a quantum-dot refrigerator (QDR) experimentally realised by Prance *et al.* [49], a dual role that such quantum dot devices can achieve. The QDEH device was demonstrated twice, with sample S31D5, shown as panels (a), (b) and (c) in Figure 3.4, and with sample S31D2, shown as panels (d), (e) and (f). The surface gates in Figure 3.4 define a cavity of $90\,\mu\text{m}^2$ area at the central 2DEG region, with two nominally identical quantum dots placed respectively on the left and the right sides of the cavity. Unlike

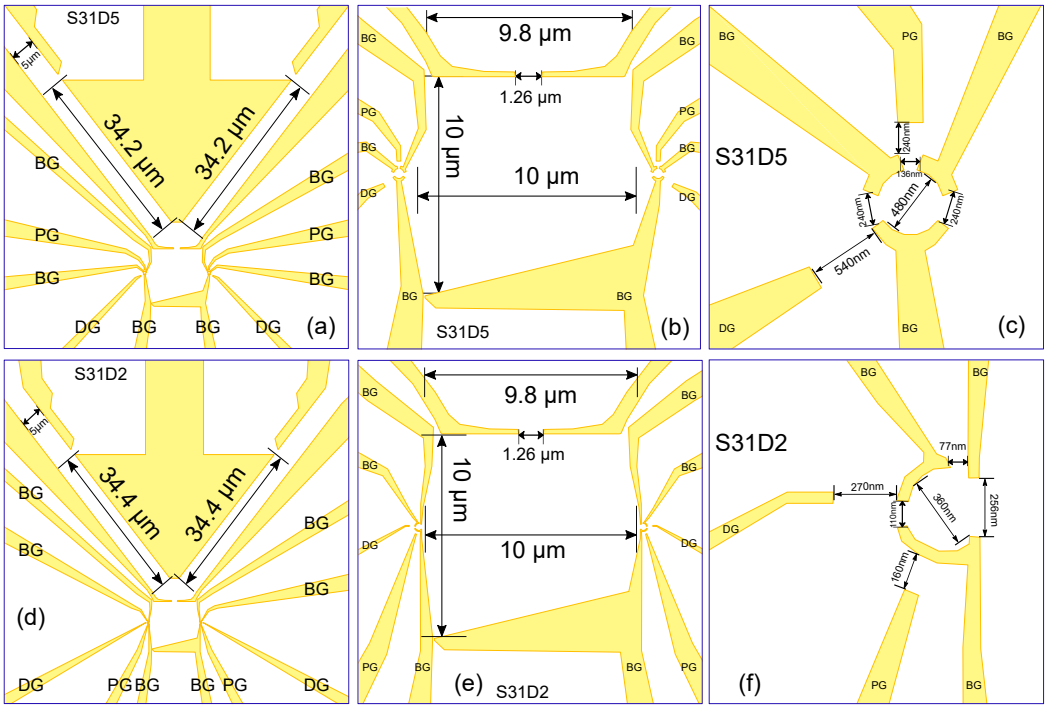

Fig. 3.4 Sample design: (a), (b) and (c) are successively magnified images of the design for sample S31D5. (d), (e) and (f) are successively magnified images of the design for sample S31D2. Here the gates are in yellow, and PG stands for the plunger gate, BG for the barrier gate, and DG for the detector gate.

in the QDR device of Prance, a heating channel of about 78 μm long is connected to the central cavity via a gap of 1.26 μm built in their shared barrier gates. This gap can allow hot electrons to traverse into the central cavity and keep the required temperature profile. The quantum dots, of diameter 480 nm for S31D5 and 360 nm for S31D2, as shown in 3.4(c), are constructed of three barrier gates (BG), one detector gate (DG), and one plunger gate (PG). The detector gate can serve to sense the charge states of the dots, which will be discussed in detail in Chapter 4 (Section 4.3).

3.2.1 The size of the central cavity

Following Prance's discussion [138], there are two factors to be considered while designing the cavity: (i) the discrete energy-level spectrum of the electron gas may be approximated as a continuum; (ii) the distribution of occupied states should be in quasi-equilibrium. The first consideration is for the average energy separation between states (ΔE_C). In a 2DEG of area A, this is given by the density of states: $g_{2D}(\varepsilon) = (m^*/\pi\hbar^2)$. Discounting the zero-energy separation between spin-degenerate states, the average energy separation is given by

$$\Delta E_C = (2\pi\hbar^2/m^*A). \tag{3.10}$$

For the spectrum of states to be approximately continuous, we require that ΔE_C is less than k_BT. At 50 mK, this implies $\Delta E_C < 4.3\,\mu$eV. This isolated electron gas must therefore have an area larger than 1.7 μm^2. The second consideration for the size of the central cavity area is that the distribution of its occupied states should ideally be in quasi-equilibrium, determined by a Fermi function, but at a non-equilibrium temperature. According to Prance's analysis [138], the area should be larger than 80 μm^2 for $T = 50$ mK, and larger than 3 μm^2 for $T_b = 300$ mK, to maintain the quasi-equilibrium in the isolated electron gas of the cavity [138].

Unlike the QDR device, the QDEH device requires a heat source from which it can harvest energy. This is achieved by putting a heating channel on the top of the cavity, with a gap of 1.26 μm, via which the electrons can traverse into the cavity. To avoid hot electrons injected from the heating channel being reflected right back into the heating channel, the bottom barrier gate of cavities is designed to be a slope with an angle of 26°. The cavity design for this QDEH device is shown in Figure 3.4. It has an area of 90 μm^2, and consists of seven barrier gates, shared with quantum dots and the heating channel.

3.2.2 The size of the heating channel

The heating channel is a resistor that heats the cavity through Joule heating with $P = I^2R$. For a typical dilution-refrigerator temperature, such as 100 mK, the 2DEG has a resistance of a few hundred ohms, which was mostly decided by the Ohmic contacts that connects the source and drain circuits [139]. For this heating channel with a width of 5 μm and a length of 78 μm, the resistance is measured to be around 500 ˙, which also indicates that no one-dimensional channel is formed there.

The a gap of 1.26 μm allows electrons to traverse into the cavity from the channel. For $T \sim 500$ mK, the heated electrons relax to the lattice temperature over a distance $l_{\text{e-ph}} \sim 200\,\mu$m, and as T is lowered further, $l_{\text{e-ph}}$ can significantly exceed the size of the cavity of the device [15]. In this regime, the energy redistribution is achieved via electron diffusion to the cold reservoirs [140]. Therefore, in this device, hot electrons diffuse out from the heating channel to the central cavity and replace cold electrons, serving to redistribute energy and leading to a well-defined electron-temperature profile.

3.2.3 The size of quantum dots

The only constraint on the design of the dots for a QDEH is that they have a significant energy separation between their states due to quantum confinement. Specifically, the state separation should be much greater than $k_B T_e$, where T_e is the electron temperature in the reservoirs. For a quantum dot with a radius a, one can approximate its corresponding maximum temperature through $T_e = \Delta E/k_B \approx E_F/(n_{2D}\pi a^2 k_B)$, where E_F is the Fermi energy of the 2DEG, n_{2D} is its carrier density, and a is the radius of the quantum dot. Therefore, we require a quantum dot to be as small as possible. However, the fact that the 2DEG used in this work is 110 nm below the surface of the heterostructure sets a lower limit on the smallest features that can be defined in the 2DEG using surface gates because of capacitive edge effects.

To find the ideal designs, the quantum dots are designed in different sizes and shapes with a radius larger than 110 nm, and Figure 3.5 shows designs of devices that have survived the fabrication process and have shown Coulomb blockade during experiments. For the two successful heat engine devices of S31D5 and S31D2, the maximum temperatures their quantum dot energy-level spacing corresponded to were 0.20 K and 0.36 K, respectively.

3.3 Fabrication

QDEH devices were fabricated using standard semiconductor processing techniques, with a mixture of optical and electron-beam lithography. Appendix A.1 contains the details

of the wafer used to make the devices, which was grown by the MBE team at the SP group of the Cavendish Laboratory. The mobility and carrier concentration of the 2DEG, which was 110 nm below the surface, were measured to be $\mu \approx 3.38 \times 10^6\,\mathrm{cm^2V^{-1}s^{-1}}$ and $n \approx 1.35 \times 10^{11}\,\mathrm{cm^{-2}}$ at 1.5 K. A set of pre-existing optical mask layers, named *J – Star* was used. First of all, a chip of area $10 \times 10\,\mathrm{mm^{-2}}$ is cleaved from a larger piece of wafer. Then it will go through a typical cleanroom process as below.

3.3.1 Mesa

An etch removes the 2DEG from the majority of the chip, leaving a central $200 \times 200\,\mu\mathrm{m}^2$ mesa in which to place a device, and 20 connecting legs.

1. The wafer was cleaned thoroughly in organic solvents: 6 minutes in acetone in an ultrasonic bath, followed by a 6 minute-long rinse in iso-propyl alcohol (IPA) to remove the acetone. The IPA was removed by blow-drying with dry N_2.

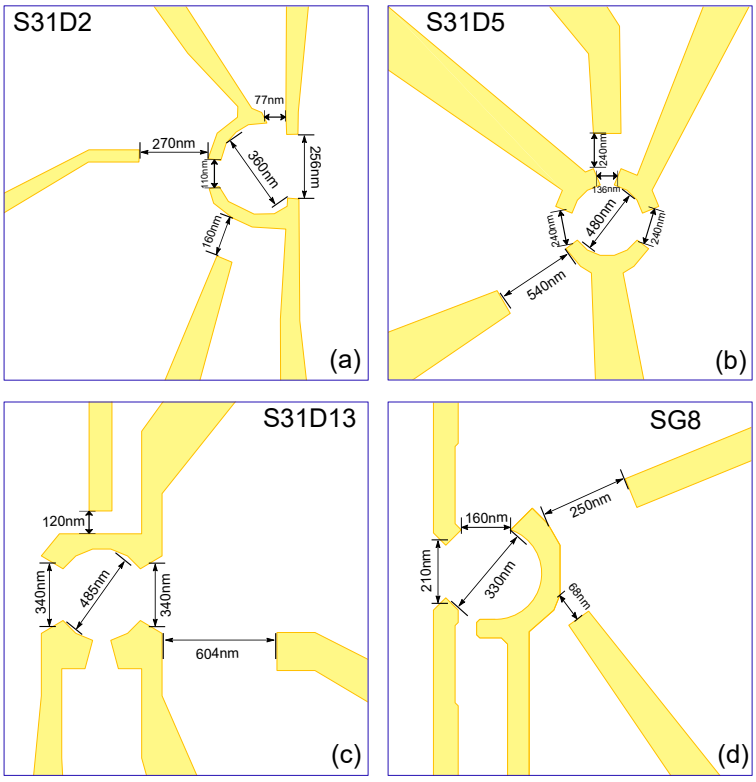

Fig. 3.5 The designs of quantum dots with different sizes and shapes, that has worked well in our measurements.

2. The photoresist, Shipley 1805, was spun onto the cleaned wafer at a rotation speed of 5500 rpm for 30 seconds. The solvent in the resist was then evaporated by baking it at a temperature of 115 °C for 60 seconds on a hotplate.

3. The phototresist was exposed to ultraviolet light for 3.5 seconds, while using the mesa pattern on the *J-Star* mask to block the light in some places.

4. The exposure to UV light breaks up the long polymer chains in the photoresist, so the exposed resist can then be removed by immersing the chip in MF319 developer for 60 seconds. The developer was then rinsed away using DI water, and the chip was dried thoroughly. This step is illustrated in Fig. 3.6(a).

5. The height of the photoresist was measured in a surface profiler (Dektak), to check that the thickness was uniform throughout. The exposed parts of the wafer were then etched away using a solution of H_2SO_4:H_2O_2:H_2O in the proportions 1:8:1600 for 3 minutes. The depth of the etch was measured in a surface profiler (Dektak), and found to be 120 nm. This ensures that all the unwanted areas of 2DEG, which is 110 nm below the surface, have been etched away. This step is illustrated in Fig. 3.6(b).

6. The photoresist was then stripped away by dissolving it in acetone, followed by a rinse in IPA, and a blow-dry with dry N_2. This step is illustrated in Fig. 3.6(c) and (d).

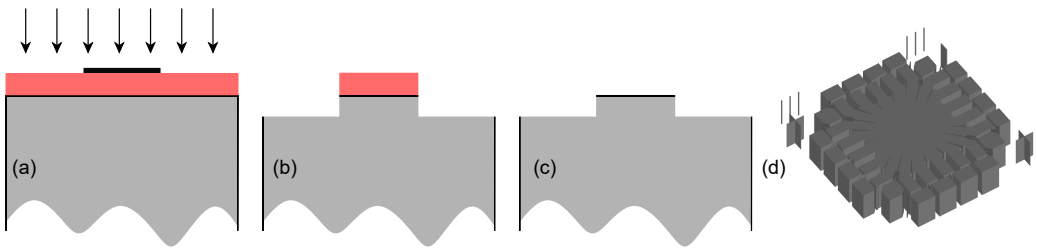

Fig. 3.6 (a), (b) and (c) The fabrication steps to form the isolation pattern (mesa). The pink layer stands for the photoresist Shipley 1805. (d) A 3D image of the completed mesa pattern, by AutoCAD.

3.3.2 Ohmic contacts

Annealed ohmic contacts are defined on bond pads at the end of each of the legs, aimed to connect the source and drain leads of the circuit. The contacts are patterned from evaporated AuGeNi, using a lift-off process. They are then annealed at 430 °C for 80s to contact the 2DEG.

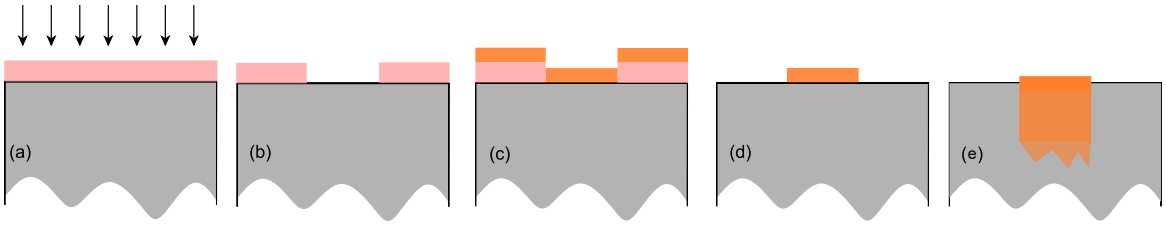

Fig. 3.7 The fabrication steps to form the source and drain ohmic contacts to the 2DEG. The pink layer is the photoresist Shipley 1813. The orange layer represents the AuGeNi.

1. Photoresist Shipley 1813 was spun onto wafer at a rotation speed of 5500 rpm for 30 seconds, and then baked at a temperature of 90 °C for 60 seconds. The baking temperature is lower than the one used in mesa processing, so as to obtain the exposed 'latent' image in the resist layer to align the contact features to the mesa ones.

2. The photoresist was exposed to ultraviolet light for 6.5 seconds, while using the pattern of the ohmic bond pads (accurately aligned with the etched mesa pattern) on the *J-Star* mask to filter the light. This step is illustrated in Fig. 3.7(a).

3. The exposed resist was then soaked in chlorobenzene for 3 minutes before being developed in MF 319 for 60 $\sim$ 120 seconds. The chlorobenzene firms up the top layer of the photoresist, so that the developer preferentially develops the photoresist closest to the wafer. This leads to a resist profile with an undercut, which helps in getting a cleaner metal lift-off (next step). This step is illustrated in Fig. 3.7(b).

4. Before metal deposition, the oxidised layer of GaAs on the surface of the chip is removed by soaking the chip in dilute hydrochloric acid ($HCl:H_2O$ in a ratio of 1:9) for 30 seconds. This removes any undeveloped resist ('scum') remaining on the exposed regions.

5. 300 mg of AuGeNi alloy was evaporated onto the chip, forming a layer of 82 nm. This step is illustrated in Fig. 3.7(c).

6. The photoresist protecting parts of the chip was removed by rinsing the chip in acetone for 10 minutes. This also removes the unwanted metal, so the process is called 'lift-off'. This step is illustrated in Fig. 3.7(d).

7. The chip was then heated to 430 °C in forming gas (a mixture of N_2 and H_2) for 80 seconds, so that the metal deposited on the ohmic bond pads diffuses into the wafer and contacts the 2DEG electrically. This step is illustrated in Fig. 3.7(e).

8. A small current was passed through a pair of ohmics by touching the surface with a pair of narrow probes, to verify that the 2DEG has been contacted. The average resistance for a pair of probes on opposite sides of the chip was found to be 7 k˙ at 77 K.

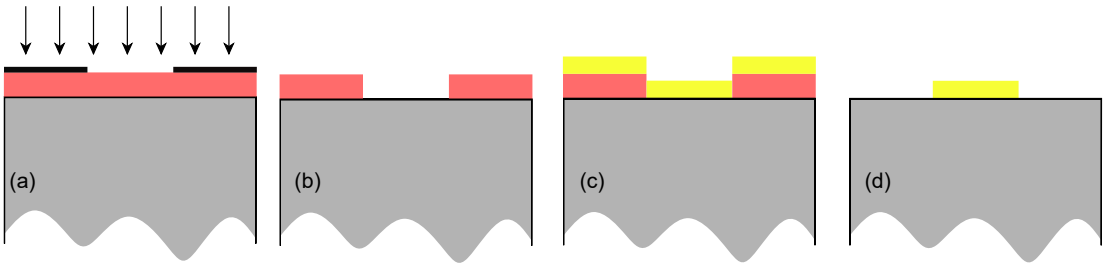

Fig. 3.8 The fabrication steps to form metal surface gates using optical lithography. The pink layer is the photoresist Shipley 1813. The yellow layer denotes the Ti/Au.

3.3.3 Optical gates

Metal gates with bond pads are evaporated on the surface of the chip. The gates rise up onto the central mesa where they can be extended by further lithography to form a device. The gates are patterned, again via lift-off, from evaporated Ti/Au of approximately 20nm/100nm thickness.

1. Photoresist Shipley 1813 was spun onto wafer at a rotation speed of 5500 rpm for 30 seconds, and then baked at a temperature of 90 °C for 60 seconds.

2. The photoresist was exposed to UV light for 6.5 seconds, while using the pattern of the gates (accurately aligned with the ohmic pattern) on the *J-Star* mask to block the light in some places. This step is illustrated in Fig. 3.8(a).

3. The photoresist was developed in MF319 for $40 \sim 60$ seconds. The result is illustrated in Fig. 3.8(b).

4. Before metal deposition, the oxidised layer of GaAs on the surface of the chip is removed by soaking the chip in dilute hydrochloric acid (HCl:H_2O in a ratio of 1:9) for 30 seconds. This removes any undeveloped resist ('scum') remaining on the exposed regions.

5. 20 nm of Ti was evaporated onto the chip, followed by 100 nm of Au. The Ti is a wetting layer, which helps the Au to stick to the GaAs surface. This step is illustrated in Fig. 3.8(c).

6. The unwanted metal covering the parts of the chip was removed by soaking the chip in acetone overnight. The result is illustrated in Fig. 3.8(d).

3.3.4 E-beam gates

To define the fine-feature surface gates, electron beam lithography is performed.

1. Two layers of PMMA were deposited on the wafer - the first had a molecular weight of 100 000 amu, and was diluted to 3% in anisole, and the second had a molecular weight of 950 000 amu, and was diluted to 2% in a combination of anisole and MIBK. Both the layers were spun on at 8000 rpm for 60 seconds, and were then baked at 115 °C for 2 minutes each. The resists were 100 nm thick, deposited as two 50 nm thick layers spun on top of the other. Higher-molecular-weight PMMA produces a higher contrast ratio for a given exposure dose and dissolves more slowly in the developer. This leads to a small overhang in the resist profile, which results in a good lift-off. The step is illustrated in Fig. 3.9(a).

2. The chip was exposed to a beam of electrons to trace out the pattern of sub-micron gates using the electron-beam lithography machine by a technician.

3. Since the PMMA layers on the chip are very thin, they were dissolved by dipping the chip in the solvent mixture MIBK:IPA:MEK (in the ratio 5:15:1) for just 8 seconds at ambient temperature. The result is illustrated in Fig. 3.9(b).

4. 10 nm of Ti followed by 30 nm of Au were evaporated onto the chip. The unwanted metal was removed by soaking the chip in acetone overnight. These are shown in Fig. 3.9(c) and (d).

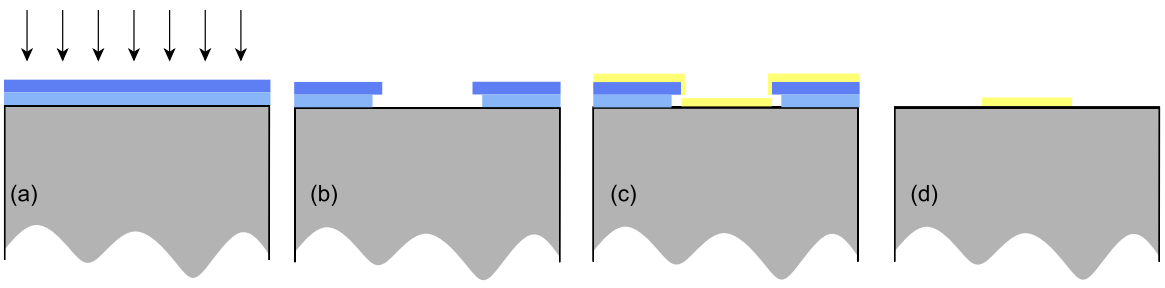

Fig. 3.9 The fabrication steps to form metal surface gates with E-beam lithography. The blue layers are the two layers of PMMA. The yellow layer is the Ti/Au.

3.3.5 Bonding

After all the processes above, a device is completed by being packaged in a 20-pin LCC sample holder.

1. The chip was cleaved into individual devices using a diamond-tipped scriber.

2. Each device was stuck onto a 20-pin LCC chip carrier using GE varnish.

3. The devices were serially bonded using a ball bonder, whilst taking care to protect the devices from the spark which forms each new ball at the tip of the bonder. This was done by the use of an ionised air-blower which neutralises any charge imbalances left on the gates while forming the bond, and also by physically separating the chip from the bonder-tip when it sparks (the bonder has to be used in the manual mode for this to be possible). Other precautions used were, waiting for one minute before forming a new bond so that charge imbalance on the tip has time to settle, and bonding gates and ohmics in pairs with the bond to the ohmic made after the bond to the gate so that charge build-up is shorted to each other before the first bond was made. This ensures that charge deposited on a gate flows to the 2DEG, thus minimising the risk of 'blowing-up' the gate as a result of electrostatic discharge. The wire bonds to the device are shown in Fig. 3.10(b).

Figure 3.10 shows SEM images of a typical completed device that has been packaged in a 20-pin LCC chip holder.

3.4 Measurement set-ups

All of the measurements presented in this chapter were made on device S31D5. The device was cooled in a ^{3}He/^{4}He dilution refrigerator with a base temperature of approximately 50 mK. The fridge is located in a screened room to reduce the coupling of environmental RF radiation to the experiment and the measurement electronics. Appendix B briefly explains the working of a dilution refrigerator.

Electrical connections to the device was made via twenty low-frequency lines. These run from a break-out box at room temperature into the vacuum space of the dilution fridge, and down to the sample holder. Before the sample holder, all twenty lines first pass through low-pass three-pole RC filters, which are installed to the mixing chamber of the fridge. These reduce noise in the measurement wiring, and the related increase of electron temperature in the device. The filters were designed to have a cut-off frequency of approximately 3 MHz.

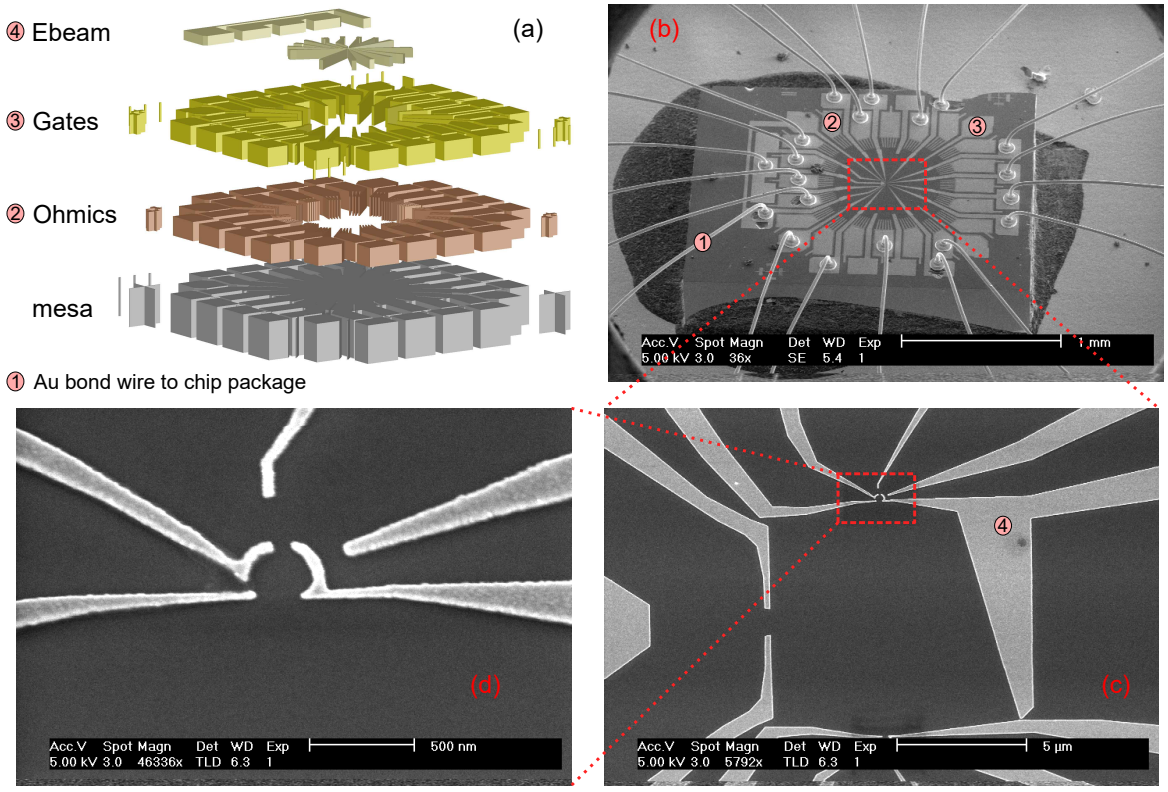

Fig. 3.10 Panel (a) depicts the layers of the mesa, ohmic contacts, optical gates and e-beam gates. (b)-(d) shows the sequentially smaller scale SEM image of a completed device.

In addition, the device was enclosed in a metal can, thermally anchored to the still to shield from the radiation from nearby 4 K surfaces.

A *NIDAQ-9178* was used to apply DC voltages on surface gates of the QDEH device. Every connection out of the *NIDAQ-9178* is made to first pass through a switch and a room temperature RCR filter consisting of two 1 MΩ resistors in series and a 0.1 μF capacitor to ground. The switches offer an option to turn off filters, and these filters provide protection to the fragile gates from sudden voltage spikes or large injections of charge. The *NIDAQ-9178* was also used to apply DC currents to the heating channel during measurements.

The transport properties of the device were studied by measuring differential conductance with a lock-in amplifier *SR7265*. The lockin produces an AC excitation voltage, and sends it to the output connector and simultaneously uses this signal, with some phase added, as a reference to the signal returning from the sample. The output signal is sent through a 1 : 1 transformer, to remove ground loops, and then reduced in magnitude via a voltage divider. The voltage is dropped across the sample and the current is produced, which is dependent on the conductivity of the sample, and then enters a current-to-voltage pre-amplifier. The signal from the pre-amplifier is sent back to the lockin for measurement. The excitation frequency

should not be a multiple of the frequency of the electrical noise in the environment which is usually 50 Hz from the mains. In these experiments an excitation voltage of 0.1 V at 77 Hz is used; this is divided by 10^4 via the potential divider to produce 0.1 μV across the device. The pre-amplifier used in this work has a gain factor adjustable between 10^6 and 10^7 A/V. To measure non-linear transport, a constant bias voltage, V_{SD}, could also be applied across the device. The bias voltage V_{SD} was applied through the pre-amplifier in our measurement. Details of the two different measurement setups are given in Figure 3.11 and Figure 3.14 (c).

Two *SR7265* lock-in amplifiers are used together for thermal power measurements. One lock-in amplifier is used to apply an AC heating current into the channel at a frequency of f, while another lock-in amplifier is used to measure the thermal voltage difference across the cavity via the $A-B$ mode at a frequency of $2f$. For QDEH devices, since the heating power varies as I^2, the electron temperature in the cavity oscillates at twice the frequency of the current I_{Heat}. Thus it was necessary to phase lock to the $2f$ component of V_{th} [15]. A pre-amplifier with a gain of 10^3 is used before the signal goes back to the lock-in amplifier.

3.5 Measurement results and analysis

The first measurements performed on the device were to characterise separately two quantum dots, the heating channel and the central cavity. The aim of these measurements was to confirm that the two quantum dots both have been formed; that the central cavity has good connection with the heating channel; that the heating channel is providing enough heat.

3.5.1 Tuning quantum dots

Figure 3.11 shows a false-colour SEM (scanning electron micrograph) image of a measured device (S31D5), along with the electrical circuit used to tune the device. Each quantum dot in the device was set up using three barrier gates, coloured in blue in Fig. 3.11, a plunger gate (coloured blue) that was used to change the chemical potential of the quantum dot, and a detector gate (coloured green). To find the voltages required on these gates to form a particular dot, the differential conductance of the device was measured while stepping voltages on related barrier gates and sweeping the voltages on the appropriate plunger gate. We know a quantum dot is formed when Coulomb oscillations can be observed from the differential conductance measured by the lock-in amplifier. Figure 3.12 shows the expected signature of Coulomb blockade of each dot: periodic peaks in conductance, separated by regions of zero conductance.

The formation of quantum dots can be confirmed by measuring the conductance over a range of bias voltage, V_{bias}. Such measurements will show the Coulomb diamonds discussed in Section 2.2.3. This measurement is performed with the same circuit in Figure 3.12 while applying a DC bias voltage across the device via the current to voltage pre-amplifier. Figure 2.5 shows finite-bias measurements made on each of the two dots. They all show the zero-bias conductance peaks evolving as expected for Coulomb blockade: the peaks split linearly with bias, revealing structure due to the dot's spectrum of states within the resulting triangles. It is noted that the zero-bias points of both Coulomb diamonds are actually around $V = 0.1\,\mathrm{mV}$. This corresponds to the offset voltage of the pre-amplifier.

In Figure 2.5, the blue lines follow the edges of the Coulomb diamonds, fitted by eye. Their gradients can be used to find the conversion ratio between the plunger-gate voltage, and dot energy. For the left and right dots, these 'lever-arms' are found to be $\alpha_{LD} = 0.025\,\mathrm{eV/V}$, $\alpha_{RD} = 0.015\,\mathrm{eV/V}$ respectively. One of the requirements for realising an efficient QDEH is that the quantum dots have large energy separation between their single-particle states, compared to $k_B T$. This can be extracted by the energy spacing of the excited states of Coulomb diamonds. In Figure 3.13, the cyan lines follow edges of the excited state, fitted

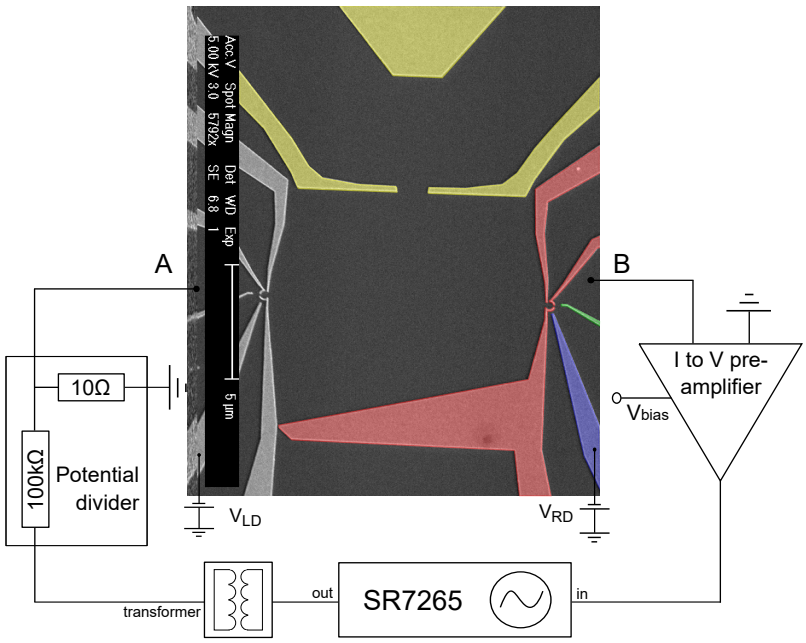

Fig. 3.11 The electrical circuits used for the Coulomb Diamond measurements. A DC voltage is applied to the pre-amplifier, that converts currents to voltages before sending the signals back to the lock-in amplifier, and the differential conductance is measured using the lock-in SR7265. A transformer is used to decrease the noise in the circuit. The potential divider is set before the trigger voltage sent to the sample, in order to decrease the voltage.

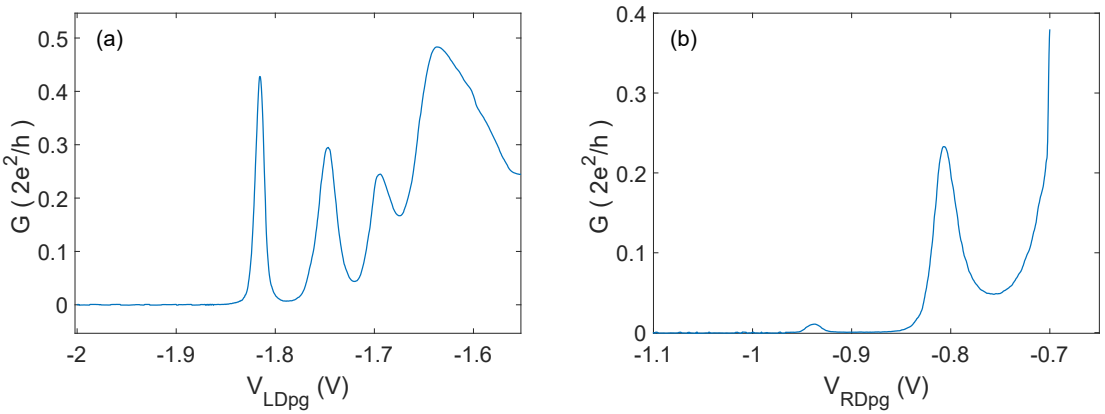

Fig. 3.12 Typical signature of Coulomb blockade. Panel (a) shows the Coulomb peaks of the left dot, and panel (b) of the right dot, both measured at a temperature of 50 mK. The different width and height of the last Coulomb peaks of both dots indicate that the left and the right quantum dots are tuned to have different barriers. Therefore they are not symmetric.

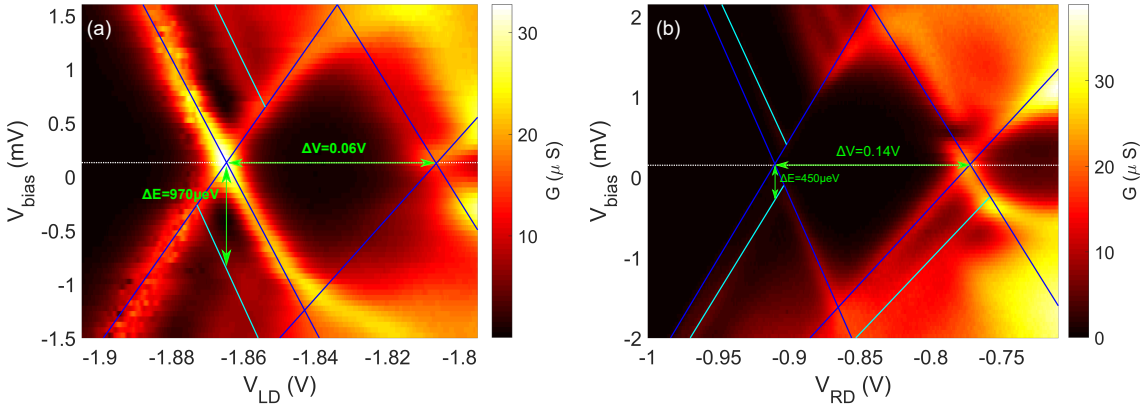

Fig. 3.13 Finite-bias conductance measurements of the left quantum dot (panel (a)) and the right dot (panel (b)). The blue lines are linear fits (by eye) to the blockade diamond edges. The cyan lines are linear fits (by eye) to the excited states, parallel to the diamond edges. The horizontal arrows indicate the blockade diamond widths, ΔV. The vertical arrows indicate the energy spacing of the first excited states, ΔE.

by eye. It can be seen that the excited state is at least 450 μeV above the ground state. Such a separation should, in principle, be sufficient for the QDEH to operate up to temperatures around 4 K. From this and other similar measurements, it was clear that the dots were able to achieve the large state separations required.

After investigating the differential conductance and Coulomb diamonds, the voltages of the barriers are chosen. The barrier-gate voltages chosen for the left dot are $V_{LB1} = -0.606V$, $V_{LB2} = -0.330V$ and $V_{LB3} = -0.392V$; the barrier-gate voltages chosen for the right dot are

$V_{RB1} = -0.890V$, $V_{RB2} = -0.430V$ and $V_{RB3} = -0.435V$. It is important to note that these two quantum dots, in Figure 3.12 and Figure 3.13, do not show perfect sysmmetry, as assumed in the theoretical proposal (in Section 3.1). Therefore, some adjustments are required to compare experimental results with the theoretical predictions.

3.5.2 Thermal power measurement results

Figure 3.14 depicts the circuits used to measure the thermal voltage V_{th} and the generated thermal power P_{th} of this QDEH device. After setting up the quantum dots, the heating channel and the cavity of the device, an AC current I_{Heat} at frequency $f = 33\,\text{Hz}$ was applied to the heating channel using a lock-in amplifier, and the thermal voltage V_{th} was measured across A - B, with another amplifier locking in at frequency $2f$, whilst stepping the voltage

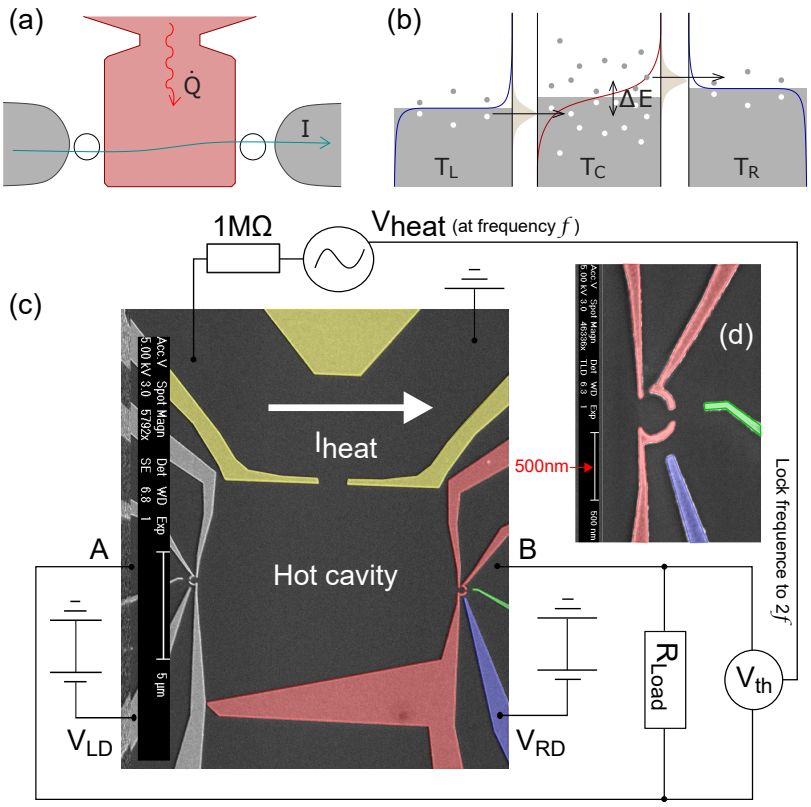

Fig. 3.14 (a) Two quantum dots connect two electronic leads (at temperature $T_0 = T_L = T_R$) to a hot cavity at T_C. A heat current $\dot{Q}$ is absorbed by the flowing electrons to generate a current I. (b) Relative energy diagram of the heat engine. Tuning the resonant level position filters tunnelling transitions with an energy gain ΔE. Panel (c) is the SEM image of the device with the electrical circuit used for the thermopower measurement. Panel (d) shows the zoomed-in image of the quantum dot.

V_{LD} on the left-dot plunger gate and sweeping the voltage V_{RD} on the right-dot plunger gate through their respective Coulomb resonances. Different AC currents are applied in the heating channel to have different temperature profiles in the central cavity. The temperatures can be extracted by fitting the differential conductance through the quantum dots, which will be discussed in detail in the next chapter. The cold reservoirs, which we assume to be at base temperature T_0, are connected externally by a load resistor, R_{Load}. The thermal power is then extracted by $P_{\mathrm{th}} = V_{\mathrm{th}}^2/R_{\mathrm{Load}}$. In potential applications the heating channel would be replaced by the heat source we wish to harvest energy from and R_{Load} represents an external device where useful work is done [1].

Figure 3.15(a) shows the thermal voltage between A and B (Fig.3.14(c)), V_{th}, measured with a heating current $I_{\mathrm{Heat}} = 100\,\mathrm{nA}$ and a load resistor $R_{\mathrm{Load}} = 500\,\mathrm{k}^{\cdot}$ in the circuit. The negative thermal voltage appears at $V_{\mathrm{LD}} \approx -1.924\,\mathrm{V}$ for the left dot, as shown in Fig. 3.15(c), and $V_{\mathrm{RD}} \approx -0.805\,\mathrm{V}$ for the right dot, as in Fig. 3.15(b). Figure 3.15(d) is the thermal power

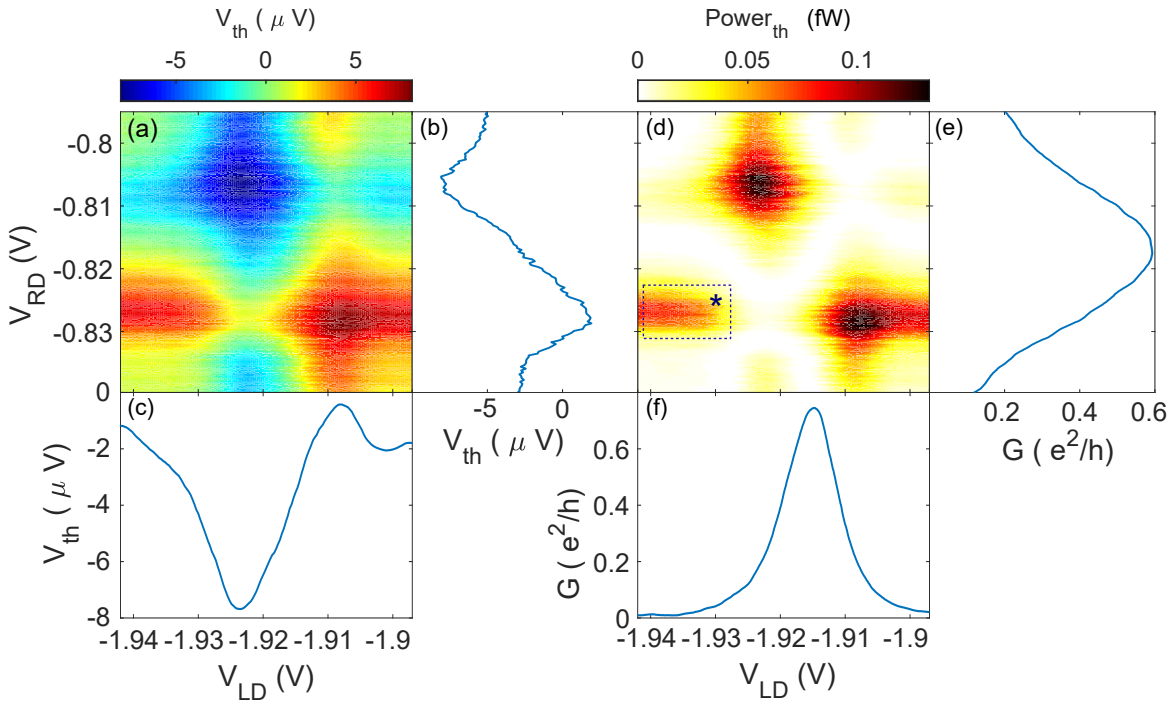

Fig. 3.15 (a) The thermal voltage V_{th}, across the device, as a function of left and right plunger gates measured whilst an AC current, $I_{\mathrm{heat}} = 100\,\mathrm{nA}$, is applied to the heating channel. The applied I_{heat} results in an estimated temperature difference of $\Delta T = T_C - T_L \approx 47\,\mathrm{mK}$ across the dots. (b) and (c) line graphs through (a) at $V_{\mathrm{LD}} = -1.924\,\mathrm{V}$ and $V_{\mathrm{RD}} = -0.805\,\mathrm{V}$ respectively. (d) Estimated power output of the device showing the two expected operating points and a third (highlighted by the box with a mark star $*$) due to external circuit impedance. The power is given by $P_{\mathrm{th}} = V_{\mathrm{th}}^2/R_{\mathrm{Load}}$ where R_{Load} is the resistance loading on the circuit. (e, f) Conductance peaks of the two dots as a function of the respective gate voltage.

extracted from the thermal voltage of Fig.3.15(a), through $P_{\text{th}} = V_{\text{th}}^2/R_{\text{Load}}$. The maximum thermal power is found at (–1.924, –0.805) V, followed by the second largest thermal power point at (–1.907, –0.829) V, in Fig. 3.15(d). The maxima appear in the vicinity of the electrical conductance peaks as shown in Fig. 3.15(e) and Fig. 3.15(f) respectively. This is because when both charge and heat are exclusively carried by electrons, for both diffusive and ballistic transport, the Seebeck coefficient S is related to the energy derivative of the conductance G [116],

$$S = \frac{V_{th}}{T_C - T_0}\bigg|_{\text{I=0}} = -\frac{\pi^2 k_B^2}{3e}(T_C + T_0)\frac{\partial \ln G}{\partial \mu}. \tag{3.11}$$

Here T_C is the electron temperature of the cavity, T_0 is the temperature of cold reservoirs, and μ is the chemical potential of the contacts. Meanwhile, the thermal voltage V_{th} peaks in Fig. 3.15(a) are also related to the energy derivative of the differential conductance G of the Fig. 3.15(e) and (f), as shown Eq. (3.11). Some thermopower is detected while only one dot is open on resonance, such as the area marked by the star $\star$ in Fig. 3.15(d). This arises from the influence of the external circuit impedance.

Thermopower measurements were carried out using resistance values (R_{Load}) from 50 k$\cdot$ to 3.9 M$\cdot$ in the circuit, whilst an AC current of 60 nA, 80 nA and 100 nA is applied on the heating channel. The heating currents of 60 nA, 80 nA and 100 nA correspond to 122 mK, 130 mK and 140 mK respectively, which will be discussed in detail in Chapter 4 (section 4.1). Figure 3.16 depicts the maximal generated power for each measurement as a function of the load resistance and the relative thermal voltages respectively. For increasing resistance R_{Load}, the power increases, reaches a maximum and then drops down, as shown in Fig. 3.16 (a). As the heating current in the channel is increased, the power also rises. This is because the cavity temperature increases with the heating current, resulting in more electrons tunnelling through the two dots and converting more energy to electrical current efficiently, as predicted in the theoretical proposal [1]. Interestingly, the maximum power always appears around $R_{\text{Load}} \approx 500\,\text{k}\cdot$ for all heating currents, corresponding to impedance matching between the heat engine and the resistor. The power vs. thermal voltage in Fig. 3.16 (b) gives an estimation of the open-circuit stall voltage of our device in each configuration. The asymmetric curves suggest the presence of non-linear effects.

3.5.3 Efficiency estimation

We next turn to the efficiency of heat-to-work conversion which is defined as the ratio of the generated electrical power P_{th} to the heat current from the hot reservoir $\dot{Q}$. The heat current is given by $\dot{Q} = \kappa\Delta T = \kappa(T_{\text{C}} - T_0)$ where the thermal conductance κ can be estimated from the electrical conductance G via the Wiedemann-Franz law, $\kappa = GL\overline{T}$, where

L is the Lorenz number, $\overline{T} = (T_C + T_0)/2$ and G is the combination of the conductance at $V_{RD} = -0.805\,V$ in Fig. 3.15(e) and that at $V_{LD} = -1.924\,V$ in Fig. 3.15(f). We remark that, as discussed in Section 2.6.4 in Chapter 2, the Wiedemann-Franz law in general is violated for mesoscopic conductors with strongly energy-dependent transmission peaks such as quantum dots [131, 133, 136, 141]. As the thermal conductance cannot be measured directly in our setup, we still use it to obtain a lower bound on the thermoelectric efficiency given by

$$\eta_{\text{w-f}} = \frac{V_{th}^2}{\kappa \Delta T R_{\text{Load}}} = \frac{V_{th}^2}{GL\overline{T}\Delta T R_{\text{Load}}}, \tag{3.12}$$

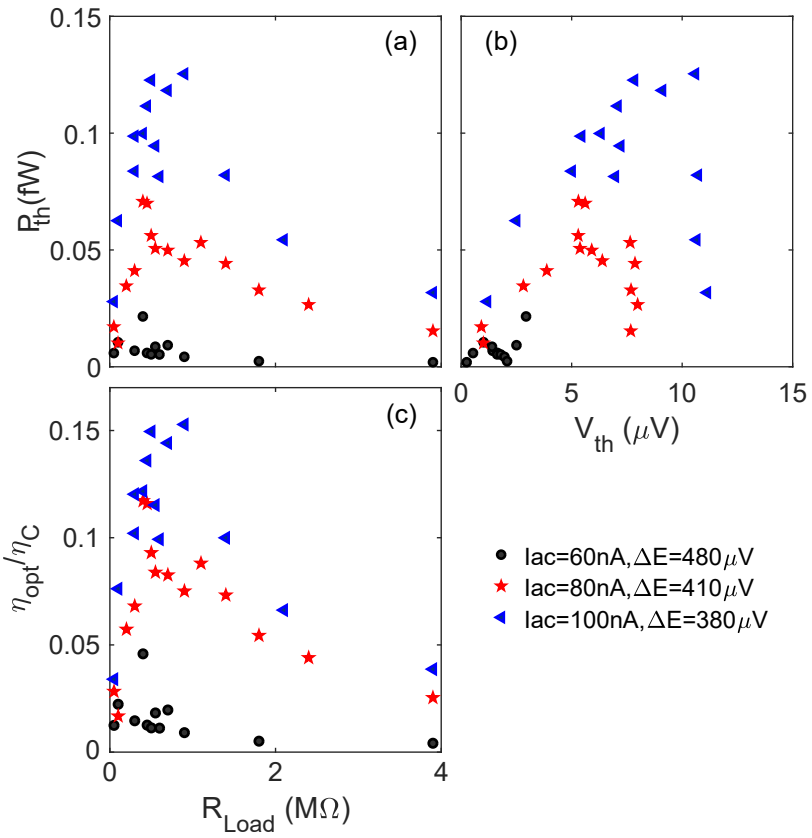

Fig. 3.16 Heat-engine characteristics. Panel (a) depicts the maximum thermal power from the measurements with different load resistance, whilst applying AC current 60 nA, 80 nA and 100 nA on the heating channel. Panel (b) shows the thermal power P_{th} and its relative thermal voltage V_{th}, which is also the bias voltage on the channel. Panel (c) depicts the ratio of the estimated optimal efficiency through Eq. (3.12) with the Carnot efficiency while changing the resistance R_{Load}. The data in the lower right corner shows the relative temperatures and energ-level difference ΔE of two dots at maximum power, with different AC currents on the heating channel. T_e is the electrical temperature of the cavity.

which can be compared with the theoretical efficiency calculated below. Figure 3.15(c) depicts the ratio of the estimated efficiency from Equation (3.12) to the Carnot efficiency ($\eta_C = 1 - T_0/T_C$) for 60 nA, 80 nA and 100 nA on the heating channel respectively.

3.5.4 Additional Theoretical Modelling

The experimental data in Fig. 3.15 and Fig. 3.16 is reproduced by the model of Ref. [1] which my collaborators, Dr. R. Sánchez, Dr. A. N. Jordan and Dr. B. Sothmann, generalise to incorporate the effects of the external circuit. The thermoelectric transport through each dot can be described by the Landauer-Büttiker formalism, with the expression:

$$\mathscr{I}_{l,n} = \frac{2}{h}\int dE E^n \mathscr{T}_l(E)[f_l(E) - f_C(E)], \tag{3.13}$$

giving the charge $I_l = e\mathscr{I}_{l,0}$ and energy $J_l = \mathscr{I}_{l,1}$ currents at lead l=L,R. The quantum-dot resonances are defined by a transmission coefficient

$$\mathscr{T}_l(E) = A_l \frac{\Gamma_l^2/4}{(E-\varepsilon_l)^2 + \Gamma_l^2/4}, \tag{3.14}$$

where the parameter A_l depends on the asymmetry of the quantum-dot barriers [137]. The quantum-dot resonance energies are tuned with gate voltages, $\varepsilon_l = \varepsilon_{l,0} - e\alpha_l V_{gl}$. In our

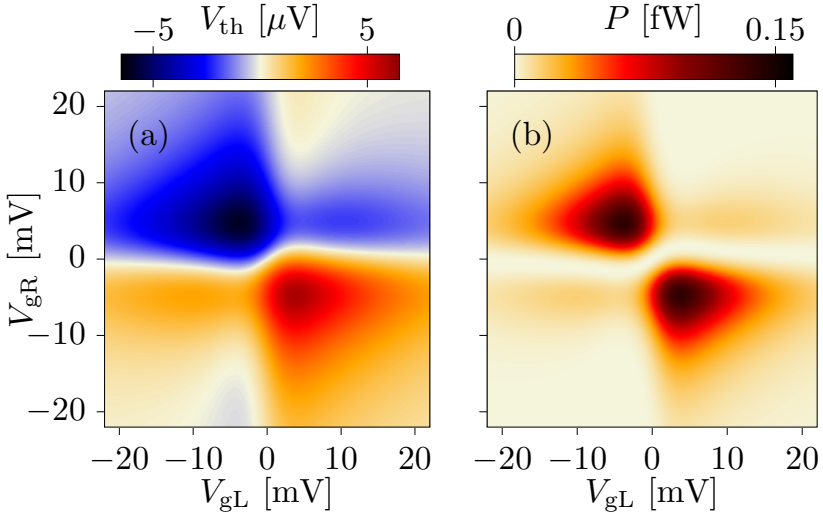

Fig. 3.17 Theoretical calculation of (a) the thermovoltage and (b) the generated power with parameters of $A_{\rm L} = A_{\rm R} = 1, \Gamma_{\rm L} = 0.2\,$meV, $\Gamma_{\rm R} = 0.1\,$meV, $\alpha_{\rm L} = 0.026$ and $\alpha_{\rm R} = 0.014$, the base temperature of $T_0 = 85\,$mK and the cavity temperature of $T_{\rm C} = 170\,$mK. The influence of the external load resistance is taken into account.

experiment, the width Γ_l is thermally broadened beyond the natural line width of the level. As no charge is injected from the heating channel into the conductor, the conservation laws for charge and energy read:

$$I_L + I_R = 0, \qquad J_L + J_R + \dot{Q} = 0, \tag{3.15}$$

where $\dot{Q}$ is the heat current injected into the central cavity. For a closed circuit where the energy harvester powers an impedance R_{Load}, the voltages are set via Ohm's law, producing the thermovoltage, $V_{\mathrm{th}} = I_L R_{\mathrm{Load}}$ and power of Fig. 3.17. Accounting for the external resistance in the circuit gives rise to additional features not present in an open-circuit model [1], such as the vertical and horizontal lines in Fig. 3.17. Our simple model based on resonant tunnelling captures all the features of the experiment, seen by the comparison of Fig. 3.16 and Fig. 3.18. The efficiency in Fig. 3.18(c) is computed with the general expression

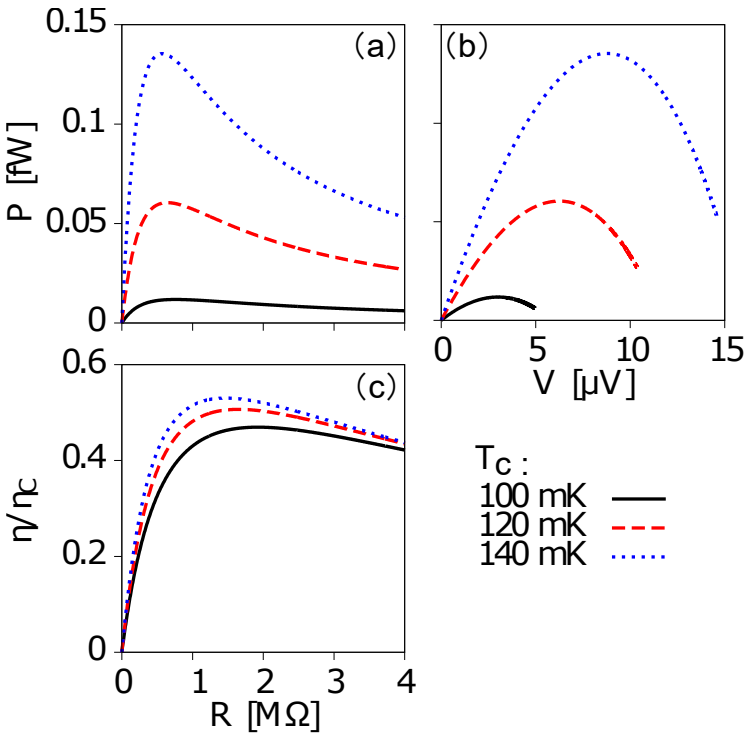

Fig. 3.18 Theoretical modelling. (a),(b) correspond to (a),(b) in Fig.3.16 respectively. Black, red and blue lines correspond to the cavity temperature T_C of 100 mK, 120 mK and 140 mK estimated for the cases with different heating current on the channel, 60 nA, 80 nA and 100 nA shown in Fig. 3.16, respectively. The base temperature in the model is 85 mK. The efficiency in (c) is computed from the charge and heat currents with resonances of $\Gamma_L = \Gamma_R = 3.5\,\mu$eV and the energy-level difference of $\Delta E = 45\,\mu$eV of the two dots. Parameter $A = 0.8$ is related to the quantum-dot barriers.

of the heat current evaluated at the obtained thermovoltage, $\eta = V_{\mathrm{th}}^2/(\dot{Q}R_{\mathrm{Load}})$. Figure 3.18 (c) suggests the maximum theoretical efficiency of the device is $\sim 0.5\eta_C$, for the considered parameters.

3.6 Conclusion

In conclusion, we have experimentally realized an energy harvester based on resonant-tunnelling quantum dots [1] which can generate a power of 0.13 fW with an estimated efficiency of at least $0.1\,\eta_{\mathrm{C}}$. Our theoretical model (not affected by limitations of the Wiedemann-Franz law) suggests the actual efficiency to be about $0.5\,\eta_{\mathrm{C}}$. Experimental observations of thermal power, voltage and efficiency at different values of I_{Heat} and R_{Load} have also been reproduced by this model. There are small quantitative differences between experimental results and theoretical modelling in terms of parameters, such as electrical temperatures and energy-level difference. This may be explained by asymmetric barriers, accidental degeneracies or the broadened lifetime width of the quantum dots, as well as charging effects in the non-linear regime. Also, the oscillation brought with the AC heating and AC measurements can increase thermal broadening in the cavity, and therefore cause inaccuracies in the measurements. Overall, this proof-of-principle experiment demonstrates the basic soundness of the theory of mesoscopic energy harvesting with energy-filtering techniques at the quantum level, realising a heat engine.

There are three ways to improve such a device. First, we can improve the power and efficiency by optimising the resonance width Γ_l as well as the symmetry of the quantum dots. Second, DC heating and measurement techniques can be used to avoid unnecessary oscillations of voltages and temperatures in the device. Finally, the performance of the energy harvester may be enhanced by scaling it up in size with resonant-tunnelling quantum wells, which may increase the maximum power up to fractions of W/cm^2 at 300 K [2], or by using smaller dots or molecules, whose large level spacing allows the system to operate at higher temperatures [1, 142, 143].

Chapter 4

A Quantum-dot thermometer

In the previous chapter, we discussed the experimental realisation of a Quantum Dot Energy Harvester (QDEH), including device designs, fabrication, measurements and analyis. Another important task is to extract electron temperatures of different regions of such a QDEH device. Accurate electron thermometry is needed in many aspects of low-dimensional semiconductor physics, particularly given the increasing important of hot-electron effects as mesoscopic device dimensions are reduced and electron mobility increases. Surplus heat energy in a 2DEG is rapidly shared among the carriers through electron-electron interactions, and an effective electron temperature T_e is established which may be considerably higher than the crystal lattice temperature T_l, to which both external thermometry and refrigeration are coupled. A measurement of the electron temperature is therefore needed to determine how an electron gas thermalises with its surroundings. Measurements of the thermoelectric response and thermal conductivity of mesoscopic devices are also interesting in their own right, as they provide fundamental information about electronic properties which is not available from electrical transport measurements alone [116].

This chapter will discuss how to extract the electron temperatures through three approaches. The first approach is to extract the electron temperature via fitting the Coulomb peaks through a quantum dots with theoretical models [67, 70]. The second is to monitor the charge occupation of a weakly tunnel-coupled 'thermometer' quantum dot using a quantum-point-contact detector gate [144]. The final one is to fit the thermal power peaks with theoretical models [116].

4.1 Coulomb Peaks

4.1.1 Theory

As discussed in Section 2.2.2 at Chapter 2, if the source-drain bias is very small, the difference between the Fermi functions in the equation 2.21 can be expanded to lowest order in a Taylor series about the Fermi level at equilibrium μ. Putting $\mu_D = \mu + eV_{SD}/2$ and $\mu_S = \mu - eV_{SD}/2$, we obtain the conductance of the quantum dot:

$$G = \frac{I}{V_{SD}} = \frac{2e^2}{h}\int_{U_S}^{\infty}(-\frac{\partial f(E,\mu)}{\partial E})T(E)dE.$$

If the two barriers are sufficiently opaque, the thermal spread of Fermi occupation function of the leads is much larger than the width of the transmission resonance of the dot ($\Gamma \ll k_B T_e$), and the conductance through the quantum dot becomes [58]

$$G = G_{max} \cdot \cosh^{-2}(\frac{\mu_{dot} - \mu}{2k_B T_e}), \tag{4.1}$$

where μ_{dot} is the chemical potential of the quantum dot, and μ is the chemical potential, that can be extracted from the plunger-gate voltage via its lever arm. The Lorentzian line shape of conductance provides a new way to look at the temperature dependence of G. The Full-Width at Half-Maximum of the resonance, FWHM $= 2\ln(3+2\sqrt{2})k_B T$ (calculated from applying $G = G_{max}/2$ into Equ. 4.1), can be used to detect change the electronic temperature. This is because the conductance at the minima results from the exponential tails of $\partial f/\partial E$, and hence appears activated, $\ln G \propto T^{-1}$, over some range [58]. The amplitude of the resonance can also be used as an electronic temperature detector. In the Coulomb-blockade regime, where $k_B T \ll \Delta E < e^2/C$, the peak height G_{max} is given by [67],

$$G_{max} = \frac{e^2}{4kT}\frac{\Gamma^l \Gamma^r}{\Gamma^l + \Gamma^r}, \text{ if } \hbar\Gamma \ll kT \ll \Delta E, \tag{4.2}$$

where Γ^l and Γ^r are tunnelling rates of the left and the right barriers respectively. The peak heights increase monotonically as $k_B T/\Delta E \to 0$, as long as $k_B T$ is greater than the resonance width $\hbar\Gamma = \hbar(\Gamma^l + \Gamma^r)$ [67]. Thus, both the height and the width of a Coulomb oscillation of a sufficiently isolated quantum dot can therefore be used to detect changes in temperature — the width being directly, and the height inversely, proportional to temperature.

Foxman *et al.* measured and studied the conductance of a quantum dot with a very small bias [145], as shown in Figure 4.1. It can be considered as a one-dimensional resonant-tunnelling system with many resonant levels whose energy can be moved through the Fermi

level by the gate voltage V_g. (In fact the energy levels are dominated by the electrostatic energy required to add extra electrons to the dot, a regime called the Coulomb blockade, as discussed in Section 2.2.1.) For a low V_g conductance peak, the coupling to the island is still relatively small and hence so too is its intrinsic width. This peak is fit well with the line shape of a purely thermally broadened resonance [58] in the limit that the resonance width is much less than k_BT,

$$G = \frac{e^2}{h}\frac{1}{4k_BT_C}A\cosh^{-2}\left(\frac{e\alpha V_g - E_{res}}{2k_BT_C}\right), \tag{4.3}$$

where E_{res} is the energy of the transmission resonance and A is the temperature-independent energy-integrated strength of the resonance, decided by the tunnel rates of both barriers. The

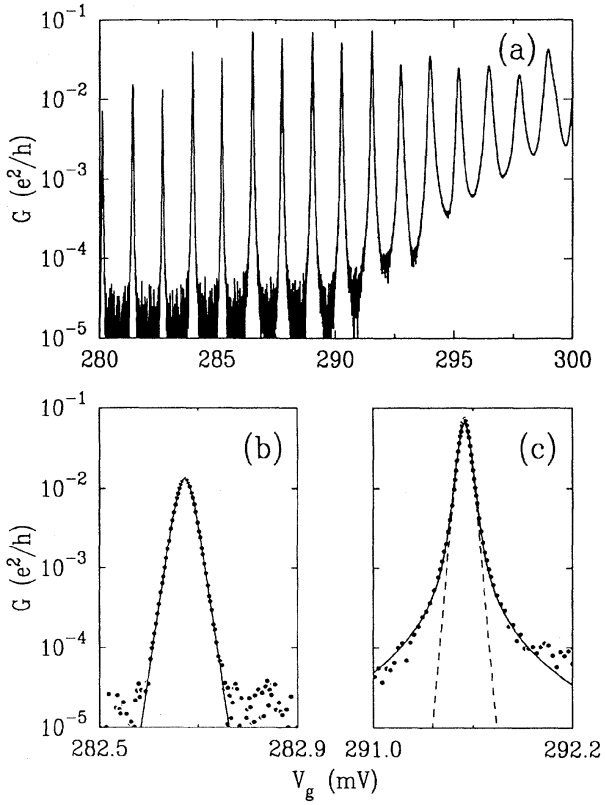

Fig. 4.1 (a) The low-bias conductance of the island vs V_g at $B = 2.53T$. (b) A low V_g conductance peak from (a) shown fit to a thermally broadened resonance (solid line) in the limit that the intrinsic resonance width is much less than k_BT. (c) A conductance peak at higher V_g shown fit to a thermally broadened Lorentzian (solid line). The dashed line is the best fit using the same line shape as in (b). This figure is adapted from Ref [145].

factor α, in Eq.(4.3), is the lever arm of the quantum dot. It relates a change in V_g to a shift in the energy of the island; $\alpha = U/e\Delta V_g$ where ΔV_g is the spacing between peaks. An example is provided by the peak around $V_g = 282.7\,\mathrm{mV}$, which can be fitted by a Lorentzian function. The peaks at lower voltage are in the opposite limit where the width of the Fermi function is larger and the shape of $G(V_g)$ is due to $\partial f/\partial E$ as shown in Fig. 4.1(b).

For a peak at higher V_g, at which the island is more strongly coupled to its leads. A striking feature of this peak is that its tails do not fall off exponentially. The line shape cannot be fitted by the expression in Eq.(4.3), when the intrinsic line shape of the resonance is influencing the conductance peak profile. Then, the peak can be fitted to a thermally broadened Lorentzian parametrized by a full-width at half-maximum Γ,

$$G = \frac{e^2}{h}\frac{1}{4k_BT_C}B\int_{-\infty}^{+\infty}\cosh^{-2}\left(\frac{E}{2k_BT_C}\right)\times\frac{(\Gamma/2)\pi}{(\Gamma/2)^2+[(e\alpha V_g - E_{res})-E]^2}dE, \tag{4.4}$$

which describes resonant tunnelling in non-interacting systems. In actual measurements, conductance peaks often exhibit asymmetries and other features which underscore the limitations of broadly applying the Lorentzian line shape. Nevertheless, reasonable fits can be made with this line shape for many of the peaks observed [145]. An example is provided by the peak around $V_g = 291.6\,\mathrm{mV}$ in Fig. 4.1(b), where the shape of $T(E)$ affects the conductance only through the area of the peak, as discussed shortly for strong bias.

4.1.2 Measurements and analysis - I

Figure 4.2 shows the circuit used for this thermometry method. Two 1 MΩ resistors are set on either side of the heating channel. The DC voltages from the *NiQaq-9178* are applied to the left resistor, providing constant currents in the channel going to the ground after the right resistor. An AC voltage of $0.1V$ from the lock-in Amplifier of *SR7265*, goes through a transformer first and then a 1/10000 potential divider, to provide an excitation voltage of $10\,\mu$V across the device. The small bias voltage drives an electron current through the quantum dots, and it will be converted into voltages afterwards through the current-to-voltage pre-amplifier. The converted voltages will eventually be sent back to the lock-in amplifier, where the signals will be collected via computer. A DC voltage from -0.1 V to 0.22 V is applied to the heating channel, to provide different temperature profiles in the cavity, and the conductance through the left dot is measured by the lock-in amplifier while its resonance is changed by sweeping the plunger-gate voltage. The right dot barriers are not tuned to form a quantum dot, but a 1D channel to have a relatively closed cavity to resemble the temperature profile of the device during thermal power measurements.

Figure 4.3 shows the measurements using the above circuit. Figure 4.3 (a) shows the gray scale of differential conductance while DC currents from –50 nA to 50 nA are applied in the heating channel. One can see that both the height and the width of conductance peaks increase with rising heating currents, as shown in the highlighted area in the green dashed box. Interestingly, the differential conductance has formed several diamond-like shapes in which the conductance is near zero, and therefore the electronic transport has been suppressed, like the Coulomb diamonds discussed in Section 2.2.3. However, these thermal diamonds are not complete, because the resonance voltages change with the DC currents applied in the heating channel, especially when the currents switch from negative to positive values. Here the likely origin of the jumps in the peak positions are because of a bias voltage accidentally generated during measurements, which will be discussed in detail later in this section. These features can be seen more clearly in Fig. 4.3(b), where conductance is plotted as a line graph with offset of 5×10^{-8} *S*. A group of Coulomb peaks, as shown in Fig. 4.3, is chosen to fit equations for conductance peaks as discussed in the previous section, to extract the electron temperatures. The line graph of these chosen Coulomb peaks can be found in Fig. 4.3(d), where the peak changes are more visible.

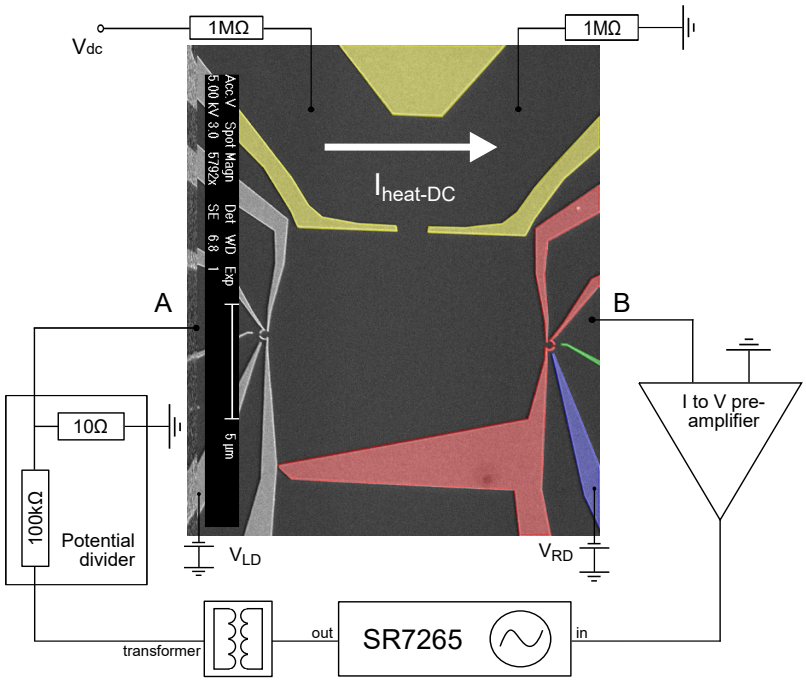

Fig. 4.2 False-colour SEM image of the device with the electrical circuit used for the temperature measurement I.

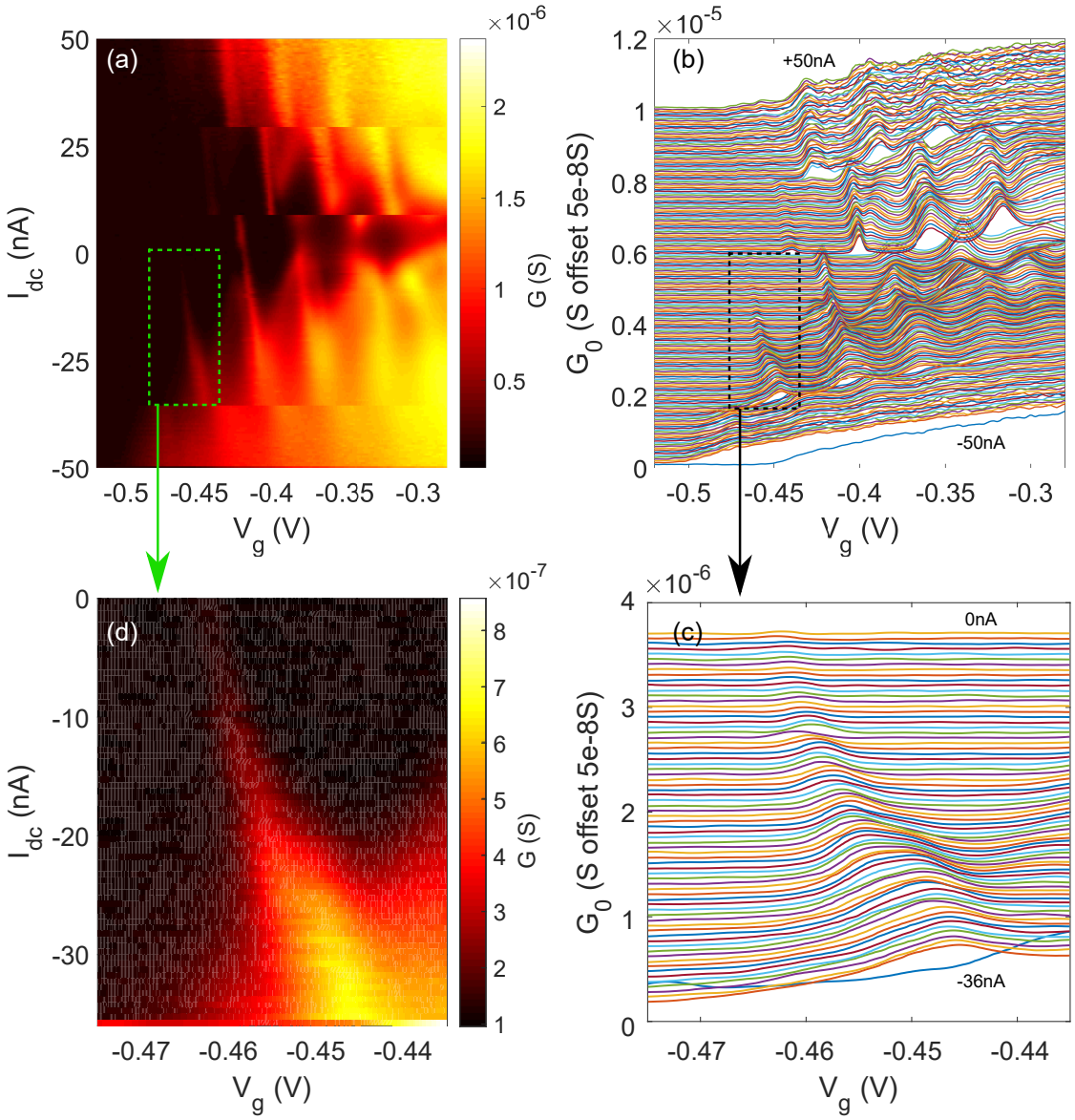

Fig. 4.3 Measurement results: (a) grey scale of the differential conductance, $G = dI/dV$. (b) the line graph of this conductance with 5×10^{-8} S offset. (c) is the selected differential conductance for temperature analysis. (d) is the corresponding line graph.

The data in Fig. 4.3 (c) is first fitted to the thermally broadened Lorentzian shape in Eq. (4.3), namely,

$$G = \frac{e^2}{h} \frac{1}{4k_B T} A \cosh^{-2}\left(\frac{E - E_{res}}{2k_B T}\right).$$

Here, $E = e\alpha V_G$ and $E = e\alpha V_{res}$ are the energy of the dot level and the energy of resonance respectively, where V_{res} is the voltage of the plunger gate when the conductance reaches the highest point, with $\alpha = 0.015$ being the lever arm of the plunger gate ascertained via

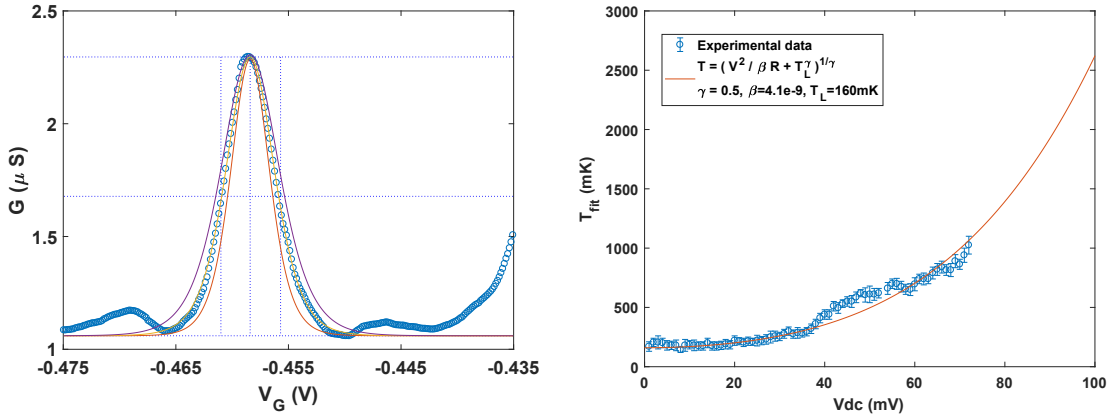

Fig. 4.4 (a) A representative Coulomb-resonance peak, measured at a base fridge temperature 120 mK and with a DC heating bias of 28 mV applied to the heating channel. The circles are the experimental data points and the orange lines is a theoretical fitting using Eq. (4.3). (b) the temperatures extracted from different DC heating voltages, using Eq. (4.3); The orange line shows the general relationship between the energy loss rate $P = U^2/R$ and temperature in the 2DEG, which gives a lattice temperature of $T_l = 160$ mK.

measurement of the Coulomb diamonds for the dot. A is the temperature-independent energy-integrated strength of the resonance, which has been defined separately for each conductance peak. Figure 4.4(a) shows a typical fitting example from Eq. (4.3). For DC voltages from $0.01V$ to $0.071V$, Equation (4.3) gives a temperature range from 160 mK to 1.05 K, shown as Fig. 4.4 (b).

The energy loss rate P from a 2DEG generally obeys $P = I^2R = U^2/R = \beta(T^\gamma - T_L^\gamma)$, where T is electron temperature and T_L is the lattice temperature [123]. This can be used to detect the electron and phonon interaction regimes of such a device, and confirm the accuracy of the extracted electrical temperature. In a macroscopic $GaAs/Al_xGa_{1-x}As$ heterojunction below 1K, the energy loss is dominated by the emission of acoustic phonons via the piezoelectric interaction, leading to a $\gamma = 5$ dependence. For $T \sim 500$ mK, the heated electrons relax to T_L over a distance $l_\text{e-ph} \sim 200\,\mu$m, and as T is lowered further $l_\text{e-ph}$ can significantly exceed the sample size [123]. In this regime, the energy loss is achieved via electron heat transport along the channel to the contacts. The T profile can then be calculated, using the Wiedemann-Franz law, and is found to give $\gamma = 2$ [123]. The general energy loss rate is plotted as the orange line in Fig. 4.4(b). Our data shows the best fit to this general rule with $\gamma = 0.5$ and $\beta = 3.3 \times 10^{-9} WK^{-0.5}$, which, however, does not fit with the discussions above. It is noted that, for an applied 100 mV DC voltage, namely, 50 nA in the heating channel, Equation (4.3) suggests an electron temperature of 2.5 K. This is unrealistically high for our measurements, especially given that the base temperature is stably at 50 mK. Also,

these extracted temperatures result in a big difference between the experimental data and the theoretical predictions.

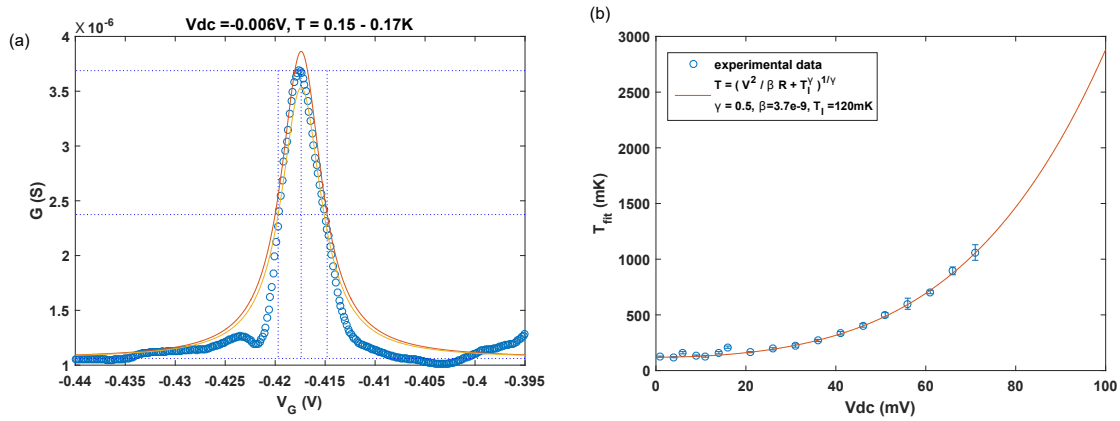

Fig. 4.5 (a) A representative Coulomb resonance peak, measured at a base fridge temperature of $T_l = 120\,\mathrm{mK}$ and with a DC heating bias of 6 mV applied to the heating channel. The circles are the experimental data points and the orange line is a theoretical fitting using Eq. (4.4). (b) The temperatures extracted from different DC heating voltages, using Eq. (4.4); The orange line shows the general relationship between the energy loss rate $P = U^2/R$ and temperature in 2DEG, which give a lattice temperature of $T_l = 120\,\mathrm{mK}$.

The same group of Coulomb peaks are then fitted with the thermally broadened Lorentzian parametrised lineshape in Eq. (4.4), namely,

$$G = \frac{e^2}{h}\frac{1}{4k_BT}A\int_{-\infty}^{\infty}\cosh^{-2}\left(\frac{E}{2k_BT}\right)\times\frac{(\Gamma/2)\pi}{(\Gamma/2)^2+[(e\alpha V_g - E_{res})-E]^2}dE.$$

Here Γ is the full-width at half-maximum at each Coulomb peak. For DC voltages from $0.01V$ to $0.071V$, Equation. (4.4) gives a temperature range from 120 mK to 1.06 K, shown in Fig. 4.5(b). Despite the fact that the electron temperatures from this estimation are lower than those from using Eq. (4.3), they are still higher than the theoretical predictions. For an applied 100 mV DC voltage, the extracted temperature of 2.0 K is also too high for our measurements. Figure 4.5(b) shows the power-loss general rule $P = I^2R = U^2/R = \beta(T^\gamma - T_L^\gamma)$ is best fitted with $\gamma = 0.5$, which is not close to the expected value of 5. Therefore, fitting the conductance with the thermally broadened lineshapes (Eq. (4.3)) does not solve the problem.

Besides the unsuccessful fits with Lorentzian lineshapes above, another puzzling issue is what is the thermal diamonds in Fig. 4.3(a). If we look only at the resistance of the measurement circuit shown in Fig. 4.2, we can find that the 1 MΩ resistors beside the heating channel in series with the resistance of about 20 kΩ of the 1D channel from right dot barriers and the resistance of about 3 MΩ from the left quantum dots, as shown in Fig. 4.6. The

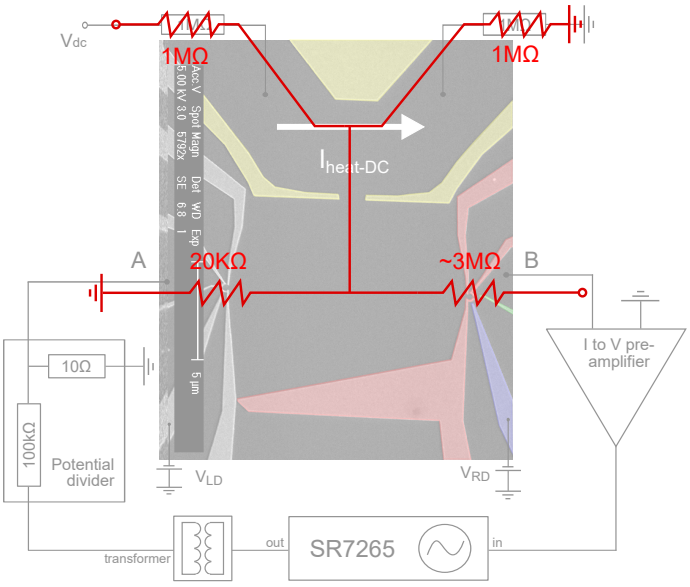

Fig. 4.6 The resistance analysis of the electrical circuit used for Temperature measurement-I.

2DEG and the heating channel have resistances of about a few hundred Ω and have been ignored here. It can be seen that the 1 MΩ before the heating channel and the 1D channel resistance of right barrier gates together can form a potential divider of 1/50 across the device. The DC voltages from the *NiDaq* are therefore divided by this accidentally formed potential divider generating a bias voltage directly into the 2DEG across the left dot. When the DC voltages from *NiDaq* increase, the bias window across the dot also increases, until eventually two continuous energy levels of the quantum dot overlapped, giving the diamond shapes detected in Fig. 4.3(a). However, it is different from the Coulomb diamonds discussed in Section 2.2.3 in Chapter 2, because the increasing currents in the channel do not only increase the bias voltage across the left dot, but also increase the temperature of the cavity. Therefore, these diamonds we saw are the 'Coulomb diamonds' at various temperatures. Because the bias voltages are directly applied to the 2DEG, the varying bias voltages will be also changing the effective gate voltages relative to the 2DEG, and therefore changing the lifetime of the left quantum dot. This is why the Eq. (4.3) and Eq. (4.4) failed to extract the electron temperatures here accurately.

4.1.3 Measurements and analysis - II

Based on the discussion in the previous section, we designed a new measurement circuit shown in Fig. 4.7. Two potential dividers of 10k Ω/100k Ω are set on either side of the heating channel, followed by a 1 MΩ resistor, to provide constant currents in the channel.

DC voltages of the same magnitude but opposite signs are applied simultaneously to either side of the heating channel via a *NiDAQ-9178*, to avoid a bias voltage being generated across the quantum dots. Two capacitors of 22 μF and 47 μF are set on either side of the cavity, to block DC heating currents from leaking through the dots. The heating currents therefore only go to the ground of the potential divider on the other side the heating channel. The differential conductance, $G = dI/dV$, is measured through the left quantum dot while different DC heating currents are applied in the channel, and the cavity is defined.

Figure 4.8 shows the measurements using the circuit in Fig. 4.7. Figure 4.8(a) shows the gray scale of the differential conductance while DC currents from 0 nA to 100 nA are applied in the heating channel. The thermal diamonds spotted in Fig. 4.3(a) did not appear, and thus neither any bias voltage across the dot is produced, unlike before. The height and the width of the conductance peaks increase with rising heating currents in Fig. 4.8 (b), though the change is less obvious than that in Fig. 4.3 (b). The last group of Coulomb peaks, as shown in Fig. 4.8 (c), are chosen to fit the theoretical models discussed in Section 4.1.1. Figure 4.3 (d) depicts the line graph of these chosen Coulomb peaks with an offset conductance of 3×10^{-7} S.

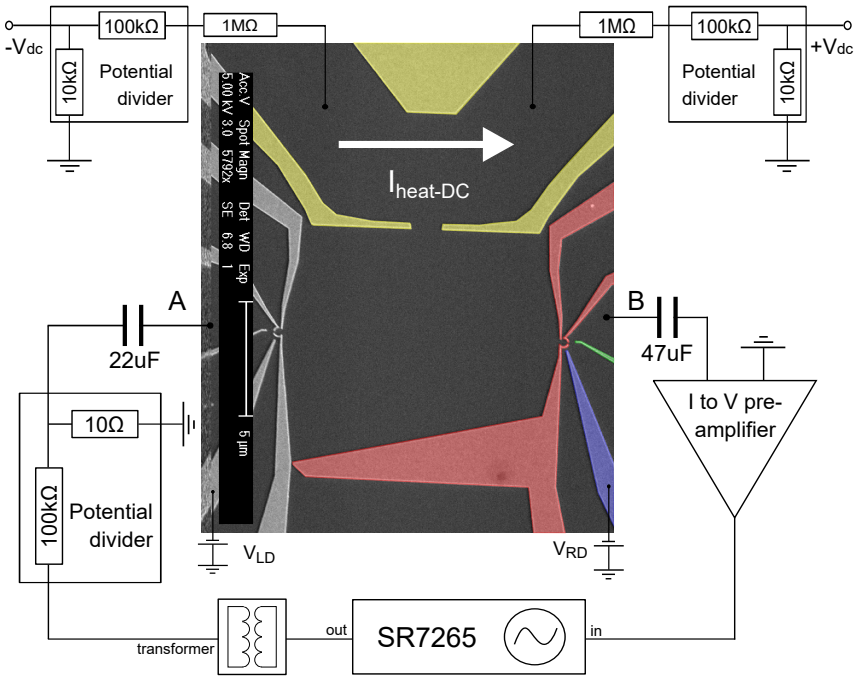

Fig. 4.7 False-colour SEM image of the device with the electrical circuit used for the temperature measurement II.

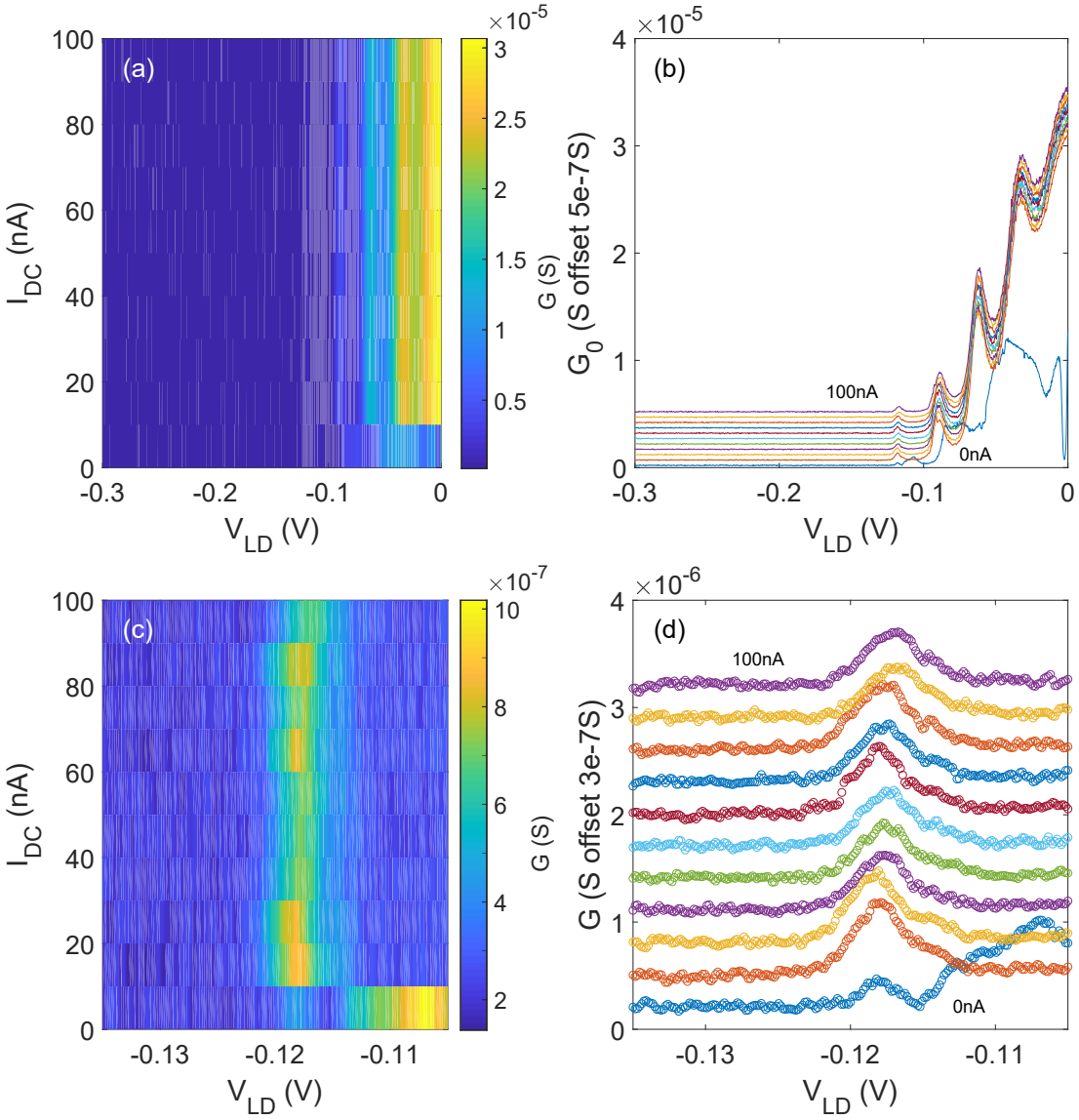

Fig. 4.8 Measurement results: (a) grey scale of the differential conductance, $G = dI/dV$. (b) Line graph of these conductance with 5×10^{-7} S offset. (c) is the selected differential conductance for temperature analysis. (d) is the corresponding line graph of the raw conductance data.

To extract the temperature of the cavity at each DC heating current, G is fitted to a thermally broadened Lorentzian, parameterised in Equ.(4.4), namely,

$$G = \frac{e^2}{h}\frac{1}{4k_BT}A\int_{-\infty}^{\infty}\cosh^{-2}\left(\frac{E}{2k_BT}\right)\times\frac{(\Gamma/2)\pi}{(\Gamma/2)^2+[(e\alpha V_g - E_{res})-E]^2}dE.$$

Here $\alpha = 0.025$ the lever arm of the plunger gate, ascertained via measurement of the Coulomb diamonds for each dot. For DC currents from 0 to 100 nA, Equation (4.4) gives a temperature range from 75 mK to 150 mK, as shown in Fig. 4.9(b). Our data shows the power dissipated per electron[116] is best fitted with $P = I^2R/(n_eC) = \beta(T_C^5 - T_0^5)$ with $R = 500^{\cdot}$, $C = 350\,\mu\text{m}^2$ and $\beta = 1.8\times10^{-15}\,\text{WK}^{-5}$, shown as the red line in Fig. 4.9(b). Here, I is the heating current, R is the resistance of the heating channel and C is the area of the heating channel. This T^5 behaviour was attributed to the acoustic phonon scattering in the Bloch-Grüneisen regime in the heating channel, with coupling via a screened piezoelectric potential [112]. The $\beta = 1.8\times10^{-15}\,\text{WK}^{-5}$ is larger than the theoretical prediction of $9.6\times10^{-18}\,\text{WK}^{-5}$ ($60\,\text{eV/sK}^5$) [116]. This can be because some heat is leaking through ohmic contacts at each end of the heating channel. Also, we assume the central cavity and the reservoir of the heating channel share the same temperature T_C, and the left and the right reservoirs have the same temperature with the base temperature, $T_L = T_R = T_0$. The base temperature estimated by this analysis is 75 mK. The quantum dot was used as the thermometer in this experiment,

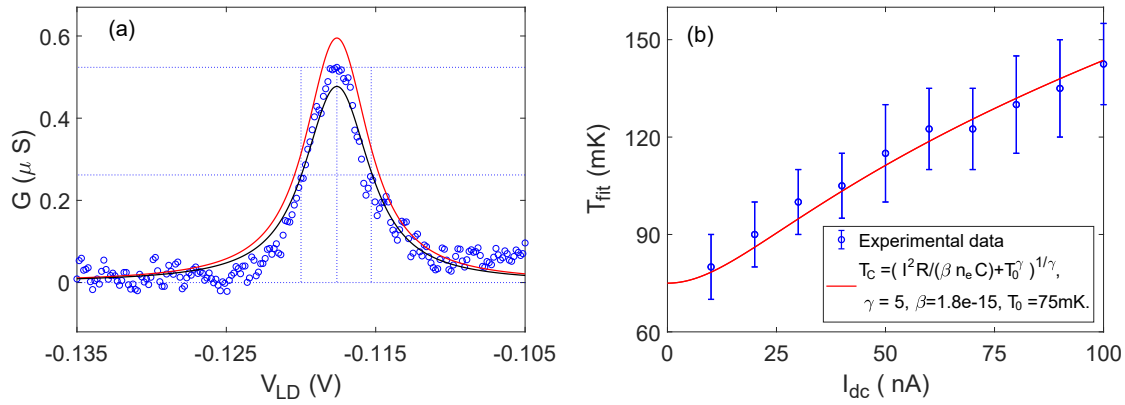

Fig. 4.9 (a) Conductance G plotted versus plunger voltage V_{LD}. The plot is a representative Coulomb resonance peak, measured at a lattice temperature of 75 mK and with a DC heating current of 30 nA applied to the heating channel. The circles are the experimental data points and the red and the black lines are the minimum 90 mK and maximum 110 mK theoretical fits by using Eq. (4.4). (b) The blue dots are the estimated electrical temperatures T_C using Eq. (4.4), with the fitting method shown in (a), and the red line is the corresponding general relationship between the energy loss rate and the temperature.

because it has greater accuracy than the thermometer in the mixing chamber of this dilution refrigerator, which gave a base temperature of 50 mK.

Overall, the experimental data (in Fig. 4.8) with the circuit in Fig. 4.7 provide a realistic electron temperature for such a QDEH device, and for the 60 nA, 80 nA and 100 nA applied in the heating channel, we extract temperatures T_e of 122 mK, 132 mK and 145 mK respectively.

4.1.4 The DC bias

Next we consider the case where the bias is so large that electrons from the right cannot contribute. We measure energies with respect to the left-hand lead. The bias V pulls down the resonant state by about $V/2$ if the structure is symmetric, so $E_{pk}(V) \approx E_{pk}(0) - eV/2$. Hence the resonance is pulled through the range of incident energies by the bias. At low temperature, where the electrons are highly degenerate, the Fermi occupation functions can be approximated by a step function. Equation 2.20, therefore, gives the currents as $I = 2e/h \int_{\mu_R}^{\mu_L} T(E)dE$. Usually the right-hand electrons all have energies below the resonance and can be neglected. Very little current flows when the peak lies outside the range of integration, $E_{pk} < U_L$ or $E_{pk} > \mu_L$. Between these limits, the resonance lies well inside the range of integration and the only significant contribution is around the peak. it is then a good approximation to extend the integral over E from (U_L, μ_L) to $(-\infty, +\infty)$, and [69]

$$I \approx \frac{2e}{h}\int_{-\infty}^{\infty} T(E)dE = \frac{2e}{h}T_{pk}\int_{-\infty}^{\infty}[1+(\frac{E-E_{pk}}{\Gamma/2})^2]^{-1}dE = \frac{2e}{h}\frac{\pi}{2}\Gamma T_{pk}. \tag{4.5}$$

The current remains constant at this value while the peak remains well inside the range of incoming energies, and it falls to zero over a width of about Γ as E_{pk} passes outside this range. It is important that the current depends on the integral of $T(E)$, not just its peak, and is therefore proportional to the width Γ. Although $T_{pk} = 1$ for a symmetric structure even if the barriers are highly opaque, the width is extremely small in this case and only a small current flows. If the barriers are very different, the approximate form gives $T_{pk} \approx 4T_</T_>$, where $T_>$ and $T_<$ are the greater and lesser of T_L and T_R [69]. Thus a device with opaque barriers passes a small current, as seems physically reasonable, despite its high peak in transmission. Expanding Γ and T_{pk} in equation 4.5 gives [69]

$$I = 2\frac{eV}{2a}\frac{T_L T_R}{T_L + T_R} \approx \frac{evT_<}{a}, \tag{4.6}$$

which confirms that current is limited by the more opaque barrier. Here, as before, a is the width of the quantum well (dot), and v is the velocity of an electron in the resonance. The bias voltage has at least three major effects on the electronic structure: it changes the

Fermi level, shifts the energy of the resonant state, and alters the profiles and transmission properties of the barriers. The first two are essential, but for simplicity the changes they cause in T_L and T_R have been neglected although this approximation can rarely be fully justified in real experiments.

In practice, for the case of the opaque barriers ($\Gamma \ll k_B T$), the current through the dot with a finite bias across it can be calculated easily [58], and Equation (4.6) becomes

$$I \propto f(\mu_{dot}, \mu_S) - f(\mu_{dot}, \mu_D). \tag{4.7}$$

As discussed above, the resulting line-shape is approximately a 'top-hat'. The width of the top-hat is proportional to the magnitude of the bias applied across the dot, and the height of the top hat is determined by the transmission coefficients of the two barriers. The widths of the two sloping sides are determined by the thermal broadening of the two leads, respectively. Equation (4.7) can therefore be used to extract the temperature of the leads by measuring the current through a quantum dot. Further, the temperatures of the two leads can be determined independently by fitting two Fermi-Dirac functions to the two sides of the top-hat line-shape.

4.2 The quantum point contact

One of the most significant experimental advances in gated semiconductor quantum dot measurements was the realisation of the 'point-contact detector' [146]. This tool allows one to measure changes in the charge state of a dot without making any direct electrical connection to it. The principle of the point-contact detector is to use the highly non-linear differential conductance characteristics of a 1D wire (the point-contact) placed in close proximity to the dot as a sensitive probe of the local electrostatic environment. A change of the dot's average charge by less than a single electron can alter the electrostatic potential of the 1D channel significantly enough to produce a measurable change in its conductance.

4.2.1 Theory

Figure 4.10 is a schematic of the thermometry method. The thermometer consists of a quantum dot tunnel coupled to the 'domain' whose temperature is to be determined. A one-dimensional channel (a quantum point contact (qpc)) is defined adjacent to the quantum dot. As the energy level of the thermometer dot is swept past the thermally broadened chemical potential of the domain, the occupation probability of this level in the dot changes. If the lifetime broadening of the resonant state in the dot Γ is less than $k_B T$ then the response of the qpc current is proportional to this (charge) occupation probability, which in turn is given

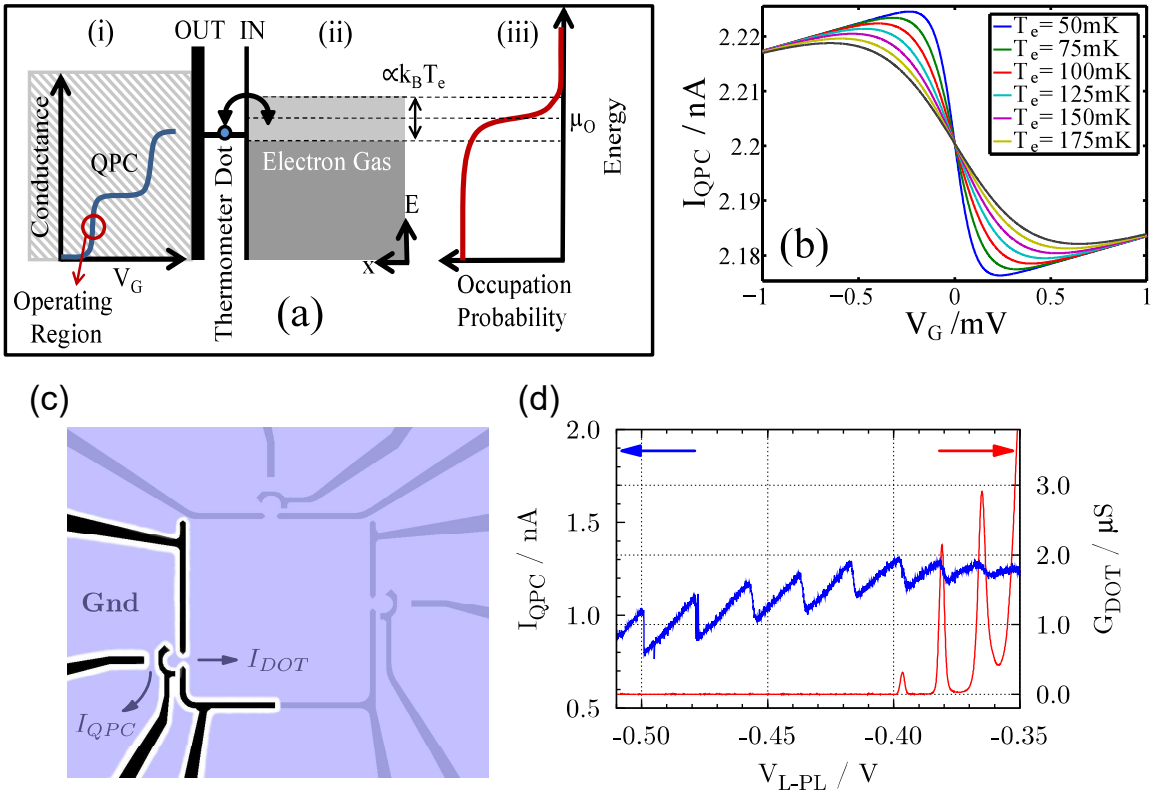

Fig. 4.10 (a) Schematic of the thermometry set-up. (i) The quantum point contact monitors the charge occupation of the thermometer dot. (ii) The dot is tuned so that it is opaque to the 2DEG on the left and partially transparent to the 2DEG on the right (the 'domain'). (iii) The width of the resulting Fermi-Dirac distribution gives the temperature of the electron gas. (b) Calculated current through the qpc as a function of the voltage on the plunger gate for different electron temperatures. The constants used in the calculations were extracted from experimental data: bias across the qpc leads $V_b = 100\mu V$, lever arm of the plunger gate on the dot potential $\alpha = 0.085$, lever arm of the dot on the qpc potential $\beta = 0.0063$, lever arm of the plunger gate on the qpc potential $\gamma = 0.0052$, charging energy of the dot $e^2/C_\Sigma = 51.9\,\mathrm{meV}$, the extent of confinement of the qpc potential in the longitudinal direction $\hbar\omega_x = 2.5\,\mathrm{meV}$, and reference energy of the qpc potential $E_0^{qpc} = -2.8\,\mathrm{meV}$. Panel (c) shows the gates used in a similar device for the same measurements, with the blue regions depicting the un-depleted 2DEG. Both the conductance of the dot ($G_{DOT} = dI_{DOT}/dV_{SD}$) and the current through the adjacent point-contact (I_{QPC}) are plotted in (d). On the right side of the plot, the steps in I_{QPC} coincide with the Coulomb-blockade peaks of the dot. They are interpreted as being caused by the change in charge state of the dot.

by the energy distribution in the electron gas. Since the electrons in the two-dimensional electron gas have a constant density of states, their energy spectrum is entirely described by the Fermi-Dirac distribution ($f(E) = 1/(1+e^{(E-\mu)/k_BT})$), where μ is the chemical potential of the gas, T is temperature, and k_B is the Boltzmann constant. A scaled Fermi-Dirac distribution can thus be fitted to the measured detector current, and the electron temperature can then be extracted from the fit.

The thermometer dot is operated in the Coulomb-blockade regime, which means that both the charging energy of the electron and the electronic level spacing are much greater than the thermal energy of the electrons, k_BT_e. As a result, electron tunnelling only takes place between the dot and a single energy level [147]. In our experiments, We further require the intrinsic lifetime broadening $\hbar\Gamma$ to be much smaller than k_BT_e, so that we can neglect intrinsic broadening effects. The dot is also set up so that the tunnel barrier to the domain is much more transparent than that to the qpc leads. The mean occupation of the dot is then given by $< n_{dot} >= f(E_0^{QD} - e\alpha V_G)$, where E_0^{QD} is a reference energy for the level, V_G is the voltage on the plunger gate and α the lever arm of the plunger gate on the dot.

The current through the qpc can be expressed using the Landauer-Büttiker formalism[148]:

$$I_{qpc} = \frac{2e}{h}\int_{-\infty}^{\infty} dE\,\mathscr{T}(E,E^{qpc})[f(E-eV_b,T_L)-f(E,T_L)]. \tag{4.8}$$

Here T_L is the temperature of the qpc leads (in general $T_e \neq T_L$), V_b is the bias applied across the leads, and $\mathscr{T}(E,E^{qpc})$ is the energy-dependent transmission coefficient of the qpc. For a single ballistic channel in a one-dimensional channel described by a saddle-point potential [149], $\mathscr{T}(E,E^{qpc}) = [1+\exp(-2\pi(E-E^{qpc})/\hbar\omega_x)]^{-1}$, where $\hbar\omega_x$ is a characteristic energy of the confinement and E^{qpc} denotes the bottom of the potential for the one-dimensional electron channel defined by qpc.

Upon changing the plunger-gate voltage V_G, the potential landscape at the qpc changes due to the capacitive couplings QPC-QD and QPC-gate. As these couplings are small, they are regarded as perturbations and their effect is modelled by a shift of the potential E^{qpc} with respect to a reference value E_0^{qpc}. Then E^{qpc} can be written as

$$E^{qpc} = \beta\frac{e^2 < n_{dot} >}{C_\Sigma} - e\gamma V_G - E_0^{qpc}. \tag{4.9}$$

Here β is the lever arm of the dot on the qpc, and γ is that of the plunger gate on the qpc. In general, it is expected that $\gamma \ll \beta$ [147].

In the limit $eV_b, k_BT_L \ll \hbar\omega_x$, $\mathscr{T}$ is approximately constant in the range where the electron distributions of the leads vary. The expression for current can then be simplified as:

$$I^{qpc} = \frac{2e^2}{h}\mathscr{T}(0, E^{qpc})V_b. \tag{4.10}$$

Although T_L no longer appears in this expression, T_e determines the dot occupation $< n_{dot} >$, which affects E_{qpc}, and hence the transmission coefficient $\mathscr{T}$. To first order, $\mathscr{T}$ is linear in V_G about $\mathscr{T} \approx 0.5$, and the above equation can be reduced to the following simple form [144]:

$$I^{qpc}(V_G) = \frac{n}{1 + exp(e\alpha(V_G - \mu_C)/k_BT_e)} + lV_G + C, \tag{4.11}$$

(where n is a normalisation constant, l models the capacitive effect of the plunger-gate voltage on the qpc potential, μ_C is the offset in gate voltage of the centre of the resonance, and C is the current at the operating point of the qpc). Figure 4.10(b) shows the qpc current as a function of V_G calculated using the above equation, for different values of T_e. To reduce the effects of noise, several scans are averaged, and a Fermi-Dirac function fitted to the resulting curve to extract the electron temperature.

Figure 4.10(c) shows a device used for such a thermometry measurement by Prance *et al.* [138]. Three gates were tuned to define a quantum dot. The adjacent point contact was set to a region of highly non-linear differential conductance, and therefore high detector sensitivity, with the detector (qpc) gate. A point-contact conductance of approximately $5\,\mu$S was found to give the best detector sensitivity. Figure 4.10 (d) shows the conductance of the dot and the detector current as a function of the voltage (V_{L-PL}) on the plunger gate of the dot. As expected, the detector current shows clear upward steps each time the charge occupancy of the dot decreases by one electron. The steps persist long after transport through the dot is visible, providing information about the dot when it is very weakly coupled to its reservoirs. On the far left side of the plot the tunnel rates of the dot barriers are lower than the measurement bandwidth of I_{QPC}. The qpc signal therefore no longer reflects the average charge occupancy of the dot, but shows sharp steps that correspond to single-electron tunnelling events [138].

4.2.2 Measurement and analysis

Figure 4.11 shows an SEM image of the measured device, along with the electrical circuit used in the experiments. The surface gates define a 'thermometer' quantum dot with an associated quantum point contact (qpc) gate, and a square domain whose temperature is measured using the thermometer dot. The quantum dot, with a radius of 310 nm, was set

up using three gates (coloured red). The chemical potential of the dot was controlled by applying a voltage to the plunger gate (in blue). A detector gate (the qpc gate in green), 250 nm apart from the quantum dot, was used to define a narrow 1D channel adjacent to the thermometer dot. An excitation voltage of 0.1 V, from an SR7265 lock-in amplifier, is applied to the transformer and then to a potential divider of 1/10000, to drive a current through this narrow channel. The current signal, after the qpc channel, was converted into voltage via a current-to-voltage amplifier, which was then read by the SR7265 lock-in amplifier. Measurements were performed in ^{3}He/^{4}He dilution refrigerator at a base (lattice) temperature of 50 mK. The characterised thermometer can now be used to measure the temperature of the domain. The measurements consist of measuring the current in the qpc at the operating point as the voltage on the plunger gate is changed. The temperature can be extracted by fitting Equation (4.11) to the data. Unfortunately, we did not see the charge fluctuations like those shown in Fig. 4.10(d).

The design of the qpc gate provides an insight into the failure of the thermometer quantum dot in our measurements. In Mavalankar's work [144], the qpc gate was designed to be 210 nm apart from the thermometer quantum dot, 40 nm less than that in our designs. This means that a larger voltage is required on the qpc gate to pinch off the channel. The qpc gate in our device also is designed to have a narrow width of 50 nm. This increases its vulnerability

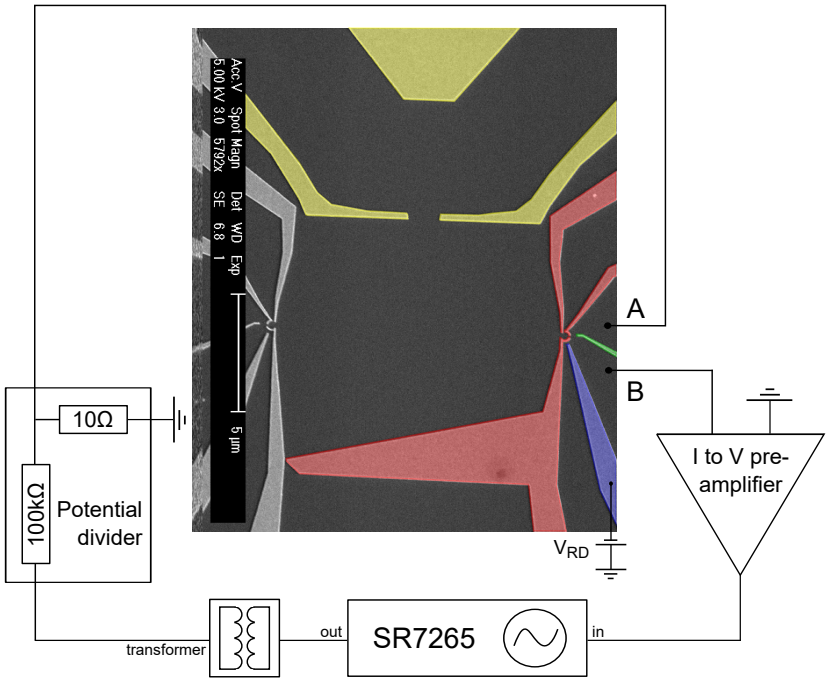

Fig. 4.11 The electrical circuit used for the qpc current measurements.

to be blown off during fabrication or when loading the device into the refrigerator. This may make it impossible for it to form a 1D channel near the quantum dot.

4.3 Seebeck coefficient

4.3.1 Theory

In Section 2.6.3 in Chapter 2, we have discussed that when both charge and heat are exclusively carried by electrons, the Seebeck coefficient (also known as thermopower), the conductance and the electrical temperatures will together follow the Mott relation. Appleyard *et al.* first used this relation as a thermometer in 1998. They measured the temperature of a 2DEG in GaAs from the thermopower of a one-dimensional ballistic constriction, through the device shown in Fig. 4.12 (a), and confirmed the calibration form the electrical

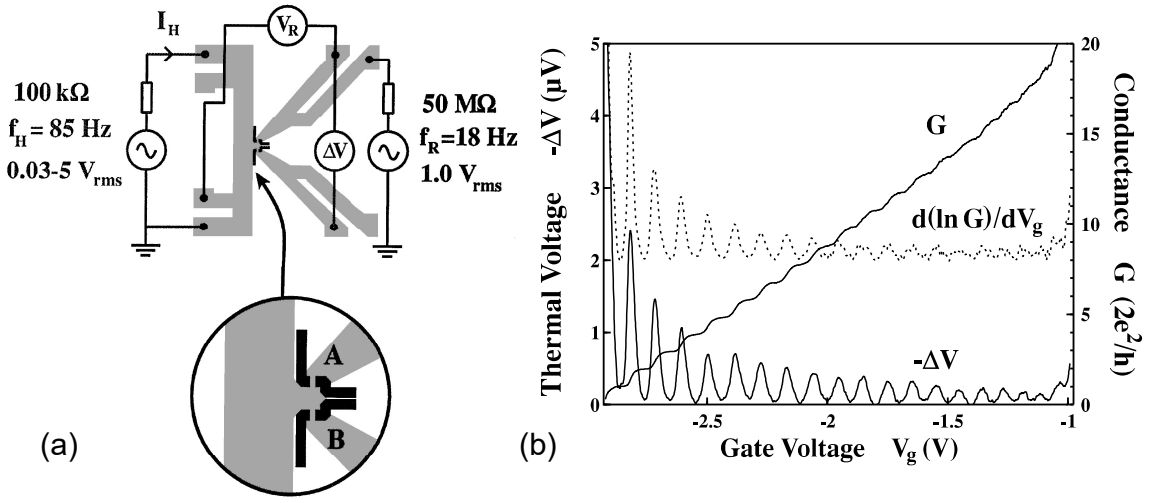

Fig. 4.12 (a) Schematic of the device and measurement circuit. The etched mesa, shown in grey, consists of heating channel and two voltage probes, where the two 1D constrictions are defined. The four-terminal resistance R is measured simultaneously with the Seebeck coefficient S, but at a different frequency. Magnified view: the two pairs of split gates defining the constrictions A and B are shown in solid black. (b) Experimental traces of the conductance G (derived from R) and the Seebeck coefficient voltage $-\Delta V$ from constriction A, using a heating current $I_H = 1.5\,\mu$A at a lattice temperature $T_l = 305$ mK, so that $T_e \approx 600$ mK. The dashed line shows the predicted Seebeck coefficient signal $-\Delta V(V_g) \sim d(\ln G)/dV_g$ from the Mott relation of Eq. 4.12. This figure is adapted from Ref. [116].

conductance using the Mott relation of Equation (2.73), written as

$$\Delta V|_{I=0} = -\frac{\pi^2 k_B^2}{3e}(T_e^2 - T_l^2)\frac{\partial \ln G}{\partial \mu}. \tag{4.12}$$

Figure 4.12(b) presents their experimental results with the comparison to Equation (4.12).

4.3.2 Measurement and analysis

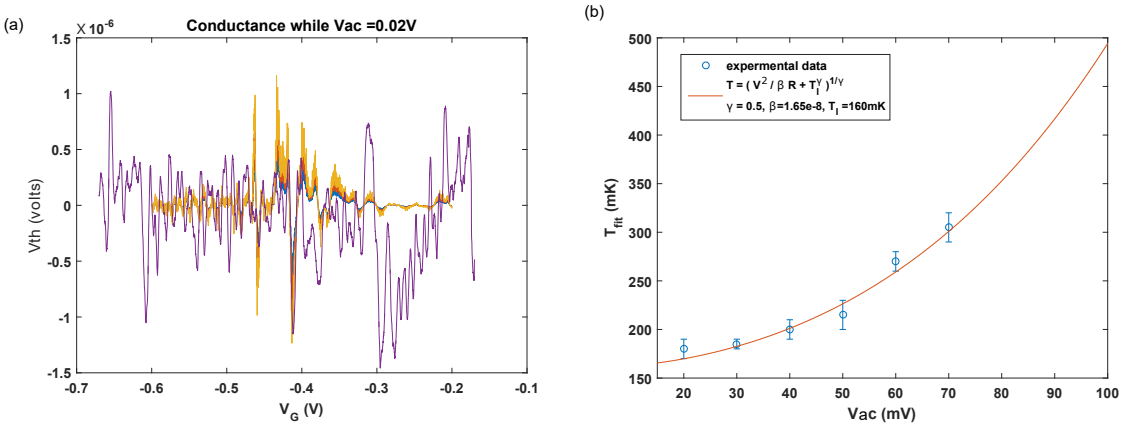

Fig. 4.13 (a) The purple line shows the thermopower measured between A and B in the measurement set-up shown in Fig.3.14(c), while $Vac = 20\,\mathrm{mV}$ is applied in a heating channel. The three overlapped lines of yellow, red and blue colours are the theoretical fitting from Eq. (4.13). (b) The temperatures extracted from different AC heating voltages, using Eq. (4.13); The orange line shows the general relationship between the energy loss rate and temperature in 2DEG, which give a lattice temperature of $T_l = 160\,\mathrm{mK}$.

We have applied such a method to our data, namely, fitting our thermopower data with the Mott relation,

$$S = \frac{\Delta V}{T_e - T_l}|_{I=0} = -\frac{\pi^2 k_B^2}{3e}(T_e + T_l)\frac{\partial lnG}{\partial \mu}. \tag{4.13}$$

As shown in Fig.4.13 (a), for $Vac = 20\,\mathrm{mV}$ to $Vac = 70\,\mathrm{mV}$, the above equation (or Eq. (2.73)) gives a temperature range from 180 mK to 305 mK with a lattice temperature of $T_l = 160\,\mathrm{mK}$, as shown in Fig. 4.13(b). The model gives an approach to measuring the electrical temperature in a 2DEG. The advantage of such a model is that we can extract the temperatures directly from the thermopower data, which is the main focus of this work. However, as shown in Fig. 4.13(a), the thermopower data are very noisy, because the device is heated with currents. It is difficult to have a very good fit unlike the curves in Fig. 4.12.

4.4 Conclusion

In summary, in this chapter, we have introduced the three methods we took to extract the electrical temperatures of our QDEH device.

Firstly, we extracted the electrical temperatures through fitting the differential conductance peaks with theoretical models. Transport through a quantum dot can also be measured using a dc set-up, in which the current is measured. The advantage of this method is that the quantum dot can directly serve as a thermometer. However, the excitation voltage, applied to drive currents through the quantum dots, will unavoidably heat the device. In addition, extracting the electron temperature from the transport measurements necessitates tuning the dot so that the tunnelling rates to the source and drain reservoirs are equal. If the barriers are unequal, the lifetime broadening of single-particle states in the dot will be determined by the more opaque transparent barrier. This limits the resolution of this thermometry method to the lifetime broadening of the dot states.

Then we introduced the quantum-point-contact thermometry, which extracts electrical temperatures via monitoring the changes in the charge state of a dot without having any direct electrical connection to the dot. It is easier to set up this measurement, because the absence of measurable transport through the thermometer dot necessitates high tunnel barriers to the source and drain reservoirs, which also reduces the probability of co-tunnelling. This means that the qpc thermometer is sufficiently isolated from the domain that the same tuning can be used for the entire operating range, whereas a conductive quantum dot might have to be retuned at higher operating temperatures. Also, the signal through a qpc is usually several times greater than the current through a quantum dot, which means that the qpc thermometer is much more sensitive than the quantum-dot thermometer for a similar experimental set up. However, the unsuccessful attempt in our measurements suggests that we need to improve the design and fabrication of our qpc detector gates.

The Mott relation is used as the third thermometry method in our work. It extracts the temperatures directly from the thermopower voltage, increasing the accuracy by using the same sets of measurement circuits and data. The challenge for this method is that the thermal power data are very noisy, and therefore the fits between experimental data and the theoretical model are not ideal.

Chapter 5

A double-quantum-well energy harvester

In the previous chapters, we have discussed the experimental realisation of a resonant-tunnelling quantum-dot energy harvester, its thermometry studies and the background knowledge. Such a device yields an output power of $0.1\,fW$ for a temperature difference of 67 mK between the hot and the cold reservoirs while at the same time it reaches an efficiency at maximum power with a lower bound around 10 % of the Carnot efficiency at maximum power. In the proposal of Jordan *et al.* [1], it has also been suggested to scale such a quantum-dot energy harvester device to macroscopic dimensions by parallelism based on the use of self-assembled quantum dots. Similar setups have also been investigated both theoretically [47, 48] and experimentally [49] in their dual role as refrigerators. They are however limited to low power.

In 2013, Sothmann *et al.* [2] proposed a three-terminal energy harvester based on resonant quantum wells. There are a number of advantages that this quantum-well structure has over a quantum-dot setup. Firstly, quantum wells should be able to deliver larger currents and, therefore, larger output powers because of the transverse degrees of freedom. The available phase space for electrons that can traverse the well is large. Secondly, a quantum-well structure might be easier to fabricate than a system of self-assembled quantum dots that should all have similar properties in order to yield a decent device performance, although there is good tolerance to fluctuations in dot properties. Finally, due to the large level spacing of narrow quantum wells, they are ideally suited for temperature applications. Apart from these advantages, the less optimal energy-filtering properties of quantum wells compared to quantum dots can reduce the efficiency of heat-to-current conversion, as quantum wells

transmit any electron with an energy larger than the level position whereas quantum dots transmit only electrons with an energy exactly equal to the level energy [2].

In this chapter, we will present the theoretical proposal of such a double-quantum-well energy harvester and our attempt at experimental demonstration. It includes the designs, the fabrication and the measurements. We will also analyse the causes for its failure and list possible improvements.

5.1 Theoretical proposal

5.1.1 Model

The quantum wells are assumed to be non-interacting such that the charging effects can be neglected in a simplified model. The effects of interaction will be revisited in the discussions of the non-linear regime.

The electronic reservoirs, $r = L, R$, are characterised by a Fermi function $f_r(E) = \{\exp[(E - \mu_r)/(k_B T_c)] + 1\}^{-1}$ with temperature T_c and chemical potential μ_r. The cavity is assumed to be in thermal equilibrium with a heat bath of temperature T_h. In reality, the heat bath can be any source from which we want to harvest energy. Strong electron-phonon and electron-electron interactions within the cavity relax the energy of the electrons entering and leaving the cavity towards the Fermi distribution $f_c(E) = \{\exp[(E - \mu_c)/(k_B T_h)] + 1\}^{-1}$ characterised by the cavity temperature T_h and the cavity chemical potential μ_c.

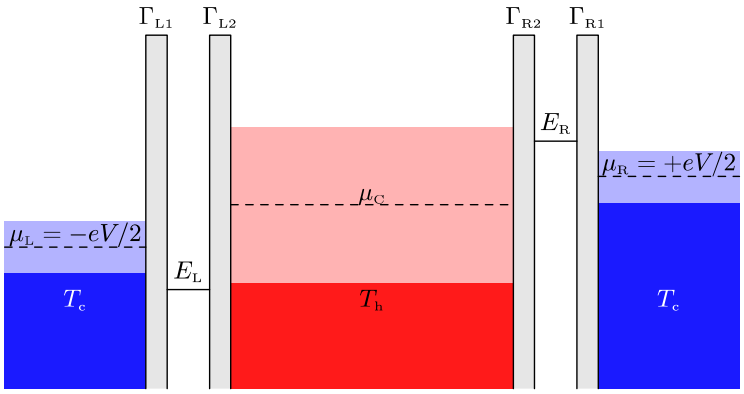

Fig. 5.1 Schematic representation of the quantum-well-based energy harvester. A central cavity (red) kept at temperature T_h by a hot thermal reservoir (not shown) is connected via quantum wells to two electron reservoirs at temperature blue T_c (blue). Chemical potentials are measured relative to the equilibrium chemical potential [2].

The cavity potential μ_c, as well as its temperature T_h (or, equivalently, the heat current J injected from the heat bath into the cavity to keep it at a given temperature T_h), have to be determined from the conservation of charge and energy, $I_L + I_R = 0$ and $J_L^E + J_R^E + J = 0$. Here, I_r denotes the current flowing from reservoirs r into the cavity. Similarly, J_r^E denotes the energy current flowing from reservoir r into the cavity. The charge and energy currents can be evaluated within a scattering-matrix approach as [2]

$$I_r = \frac{e\upsilon_2 A}{2\pi\hbar} \int dE_\perp dE_z T_r(E_z)[f_r(E_z + E_\perp) - f_c(E_z + E_\perp)] \tag{5.1}$$

and

$$J_r^E = \frac{\upsilon_2 A}{2\pi\hbar} \int dE_\perp dE_z (E_z + E_\perp) T_r(E_z)[f_r(E_z + E_\perp) - f_c(E_z + E_\perp)]. \tag{5.2}$$

Here, $\upsilon_2 = m^*/(\pi\hbar^2)$ is the density of states of the two-dimensional electron gas inside the quantum well with the effective electron mass m^*. A denotes the surface area of the well. E_z and $E_\perp$ are the energies associated with motion in the well's plane and perpendicular to it, respectively. The transmission of quantum well r is given by [137]

$$T_r(E) = \frac{\Gamma_{r1}(E)\Gamma_{r2}(E)}{(E - E_{nr})^2 + [\Gamma_{r1}(E) + \Gamma_{r2}(E)]^2/4}. \tag{5.3}$$

Here, $\Gamma_{r1}(E)$ and $\Gamma_{r2}(E)$ denote the (energy-dependent) coupling strength of the quantum well to the electronic reservoir r and the cavity, respectively. The energies of the resonant levels (more precisely the subband thresholds) within the quantum well are given by E_{nr}. For a parallel geometry with well width L, the resonant levels are simply given by the discrete eigenenergies of a particle in a box, $E_{nr} = (\pi\hbar n)^2/(2m^* L^2)$. In the following, it has always been restricted to the situation of weak coupling, $\Gamma_{r1}(E), \Gamma_{r2}(E) \ll k_B T_c, k_B T_h$, whose energy dependence can be neglected. Furthermore, it is assumed that the level spacing inside the quantum wells is large such that only the lowest energy state is relevant for transport. In the case, the transmission function reduces to a single delta peak, $T_r(E) = 2\pi\Gamma_{r1}(E)\Gamma_{r2}(E)/(\Gamma_{r1}(E) + \Gamma_{r2}(E))\delta(E_z - E_{1r})$.

5.1.2 Results

In the following discussions, both quantum wells are assumed to be intrinsically symmetric, i.e. $\Gamma_{L1} = \Gamma_{L2} \equiv (1+a)\Gamma$, $\Gamma_{R1} = \Gamma_{R2} \equiv (1-a)\Gamma$. Here, Γ denotes the total coupling strength where as $-1 \leq a \leq 1$ characterises the asymmetry between the coupling of the left and the right wells. To simplify notation, the temperature is introduced as the average temperature $T = (T_h + T_c)/2$ and the temperature difference $\Delta T = T_h - T_c$. To linear order in the temperature

difference ΔT and the bias voltage $eV = \mu_R - \mu_L$ applied between the two electronic reservoirs, Sothmann *et al.* extract the charge current through the system, the maximal output power and the efficiency at maximum power as below [2]:

$$I_L = -I_R = \frac{e\upsilon_2 A\Gamma}{2\hbar} g_1(\frac{E_L}{k_BT}, \frac{E_R}{k_BT})[-eV - k_B\Delta T g_2(\frac{E_L}{k_BT}, \frac{E_R}{k_BT})], \tag{5.4}$$

$$P_{max} = \frac{\upsilon_2 A\Gamma}{2\hbar}(\frac{k_B\Delta T}{2})^2 g_1(\frac{E_L}{k_BT}, \frac{E_R}{k_BT}) g_2^2(\frac{E_L}{k_BT}, \frac{E_R}{k_BT}), \tag{5.5}$$

$$\eta_{maxP} = \frac{\eta_C}{4} \frac{g_1(\frac{E_L}{k_BT}, \frac{E_R}{k_BT}) g_2^2(\frac{E_L}{k_BT}, \frac{E_R}{k_BT})}{g_3(\frac{E_L}{k_BT}, \frac{E_R}{k_BT})}, \tag{5.6}$$

with the auxiliary functions of

$$g_1(x,y) = \frac{1-a^2}{2+(1-a)e^x+(1+a)e^y} \tag{5.7}$$

$$g_2(x,y) = x - y + (1+e^x)\log(1+e^{-x}) - (1+e^y)\log(1+e^{-y}). \tag{5.8}$$

and

$$\begin{aligned} g_3(x,y) = {} & \frac{2\pi^2}{3} - \frac{1}{2}(x-y)g_1(x,y)[x-y-2g_2(x,y)] - 2(1+a)_2(\frac{1}{1+e^{-x}}) \\ & -2(1-a)\mathrm{Li}_2(\frac{1}{1+e^{-y}}) - 2(1+a)\log(1+e^x)\log(1+e^{-x}) \\ & -2(1-a)\log(1+e^y)\log(1+e^{-y}) - g_1(x+y)(1+e^x)(1+e^y)\log(1+e^{-x}) \\ & \times \log(1+e^{-y}) - g_1(x,y)\log^2(1+e^{-x})[e^x\sinh x + \frac{1+a}{1-a}e^x(1+e^y)] \\ & -g_1(x,y)\log^2(1+e^{-y})[e^y\sinh y + \frac{1-a}{1+a}e^y(1+e^x)], \end{aligned} \tag{5.9}$$

with the dilogarithm $\mathrm{Li}_2(z) = \Sigma_{k=1}^{\infty}\frac{z^k}{k^2}$. At $V = 0$, a finite current driven by $\Delta T \neq 0$ flows in a direction that depends on the position of the resonant levels. If, e.g., $E_R > E_L$, electrons will be transferred from the left to the right lead [2].

Figure 5.2 depicts the output power and the efficiency from this model [2]. Figure 5.2(a) shows the output power as a function of the level positions E_L and E_R. It is symmetric with respect to exchange of E_L and E_R. The maximal output power of approximately $P_{max} \approx \frac{\upsilon_2 A\Gamma}{2\hbar}(\frac{k_B\Delta T}{2})^2$ arises when one of the two levels is deep below the equilibrium chemical potential, $-E_{L/R} \gg k_BT$ while the other level is located at about $E_{R/L} \approx 1.5k_BT$.

Similarly to the power, the efficiency is also symmetric under an exchange of the level positions, as shown in Fig. 5.2 (b). It takes its maximal value of $\eta \approx 0.1\eta_C$ in the region $E_L, E_R > 0$ where the output power is strongly suppressed. For these parameters, energy filtering is efficient but the number of electrons that can pass through the filter is exponentially suppressed. For level positions that maximise the output power, the efficiency is slightly reduced to $\eta_{maxP} \approx 0.07\eta_C$. The efficiency at maximum power of the quantum-well heat engine is about a factor of three less than the efficiency at maximum power of a quantum-dot heat engine with level width of the order of $k_B T$ [1, 11]. The latter configuration has been shown to yield the maximal output power [1]. For the situation depicted in Figure 5.1, the right quantum well acts as an efficient energy filter because the number of electrons larger than E_R is exponentially small. The energy filtering at the left quantum well relies on a different mechanism. In order for an electron of energy E to enter the cavity, it needs $f_L(E) > 0$ so that the reservoir state is occupied. At the same time, it also requires $f_L(E) < 1$ such that a free state is available in the cavity. These conditions define an energy window of the order

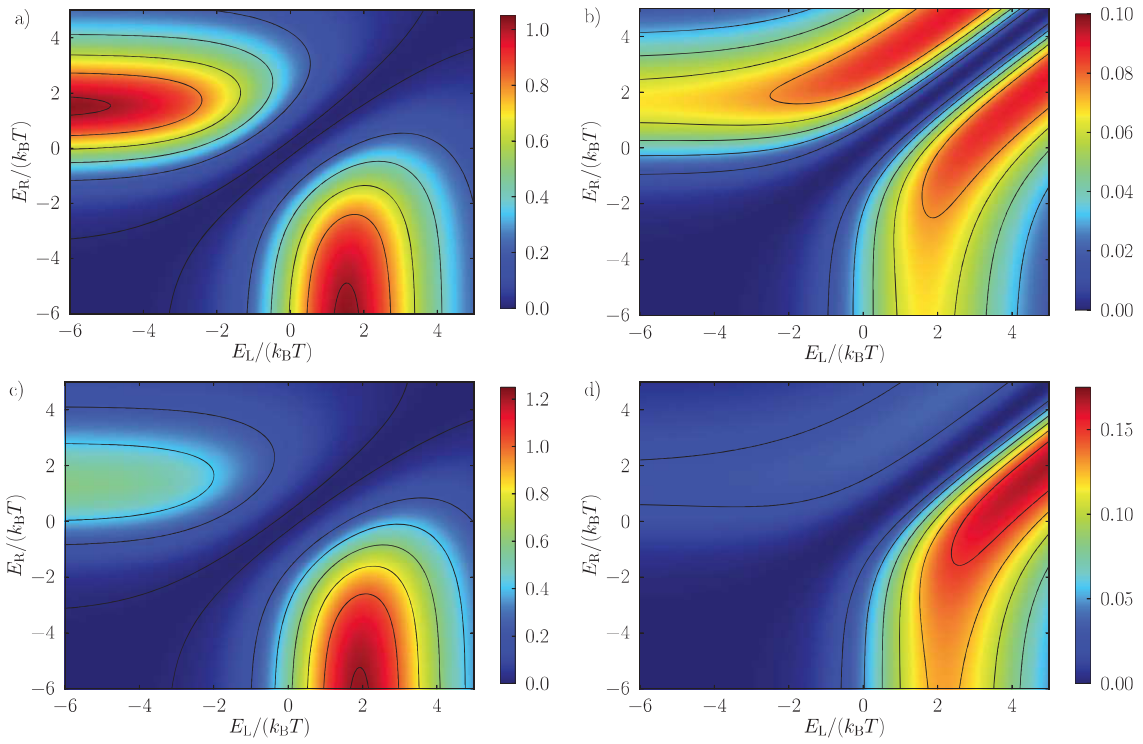

Fig. 5.2 (a) Maximum power in units of $\frac{\upsilon_2 A\Gamma}{2\hbar}(\frac{k_B\Delta T}{2})^2$ within linear response as a function of the level positions inside the two quantum wells for a symmetric setup $a = 0$. (b) Efficiency at maximum power in units of the Carnot efficiency η_C within linear response as a function of the two level positions for a symmetric configuration. Panels (c) and (d) show the same as (a) and (b) but for a system with asymmetry $a = 0.5$. This figure was adapted from Ref. [2].

k_BT which explains why the quantum-well heat engine has an efficiency comparable to that of a quantum-dot heat engine with level width k_BT [2].

The proposal [2] has also considered an asymmetric system, $a \neq 0$, where both the power and the efficiency are no longer invariant under an exchange of the two level positions. It is found that power and efficiency are strongly reduced for $E_L < 0$ and $E_R > 0$ if $a > 0$ (for $a < 0$, the roles of E_L and E_R are interchanged). In contrast, for $E_L > 0$ and $E_R < 0$, power and efficiency are even slightly enhanced compared to the symmetric system. Figure 5.3 depicts the power as a function of the asymmetry a and the level position E_L. The maximal power occurs for $a \approx 0.46$ and $E_L \approx 2k_BT$ with $-E_R \gg k_BT$. The resulting power is about 20% larger than for the symmetric setup. At the same time, the efficiency at maximum power is also increased compared to the symmetric systems to $\eta \approx 0.12\eta_C$ (nearly doubled). The maximal efficiency that can be obtained for the asymmetric system is given by $\eta \approx 0.3\eta_C$. However, as for the symmetric setup, this occurs in a regime where the output power is highly suppressed [2].

For realistic device parameters, using $m^* = 0.067m_e$, $T = 300K$, $\Gamma = k_BT$ and $a = 0.5$, this model predicts $P_{max} = 0.18\,\mathrm{Wcm}^{-2}$ for a temperature difference $\Delta T = 1K$ [2]. Hence, the quantum-well heat engine is nearly twice as powerful as a heat engine based on resonant-tunnelling quantum dots [1]. It is noted that materials with higher effective mass yield correspondingly larger output powers. In addition, the quantum-well heat engine offers the advantages of being potentially easier to fabricate. As typical level splittings in quantum wells are in the range of 200-500 meV, narrow quantum wells might also be promising candidates for room-temperature applications though leakage phonon heat currents become

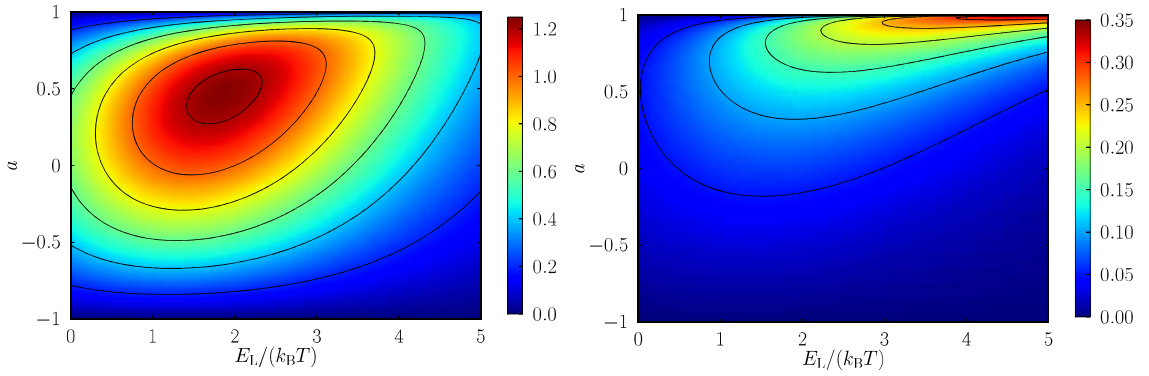

Fig. 5.3 Left panel: maximum power in units of $\frac{\upsilon_2 A\Gamma}{2\hbar}(\frac{k_B\Delta T}{2})^2$ within linear response as a function of the level positions and the asymmetry of couplings. Right panel: efficiency at maximum power in units of the Carnot efficiency η_C within linear response as a function of one level position and the asymmetry of couplings. For both plots, $E_R = -10k_BT$. This figure was adapted from Ref. [2].

of relevance then [2]. Finally, Figure 5.3 shows a good robustness with respect to fluctuations in the device properties [2], compared to to the quantum-dot based similar setup in Ref. [1].

5.2 Device design

Figure 5.4 shows the design used for the Double-Well Energy Harvester (DWEH). It consists of four pairs of split gates (SG), four middle gates (MG), two area gates and one bar gate (BG), which has been fabricated using E-beam lithography. Their functions will be discussed in detail in following sub-sections. There is also the mesa marked by the orange solid lines, four ohmic contacts false-coloured in orange that are connecting the surface with the double 2DEGs below, and gates featured in grey solid lines. Their fabrication will be discussed in detail in the next section.

5.2.1 The split and middle gates

To make measurements of tunnelling between the parallel 2DEGs, it is essential to make independent contacts to the two 2D layers simultaneously. Smoliner *et al.* used a combination of shallow ohmic contacts and etching to make the first direct measurements of 2D-2D tunnelling [150, 151]. Later Eisenstein *et al.* developed the technique of selective depletion [152] by Schottky gates evaporated on the front and back surface of a chip to form independent contacts in higher quality DQW samples. Split-gate devices with an additional middle gate were fabricated on GaAs/AlGaAs DQW heterostructure [153–155]. Crucially,

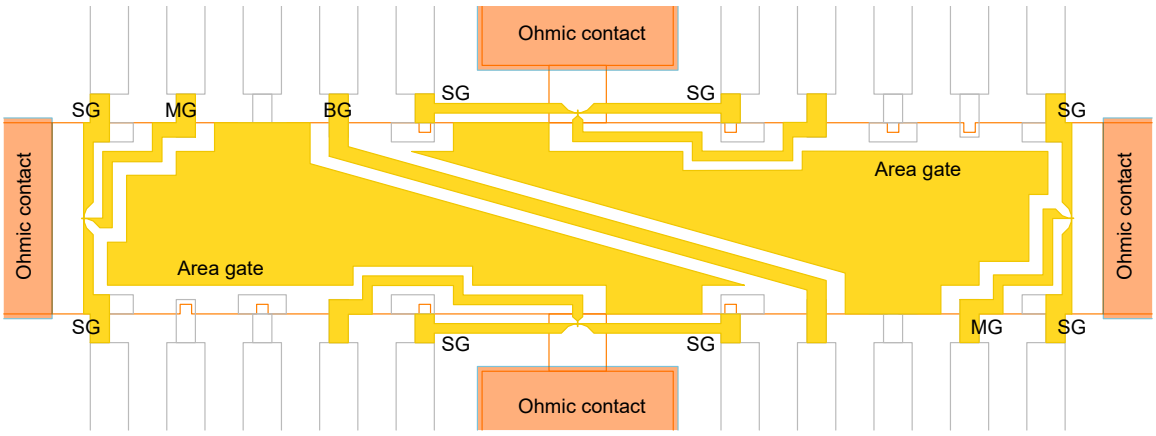

Fig. 5.4 The design used for the Double-Well Energy Harvester (DWEH). The gates are false coloured in yellow, and the ohmic contacts in orange. The orange solid lines depict the mesa, and the gray solid lines depict the gate from optical lithography, which will be discussed in detail in the fabrication section (Sec. 5.3).

the mid-gate/split-gate combination can tune the device into a configuration comprising a pair of vertically aligned quasi-1D channels, or a single quasi-1D channel in either the upper or lower 2DEG. This gives access to each quantum well separately.

Thomas *et al.* measured the two-terminal conductance $G = dI/dV$ of two vertical parallel wires using conventional techniques in 1999 [153], as shown in Fig. 5.5. Figure 5.5 (a) depicts the conductance traces, $G(V_{sg})$, of the 2×1D device at 1.2 K. The conductance is measured as a function of the split-gate voltage, V_{sg}, and V_{mid} is stepped from 0.16 V on the left to –1.0 V on the right, in intervals of 40 mV, as the middle gate voltage V_{mid} was changed from 0.16 V to –1.0 V in 40 mV steps. Three distinct regions are observed. The triangular regions at the bottom left and right labelled '*u*' and '*l*' arise from a single quasi-1D channel in either the upper or lower layer, respectively, with the other channel pinched off. Both channels exhibit strong ballistic conductance plateaux quantised in steps of $2e^2/h$, in addition to structure at $0.7(2e^2/h)$. In the central region, two quasi-1D wires are present and conduct in parallel, with a total conductance equal to the sum of the conductances of each wire. This is achieved by changing voltages on split-gate and middle-gate. The split-gate voltage V_{sg} defines both the *u* and *l* wires; however, as V_{sg} becomes more negative, the

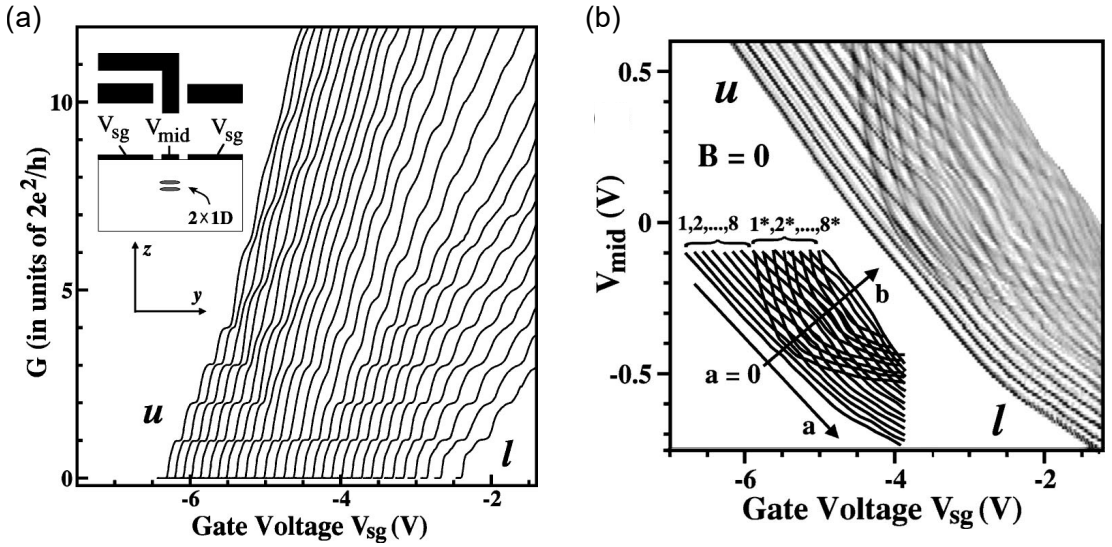

Fig. 5.5 Conductance characteristics of a vertically-aligned, double-quantum-wire device. V_{sg} is swept for fixed V_{mid}, where V_{mid} is incremented between traces from 0.16 V to –1 V (left-to-right), in 40 mV steps. The inset shows both a plan and cross-section schematic of the device, where SG and MG stand for split gate and middle gate, respectively. (b) Transconductance of data from (a), as a function of V_{mid} and V_{sg}. Black (white) regions represent high (low) transconductance, i.e. risers between plateaux (the plateaux). The black lines are re-plotted in the inset, and are identified as bonding and anti-bonding (*) states of the coupled system. Both (a) and (b) are adapted from Ref. [153].

subbands in the l wire are depopulated first. The middle-gate voltage v_{mid} has the opposite effect; as it is made more negative the u wire is depopulated first. Therefore, by varying V_{sg} and V_{mid}, the fraction of the current passing through the u and l wires can be tuned. It is more instructive to view the transconductance of the data in Figure 5.5(a), shown in Figure 5.5(b). The black (white) regions represent high (low) transconductance, i.e. risers between plateaux (the plateaux). The black lines therefore occur when the 1D subband edges cross the chemical potential. Two sets of lines are evident; one set of lines is reasonably straight, the other is curved. These are plotted in the inset, and are identified as the bonding $(1,2,...,8)$ and anti-bonding $(1^*,2^*,...,8^*)$ states of the coupled-wire system. These states anti-cross as a function of V_{mid} and V_{sg}. A fuller explanation of these measurements is given by Thomas *et al.* [153].

Figure 5.6 shows the scaled image of the design for the split-gate and mid-gate combination in this device. The split gate was 0.5 μm long and 1.1 μm wide, and the middle gate is 0.5 μm wide. The middle gate is positioned at the centre of the split gate, and each side is 0.3 μm apart from the split gate. All four groups of SG and MG are identical in terms of their lengths, widths and their distances from each other.

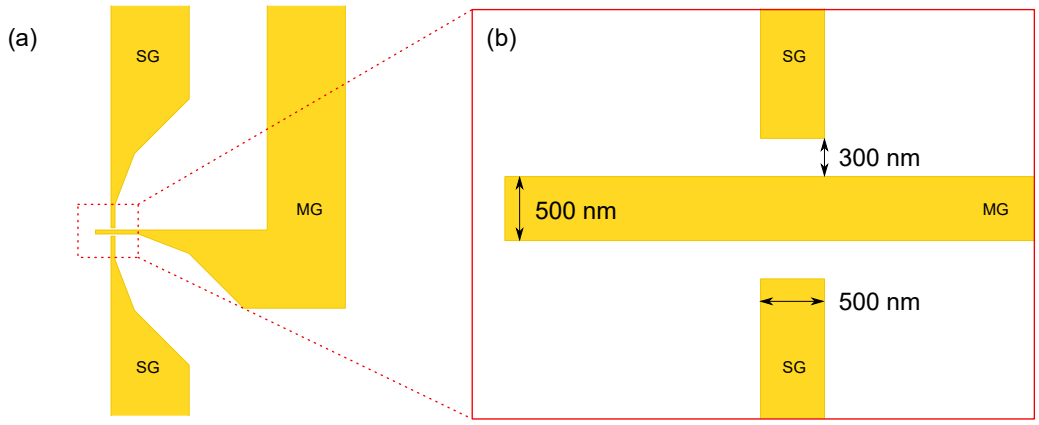

Fig. 5.6 The split gate design.

5.2.2 The bar gate and the area gates

Both the bar gate and the area gates are made to change the carrier density in the upper 2DEG. The bar gate is designed to cross the whole mesa. A negative voltage is applied to it to deplete the electrons below the gate in the upper 2DEG completely, so as to have two separate regions of 2DEGs in the upper layer. This is because it requires three layers of 2DEGs to experimentally realise such a system as in Figure 5.1. Given that we only have a double-quantum-well GaAlAs/GaAs HEMT wafer, it is therefore necessary to divide

the upper quantum well into two independent regions to act as two cold reservoirs. The lower 2DEG can then act as a hot cavity heated by different AC currents applied from an independent lock-in amplifier. The electrons that meet the tunnelling conditions between the two wells, can then be tuned to tunnel from one cold reservoir in the upper well into the hot reservoir of the lower well, or vice versa. This can be achieved by changing carrier densities in the two separate 2DEGs in the upper well electrically via varying negative voltages applied on their respective area gates. Eventually, we aim to achieve the tunnelling as shown in Figure 5.7, harvesting energy from the lower quantum well to the upper 2DEG.

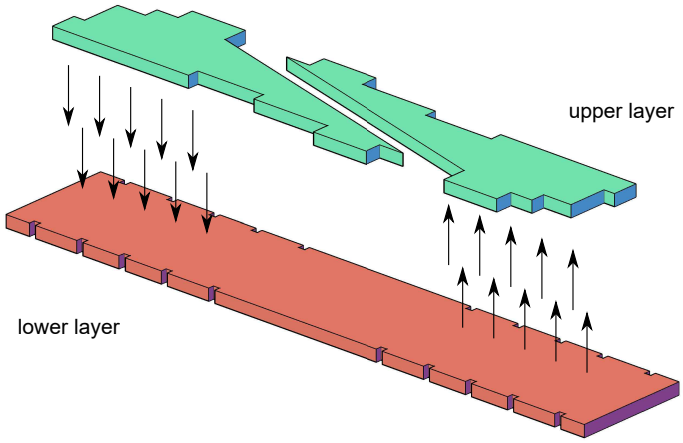

Fig. 5.7 The possible tunnelling between double wells that is aimed to be achieved via changing their carrier densities through the area gates.

5.3 Fabrication

QWEH devices were fabricated using standard semiconductor process techniques, including optical and electron-beam lithography. Appendix A.2 contains the details of the wafer (W0187) used to make the devices, which was grown by the MBE team at the SP group of the Cavendish Laboratory. The same wafer of W0187 was also used in the work of Smith *et al.* [92], where the mobility and carrier concentration of both layers measured simultaneously were $\mu \approx 3.0 \times 10^6\,\mathrm{cm^2V^{-1}s^{-1}}$ and $n \approx 2.4 \times 10^{11}\,\mathrm{cm^{-2}}$ respectively at 1.5 K. The carrier density of the upper and lower layers of W0187 were measured to be $n_u \approx 1.3 \times 10^{11}\,\mathrm{cm^{-2}}$ and $n_l \approx 1.1 \times 10^{11}\,\mathrm{cm^{-2}}$ respectively. It was not possible to measure the individual mobility of each layer.

5.3.1 Etching

To begin with, the wafer is cleaved into an appropriate size of $10 \times 10\,\mathrm{mm}^2$ for processing. This piece of wafer will be referred as the 'chip' in the following description. The first step is to electrically isolate a region of the 2DEG, in the shape of a Hall bar. To this end this chip is coated with a negative photoresist (Shipley 1813), and briefly exposed to UV light through a mask patterned as a Hall bar. The chip is then developed to remove the photoresist from exposed areas. A sulphuric acid solution (1:8:111 H_2SO_4:H_2O_2:H_2O) is used to etch the surface of the wafer, leaving a raised 'mesa'. The depth of mesa is then measured using a DEKTAK surface profiler, to check whether enough material has been removed. In a HEMT wafer, it is only necessary to etch beyond the dopant layer, but, for reliable processing, it is generally safest to etch past the 2DEG layer. For a DQW wafer, it is necessary to etch beyond the second doping layer ($> 620\,\mathrm{nm}$ for W0187). After etching, the remaining resist is removed using acetone. In this work, mask patterns CAV-SP-TLL were used, for which the Hall bar is $1700\,\mu\mathrm{m}$ long and $80\,\mu\mathrm{m}$ wide. Figure 5.8(a) shows the device after the mesa etching process.

5.3.2 Ohmic contacts

The next step is to fabricate the ohmic contacts, which are formed by depositing an alloy of AuGeNi on top of the mesa, and thermally annealing. It is necessary for the metal to diffuse beyond the GaAs/AlGaAs interface, where the 2DEG forms, to make good electrical contacts. The pattern for ohmic contacts is created using a standard process. The chip is coated with a photoresist of Shipley 1805, exposed to UV light through the ohmic-contact mask pattern, and the chip is developed. The chip is then metallised with AuGeNi in a thermal evaporator, under a high vacuum ($< 1 \times 10^{-6}\,\mathrm{mbar}$). Unwanted metal and resist are removed in the lift-off process, which is aided by having soaked the chip in chlorobenzene for 180 s prior to developing, to produce an undercut profile in the resist. The chip is then annealed in forming gas (95%N_2 5% H_2), to prevent oxidation of the ohmic contacts. The DQW wafers are annealed at $450\,^{\circ}\mathrm{C}$, to ensure that the metal contacts both quantum wells below. Figure 5.8 (b) depicts the device after the ohmic contact process.

5.3.3 Optical gates

Schottky surface gates are then patterned using optical lithography, in the same way as the ohmic contacts. The chip is coated with Shipley 1813 photoresist, exposed to UV light through the mask of CAV-SP-TLL, and developed. Prior to developing, a chlorobenzene

soak is used to produce an undercut profile in the resist. The gates are metallised in a thermal evaporator at high vacuum (2×10^{-7}mbar), and 20/150 nm Ti/Au is deposited (Ti is used to improve adhesion to the surface of the wafer), A Rotatilt was used in the evaporation chamber to ensure continuity over the mesa edge, where the chips are held at a small angle (about 30°) and continuously rotated during the evaporation. Following metallisation, the unwanted metal and resist are removed in a lift-off process, by soaking the chip in acetone for 10 minutes. Figure 5.8 (c) depicts the device after the processing of the optical gates.

5.3.4 E-beam gates

In order to pattern gate feature $< 1\,\mu$m, such as split gates, electron-electron lithography is required, Firstly, a layer of 100K PMMA is spun onto the chip, and the chip is baked at 115 °C for 2 minutes. In order to increase the thickness of the gates that can be deposited, a thicker layer of PMMA is required. However, this increases the minimum feature size that can be written using the electron beam. To overcome this problem, a second, thinner layer of 950K PMMA is deposited on top of the first (thick) layer, to preserve the resolution that can be achieved. The required gate pattern is then written in the PMMAs using the electron

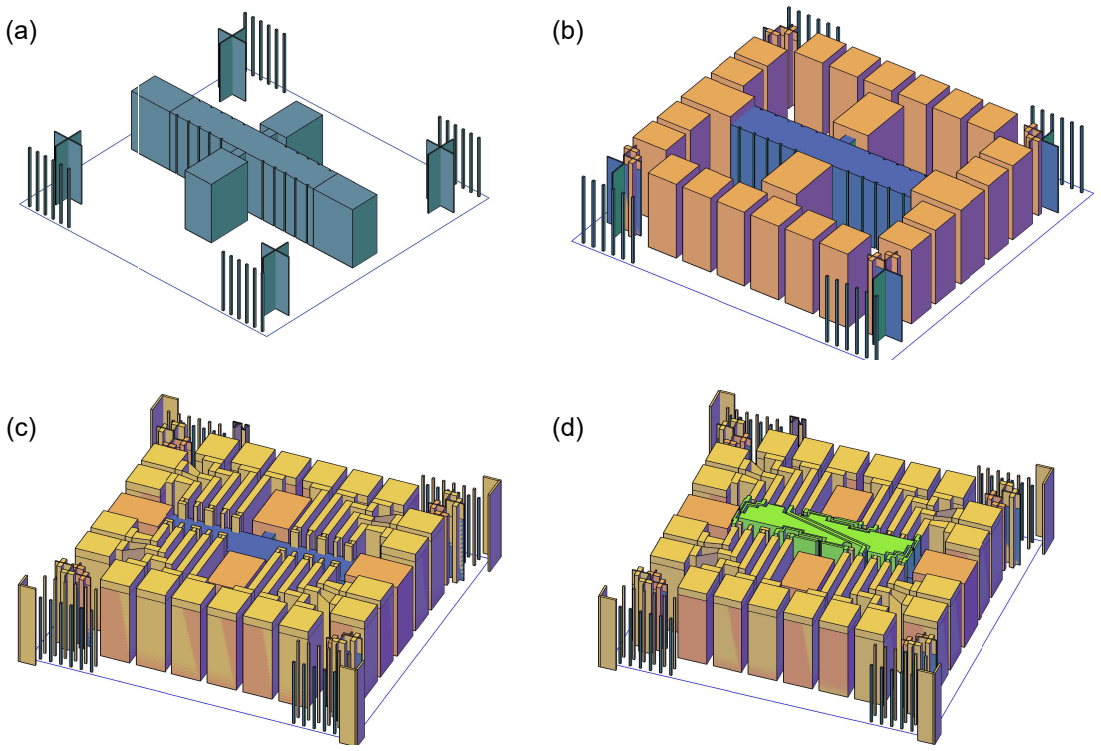

Fig. 5.8 The 3D image of the device after completing the process of (a) Mesa (in blue); (b) Ohmic contacts (in orange); (c) Optical gates (in yellow); (d) E-beam gates (in green).

beam, after which the pattern is developed using a standard developer [1:3 propanol: methyl isobutyl ketone (MIBK)]. The metallisation process is the same as that described for the optical gates, although a longer lift-off time (> 2 hours) is necessary. Typically, 10/60 nm Ti/Au is metallised for a standard set of split gates, and these gates must be continuous with the optically-defined gates. Figure 5.8 (d) shows the device after E-beam processing.

5.3.5 Bonding

In the final stage of processing, devices are mounted in non-magnetic chip carriers. Since several devices are fabricated on one chip, the chips are first cleaved into the individual devices, which are then glued into chip carriers using GE varnish. A gold-ball thermosonic bonder is used to connect gate and ohmic pads on the device to the chip package.

5.4 Measurement set-ups

The data presented in this thesis were primarily obtained using a two-terminal measurement circuit, as shown in Fig. 5.9. An AC excitation voltage of V_{ac} is output from a lock-in amplifier, SR830 DSP, and passes through a transformer first, and then a potential divider of $10^2\Omega/10^6\Omega$, to provide a constant voltage of $V = 100\,\mu$V across the sample (SG(2,4)). After the sample, the current I is then measured using the lock-in amplifier, which detects the signal at a given reference frequency (typically 77 Hz). This signal is passed to a measurement computer over a GPIB interface. Since V is constant, I is proportional to the conductance of the sample (plus a series-resistance contribution). The circuit can be calibrated by replacing the sample with a 10 kΩ resistor. The measured signal from the lock-in amplifier can then be scaled using this known resistance such that the signal corresponds to the conductance of the resistor/sample. The negative voltages are applied from NiQaq-7298 on the gates to vary the carrier density in the 2DEGs below and define the device.

Three methods have been used to reduce the noise in the circuit, which is very important for low-temperature measurements. Firstly, phase-sensitive detection goes a long way towards minimising the noise in the measured signal, by detecting a signal at a specific frequency. The signal frequency is chosen to be away from the mains frequency of 50 Hz and higher harmonics. One of the most common problems is 50 Hz (and higher harmonics) noise, arising from ground loops (multiple grounds in the circuit). These must be removed by ensuring that there is only one common ground for the circuit. Some precautions that can be taken include ensuring a common ground for all the measurement instruments, and placing a 1 : 1 transformer on the output of the signal generator. This is the second method. Additionally,

the 10 T cryostat system (the 1K pot system shown in Figure B.1 in Appendix B) used in this work was located inside a screened room, acting as Faraday cage to avoid RF sources of electron heating.

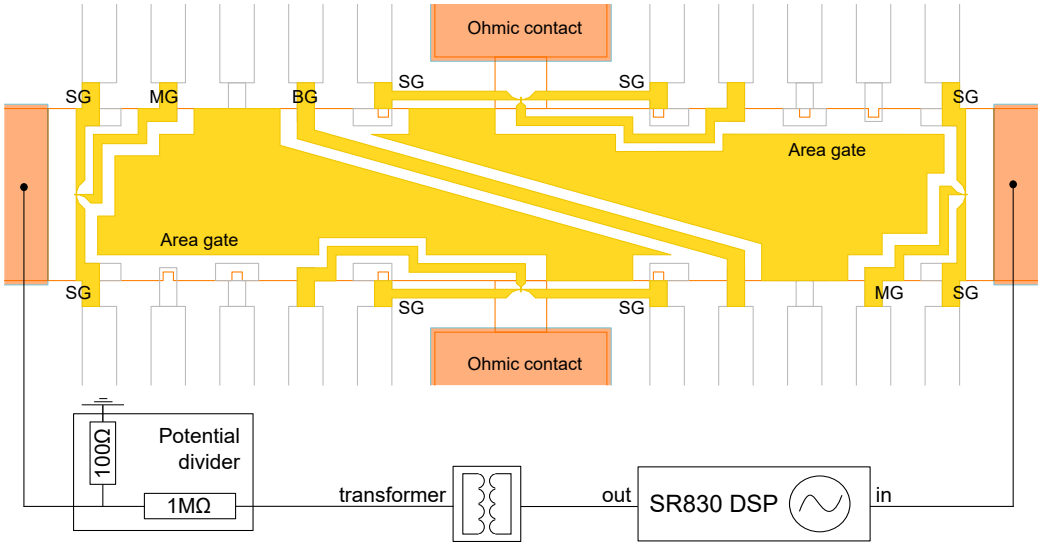

Fig. 5.9 The electrical circuit used for two-terminal constant-voltage measurements, with the device in central where the gates are in yellow and the ohmic contacts in orange. An AC excitation voltage of 1.0 V is applied from a SR 830 DSP lock-in amplifier, which passes through a transformer first to decrease the noise, and then is divided by a potential divider of $10^2/10^6$, and finally this is applied to the device. The current is measured via the lock-in amplifier as a function of gate voltage at a frequency of 77 Hz.

5.5 Measurements and analysis

The first task of the measurements is to tune the device via changing the negative voltages applied on the gates as well as to ensure access to the 2DEGs.

As discussed in Section 5.2.2, it is necessary to have two independent regions of 2DEG in the upper quantum well while not influencing the 2DEG in the lower well. Figure 5.10 (a) shows the current through both 2DEGs as a function of the bar-gate voltage (V_{gate5}). The first drop in current (marked by U) occurs when the upper layer is depleted of electrons in the region below the bar gate. As V_{gate5} is made more negative, a second drop in current to $I = 0$ occurs (marked by L), which indicates the depletion of the lower layer. When $V_{gate5} = 0$ the current in both layers is measured, and for $V_{gate5} \approx -0.5V$ (marked by the arrow), the 2DEG in the top layer has been separated and the lower-layer current alone is measured. Therefore,

the bar gate has been applied a voltage of –0.5V during our measurements. The conductance equals the current divided by the AC excitation voltage of 100 μV.

Figure 5.10(b) shows the total conductance G_0 ($V_{bar} = 0$ V) of sample SG(2,4), as a function of the split-gate voltages ($V_{gate}16–18$). For each trace V_{mid} is fixed, and between traces V_{mid} is stepped by –30 mV, from 0.40 V on the left to –0.50 V on the right. Three distinct regions are observed. The triangular regions at the bottom left and right labelled 'U' and 'L' arise from a single quasi-1D channel in either the upper or lower layer, respectively, with the other channel pinched off. Both channels exhibit strong ballistic conductance plateaux quantised in steps of $2e^2/h$, in addition to structure at $0.7(2e^2/h)$. In the central region, two quasi-1D wires are present and conduct in parallel with a total conductance equal to the sum of the conductance of each wire. Based on Figure 5.10 (b), we can decide voltages applied on this group of middle gate and split gates, so as to form independent access to either the upper or the lower layers respectively.

After tuning the device, the next task is to measure resonant tunnelling between two wells. Following on the discussion in Section 2.4.1 in Chapter 2, the resonant tunnelling can only occur when the subband energy as well as the k-vector are made equal in both layers, which means an equal carrier density in both wells in our measurement. The differential tunnelling conductance was therefore measured as a function of the area gate voltage controlling the

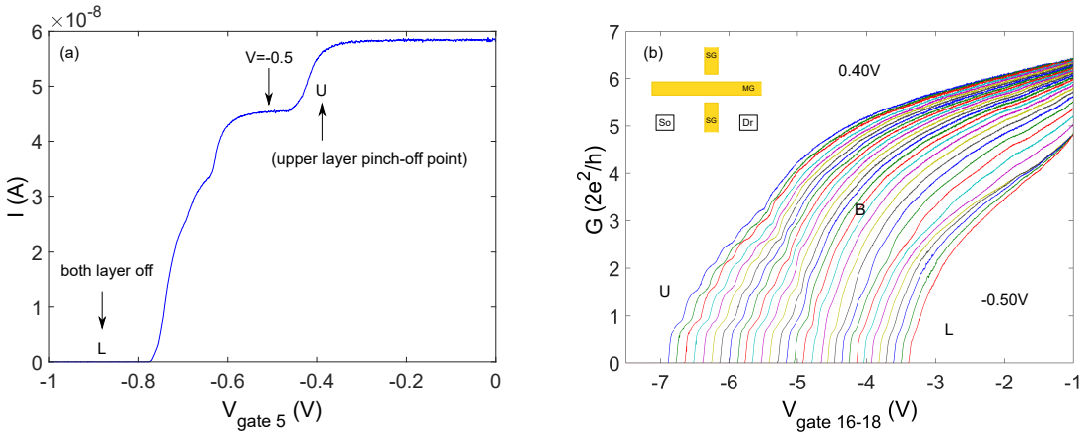

Fig. 5.10 (a) The current as a function of bar-gate voltage, V_{gate5}. U and L mark the depletion of the upper and lower electron layers respectively. The arrow indicates V = –0.50 V, the typical voltage applied to measure lower-layer conductance. (b) G as a function of split-gate voltage, $V_{gate}16–18$. V_{mid} is stepped from 0.40 V on the left to –0.50 V on the right, in –30 mV intervals (T = 1.5 K,B = 0 T). The conductance is quantised in units of $2e^2/h$. The upper (lower) wire is occupied on the left (right) of the $V_{gate}16–18$, marked by U(L). In the middle region (marked B), conductance is quantised in $4e^2/h$ multiples, indicating transport through the two wires in parallel. These measurements were performed at 1.5K.

carrier density in the upper layer, when the carrier density in the lower 2DEG is fixed, as shown in Figure 5.11. Unfortunately the tunnelling conductance, $G \approx 0.002(2e^2/h)$, is so low that it is not enough for realising the QWEH device. This is because the barrier width is 30 nm, between the two quantum wells, too large to have the tunnelling. Turner *et al.* see the resonant tunnelling between two quantum wells with a distance of around 10 nm.

Figure 5.11(b) shows that differential conductance G between two wells as a function of the area-gate voltage, changing the carrier density of the upper layer, while applying an in-plane magnetic field. For each traces the magnetic field B is fixed, and between traces B is stepped by 0.25 T, from 0 T on the bottom to 3.75 T on the top. However no resonant tunnelling peaks appear while applying an in-plane magnetic field. It has increased the conductance by 1000 times, which looks more likely to be a leakage between two quantum wells possibly. This can happen first through the ohmic contacts, when the gates have not been defined well. This type of leakage often appeared in our measurements when the bar gate has not been used. Secondly, it could be leakage from the sample holder, which has been in poor conditions and had to be fixed several times.

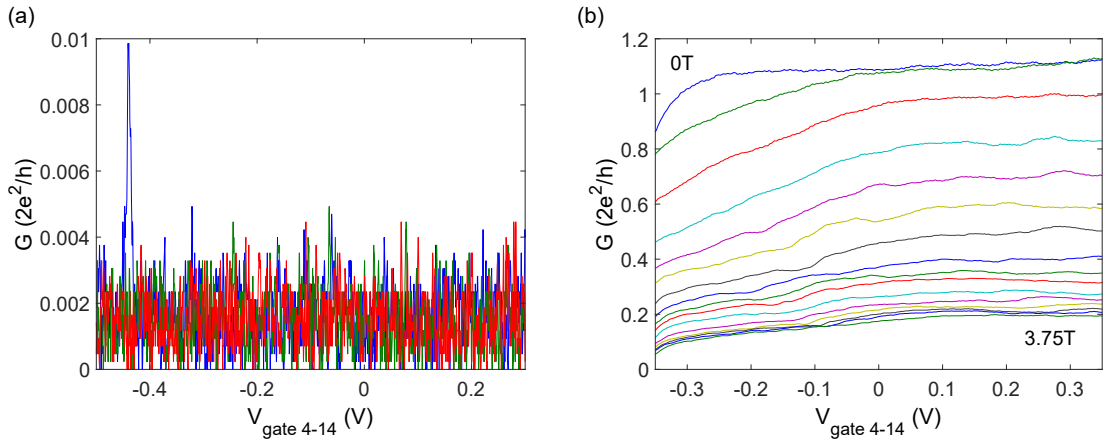

Fig. 5.11 (a) shows the tunnelling conductance from the upper well to the lower one as a function of area gate voltages, V_{4-14}, at $T = 1.5$ K, $B = 0$ T. The multiple traces here show the same sweep repeatedly measured. (b) shows the tunnelling conductance between double wells as a function of area-gate voltage, V_{4-14}, in an in-plane magnetic field changed from $0T$ to $3.75T$ in a step of $0.25T$, at $T = 1.5K$. For each trace, the magnetic field is fixed. There appears no resonant peaks in tunnelling, but the conductance is much larger than that in Panel (a). This is actually caused by a leakage appeared during the measurements.

5.6 Conclusion

In this chapter, we have introduced the theoretical proposal, from Sothmann *et al.* [2], of building an energy harvester with two resonant-tunnelling quantum wells. This can scale up the quantum-dot energy harvester, experimentally demonstrated in Chapter 3, and increase its working temperature as well as the generated thermal power. The design and fabrication processes have been presented in detail. Measurements has proven that a split-gate and mid-gate combination can successfully give us access to each individual layers. Unfortunately, the tunnelling between two quantum wells has failed due to the wide barrier between two wells and the current leakage between two wells from the ohmic contacts or the sample holder. Resonant tunnelling between two quantum wells can be improved by choosing a double-quantum-well wafer with narrow barrier width, such as 10 nm as used in the work of Turner *et al.* [95].

Chapter 6

Conclusion

To conclude, in this thesis, I first introduced the background semiconductor physics required for carrying out our research. I then presented the work that demonstrates, both theoretically and experimentally, an energy harvester built from two resonant-tunnelling quantum dots. A device, proposed by Jordan *et al.* [1], harvests energy from an area of $90\,\mu\mathrm{m}^2$ of a two-dimensional electron gas (2DEG), using the energy-selective transport of electrons through a pair of quantum dots. It has proven to be an effective technique for harvesting energy at the micro/nano scales. Our energy harvester can generate a power of 0.13 fW in an estimated efficiency with a lower bound around $0.1\,\eta_{\mathrm{C}}$. Our theoretical model (not affected by limitations of the Wiedemann-Franz law) suggests the actual efficiency to be about $0.5\,\eta_{\mathrm{C}}$, (here η_{C} is Carnot efficiency, given by $\eta_{\mathrm{C}} = 1 - T_R/T_C$.). Experimental observations of thermal power, voltage and efficiency at different values of I_{Heat} and R_{Load} have also been reproduced by this model. There are small quantitative differences between experimental results and theoretical modelling in terms of parameters, such as electrical temperatures and energy level difference. This may be explained by asymmetric barriers, accidental degeneracies or the broadened lifetime width of the quantum dots, as well as charging effects in the non-linear regime. Also, the oscillation brought with the AC heating and AC measurements can increase thermal broadening in the cavity, and therefore cause inaccuracy in the measurement results. Overall, this proof-of-principle experiment demonstrates the basic soundness of the theory of mesoscopic energy harvesting with energy-filtering techniques at the quantum level, realizing a heat engine.

Chapter 4 investigated the thermometry of such a quantum-dot energy harvester. This part of the thesis describes the characterisation and performance of a non-invasive single-electron thermometer, and extracted the electrical temperatures via three methods as below. First, we introduced to extract the electrical temperatures through fitting the differential conductance

peaks to theoretical models. The advantage of this method is that the quantum dot can directly serve as a thermometer. The disadvantage is that the excitation voltage, applied to trigger the currents through quantum dots, will unavoidably heat the device. In addition, extracting the electron temperature from the transport measurements described above necessities tuning the dot so that the tunnelling rates to the source and drain reservoirs are equal. If the barriers are unequal, the lifetime broadening of single-particle states in the dot will be determined by the more transparent barrier. This limits the resolution of this thermometry method to the lifetime broadening of the dot states. Then we introduce the qpc thermometry, to extract temperatures via monitoring the changes in electrostatic potential of 1D channel close to the quantum dot. It is easier to set up this measurement, and the signal through a qpc is usually several times greater than the current through a quantum dot, which means that the qpc thermometer is much more sensitive than the quantum-dot thermometer for a similar experimental set up. The third method is to use the Mott relation as an insight into the thermometry of our QDEH device. It is supposed to have higher accuracy compared to previous thermometers, because of the same sets of circuits and data used as the thermal power measurements. We were unable to make this work unfortunately.

Chapter 5 presented our attempt to experimentally demonstrate the theoretical proposal of building an energy harvester with two resonant-tunnelling quantum wells by Sothmann *et al.* [2]. This can scale up the quantum-dot energy harvester of Chapter 3, increase its working temperature and the generated thermal power. The design and fabrication process have also been presented in detail. Measurements confirmed that a split-gate and mid-gate combination can successfully give us access to each individual layer. Unfortunately, the tunnelling between two quantum wells was too weak, due to the wide barrier between two wells. This work can be improved by fabricating such an energy-harvester device with a double-quantum-well wafer with a narrow barrier width.

Both devices require a good thermal contact to relative 2DEGs. The electron temperatures are key to studying their power and efficiency, and therefore it is important to study the thermometry of these measurements. Hopefully further study of energy harvesters will result in a more rigorous understanding of their limitations, improvements in performance, and perhaps new insights into the physics of heat in low-dimensional electronic systems.

There are several possible improvements for future work. First, we can improve the power and efficiency by optimising the resonance width as well as the symmetry of the quantum dots in Chapter 3. Second, the quantum-dot energy harvester can be realised with smaller dots or molecules, whose large level spacing allows the system to operate at higher temperature [1, 142, 143]. Third, DC heating and measurement techniques can be used to avoid unnecessary oscillations of voltages and temperatures in the quantum-dot energy

harvester device. Finally, repeat the measurements of Chapter 5, with a double-well wafer whose barrier width between two wells is around 10 nm, to experimentally realise a resonant-tunnelling quantum-well energy harvester [2], which may increase the maximum power of the quantum-dot energy harvester [1].

References

[1] Andrew N. Jordan, Björn Sothmann, Rafael Sánchez, and Markus Büttiker. Powerful and efficient energy harvester with resonant-tunneling quantum dots. *Phys. Rev. B*, 87(7):075312, February 2013. doi: 10.1103/PhysRevB.87.075312. URL http://link.aps.org/doi/10.1103/PhysRevB.87.075312.

[2] Björn Sothmann, Rafael Sánchez, Andrew N. Jordan, and Markus Büttiker. Powerful energy harvester based on resonant-tunneling quantum wells. *New J. Phys.*, 15(9): 095021, September 2013. ISSN 1367-2630. doi: 10.1088/1367-2630/15/9/095021. URL http://iopscience.iop.org/1367-2630/15/9/095021.

[3] Bruce E White Jr. Energy-harvesting devices: Beyond the battery. *Nature nanotechnology*, 3(2):71, 2008.

[4] Ali Shakouri. Recent developments in semiconductor thermoelectric physics and materials. *Annual review of materials research*, 41:399–431, 2011.

[5] Giuliano Benenti, Giulio Casati, Keiji Saito, and Robert S Whitney. Fundamental aspects of steady-state conversion of heat to work at the nanoscale. *Physics Reports*, 694:1–124, 2017.

[6] David Michael Rowe. Thermoelectric waste heat recovery as a renewable energy source. *International Journal of Innovations in Energy Systems and Power*, 1(1): 13–23, 2006.

[7] L. D. Hicks and M. S. Dresselhaus. Effect of quantum-well structures on the thermoelectric figure of merit. *Phys. Rev. B*, 47(19):12727–12731, May 1993. doi: 10.1103/PhysRevB.47.12727. URL http://link.aps.org/doi/10.1103/PhysRevB.47.12727.

[8] L. D. Hicks and M. S. Dresselhaus. Thermoelectric figure of merit of a one-dimensional conductor. *Phys. Rev. B*, 47(24):16631–16634, June 1993. doi: 10.1103/PhysRevB.47.16631. URL http://link.aps.org/doi/10.1103/PhysRevB.47.16631.

[9] G D Mahan and J O Sofo. The Best Thermoelectric. *Proc. Natl. Acad. Sci. USA*, 93 (15):7436–7439, July 1996. ISSN 0027-8424, 1091-6490. URL http://www.pnas.org/content/93/15/7436.

[10] C. W. J. Beenakker and A. A. M. Staring. Theory of the thermopower of a quantum dot. *Phys. Rev. B*, 46(15):9667–9676, October 1992. doi: 10.1103/PhysRevB.46.9667. URL http://link.aps.org/doi/10.1103/PhysRevB.46.9667.

[11] Natthapon Nakpathomkun, H. Q. Xu, and Heiner Linke. Thermoelectric efficiency at maximum power in low-dimensional systems. *Phys. Rev. B*, 82(23):235428, December 2010. doi: 10.1103/PhysRevB.82.235428. URL http://link.aps.org/doi/10.1103/PhysRevB.82.235428.

[12] T. E. Humphrey, R. Newbury, R. P. Taylor, and H. Linke. Reversible Quantum Brownian Heat Engines for Electrons. *Phys. Rev. Lett.*, 89(11):116801, 2002. doi: 10.1103/PhysRevLett.89.116801. URL http://link.aps.org/doi/10.1103/PhysRevLett.89.116801.

[13] M. Esposito, K. Lindenberg, and C. Van den Broeck. Thermoelectric efficiency at maximum power in a quantum dot. *Europhys. Lett.*, 85(6):60010, March 2009. ISSN 0295-5075, 1286-4854. doi: 10.1209/0295-5075/85/60010. URL http://iopscience.iop.org/0295-5075/85/6/60010.

[14] A. A. M Staring, L. W Molenkamp, B. W Alphenaar, H. van Houten, O. J. A Buyk, M. A. A Mabesoone, C. W. J Beenakker, and C. T Foxon. Coulomb-Blockade Oscillations in the Thermopower of a Quantum Dot. *Europhysics Letters (EPL)*, 22: 57–62, April 1993. ISSN 0295-5075, 1286-4854. doi: 10.1209/0295-5075/22/1/011. URL http://iopscience.iop.org/0295-5075/22/1/011.

[15] A. S. Dzurak, C. G. Smith, C. H. W. Barnes, M. Pepper, L. Martín-Moreno, C. T. Liang, D. A. Ritchie, and G. A. C. Jones. Thermoelectric signature of the excitation spectrum of a quantum dot. *Phys. Rev. B*, 55(16):R10197–R10200, April 1997. doi: 10.1103/PhysRevB.55.R10197. URL http://link.aps.org/doi/10.1103/PhysRevB.55.R10197.

[16] S. F. Godijn, S. Möller, H. Buhmann, L. W. Molenkamp, and S. A. van Langen. Thermopower of a Chaotic Quantum Dot. *Phys. Rev. Lett.*, 82(14):2927–2930, April 1999. doi: 10.1103/PhysRevLett.82.2927. URL http://link.aps.org/doi/10.1103/PhysRevLett.82.2927.

[17] Joshua P. Small, Kerstin M. Perez, and Philip Kim. Modulation of Thermoelectric Power of Individual Carbon Nanotubes. *Phys. Rev. Lett.*, 91(25):256801, December 2003. doi: 10.1103/PhysRevLett.91.256801. URL http://link.aps.org/doi/10.1103/PhysRevLett.91.256801.

[18] M. C. Llaguno, J. E. Fischer, A. T. Johnson, and J. Hone. Observation of Thermopower Oscillations in the Coulomb Blockade Regime in a Semiconducting Carbon Nanotube. *Nano Lett.*, 4(1):45–49, 2003. ISSN 1530-6984. doi: 10.1021/nl0348488. URL http://dx.doi.org/10.1021/nl0348488.

[19] R. Scheibner, H. Buhmann, D. Reuter, M. N. Kiselev, and L. W. Molenkamp. Thermopower of a Kondo Spin-Correlated Quantum Dot. *Phys. Rev. Lett.*, 95 (17):176602, October 2005. doi: 10.1103/PhysRevLett.95.176602. URL http://link.aps.org/doi/10.1103/PhysRevLett.95.176602.

[20] R. Scheibner, E. G. Novik, T. Borzenko, M. König, D. Reuter, A. D. Wieck, H. Buhmann, and L. W. Molenkamp. Sequential and cotunneling behavior in the temperature-dependent thermopower of few-electron quantum dots. *Phys.*

Rev. B, 75(4):041301, January 2007. doi: 10.1103/PhysRevB.75.041301. URL http://link.aps.org/doi/10.1103/PhysRevB.75.041301.

[21] S Fahlvik Svensson, A I Persson, E A Hoffmann, N Nakpathomkun, H A Nilsson, H Q Xu, L Samuelson, and H Linke. Lineshape of the thermopower of quantum dots. *New J. Phys.*, 14(3):033041, March 2012. ISSN 1367-2630. doi: 10.1088/1367-2630/14/3/033041. URL http://iopscience.iop.org/1367-2630/14/3/033041.

[22] S. Fahlvik Svensson, E. A. Hoffmann, N. Nakpathomkun, P. M. Wu, H. Q. Xu, H. A. Nilsson, D. Sánchez, V. Kashcheyevs, and H. Linke. Nonlinear thermovoltage and thermocurrent in quantum dots. *New J. Phys.*, 15(10):105011, October 2013. ISSN 1367-2630. doi: 10.1088/1367-2630/15/10/105011. URL http://iopscience.iop.org/1367-2630/15/10/105011.

[23] H. Thierschmann, M. Henke, J. Knorr, L. Maier, C. Heyn, W. Hansen, H. Buhmann, and L. W. Molenkamp. Diffusion thermopower of a serial double quantum dot. *New J. Phys.*, 15(12):123010, December 2013. ISSN 1367-2630. doi: 10.1088/1367-2630/15/12/123010. URL http://iopscience.iop.org/1367-2630/15/12/123010.

[24] Martin Josefsson, Artis Svilans, Adam M. Burke, Eric A. Hoffmann, Sofia Fahlvik, Claes Thelander, Martin Leijnse, and Heiner Linke. A quantum-dot heat engine operating close to the thermodynamic efficiency limits. *Nat. Nanotechnol.*, 13(10): 920–924, Jul 2018. ISSN 1748-3395. doi: 10.1038/s41565-018-0200-5.

[25] Björn Sothmann, Rafael Sánchez, and Andrew N. Jordan. Thermoelectric energy harvesting with quantum dots. *Nanotechnology*, 26(3):032001, January 2015. ISSN 0957-4484. doi: 10.1088/0957-4484/26/3/032001. URL http://iopscience.iop.org/0957-4484/26/3/032001.

[26] O. Entin-Wohlman, Y. Imry, and A. Aharony. Three-terminal thermoelectric transport through a molecular junction. *Phys. Rev. B*, 82(11):115314, 2010. doi: 10.1103/PhysRevB.82.115314. URL http://link.aps.org/doi/10.1103/PhysRevB.82.115314.

[27] Rafael Sánchez and Markus Büttiker. Optimal energy quanta to current conversion. *Phys. Rev. B*, 83(8):085428, February 2011. doi: 10.1103/PhysRevB.83.085428. URL http://link.aps.org/doi/10.1103/PhysRevB.83.085428.

[28] Björn Sothmann, Rafael Sánchez, Andrew N. Jordan, and Markus Büttiker. Rectification of thermal fluctuations in a chaotic cavity heat engine. *Phys. Rev. B*, 85(20): 205301, May 2012. doi: 10.1103/PhysRevB.85.205301. URL http://link.aps.org/doi/10.1103/PhysRevB.85.205301.

[29] Björn Sothmann and Markus Büttiker. Magnon-driven quantum-dot heat engine. *Europhys. Lett.*, 99(2):27001, July 2012. ISSN 0295-5075, 1286-4854. doi: 10.1209/0295-5075/99/27001. URL http://iopscience.iop.org/0295-5075/99/2/27001.

[30] Tomi Ruokola and Teemu Ojanen. Theory of single-electron heat engines coupled to electromagnetic environments. *Phys. Rev. B*, 86(3):035454, July 2012. doi: 10.1103/PhysRevB.86.035454. URL http://link.aps.org/doi/10.1103/PhysRevB.86.035454.

[31] Jian-Hua Jiang, Ora Entin-Wohlman, and Yoseph Imry. Thermoelectric three-terminal hopping transport through one-dimensional nanosystems. *Phys. Rev. B*, 85(7):075412, February 2012. doi: 10.1103/PhysRevB.85.075412. URL http://link.aps.org/doi/10.1103/PhysRevB.85.075412.

[32] Jian-Hua Jiang, Ora Entin-Wohlman, and Yoseph Imry. Three-terminal semiconductor junction thermoelectric devices: improving performance. *New J. Phys.*, 15(7):075021, July 2013. ISSN 1367-2630. doi: 10.1088/1367-2630/15/7/075021. URL http://iopscience.iop.org/1367-2630/15/7/075021.

[33] P. Machon, M. Eschrig, and W. Belzig. Nonlocal Thermoelectric Effects and Nonlocal Onsager relations in a Three-Terminal Proximity-Coupled Superconductor-Ferromagnet Device. *Phys. Rev. Lett.*, 110(4):047002, January 2013. doi: 10.1103/PhysRevLett.110.047002. URL http://link.aps.org/doi/10.1103/PhysRevLett.110.047002.

[34] Christian Bergenfeldt, Peter Samuelsson, Björn Sothmann, Christian Flindt, and Markus Büttiker. Hybrid Microwave-Cavity Heat Engine. *Phys. Rev. Lett.*, 112 (7):076803, February 2014. doi: 10.1103/PhysRevLett.112.076803. URL http://link.aps.org/doi/10.1103/PhysRevLett.112.076803.

[35] S. Donsa, S. Andergassen, and K. Held. Double quantum dot as a minimal thermoelectric generator. *Phys. Rev. B*, 89(12):125103, March 2014. doi: 10.1103/PhysRevB.89.125103. URL http://link.aps.org/doi/10.1103/PhysRevB.89.125103.

[36] Francesco Mazza, Riccardo Bosisio, Giuliano Benenti, Vittorio Giovannetti, Rosario Fazio, and Fabio Taddei. Thermoelectric efficiency of three-terminal quantum thermal machines. *New J. Phys.*, 16(8):085001, August 2014. ISSN 1367-2630. doi: 10.1088/1367-2630/16/8/085001. URL http://iopscience.iop.org/1367-2630/16/8/085001.

[37] Francesco Mazza, Stefano Valentini, Riccardo Bosisio, Giuliano Benenti, Vittorio Giovannetti, Rosario Fazio, and Fabio Taddei. Separation of heat and charge currents for boosted thermoelectric conversion. *Phys. Rev. B*, 91(24):245435, June 2015. doi: 10.1103/PhysRevB.91.245435. URL http://link.aps.org/doi/10.1103/PhysRevB.91.245435.

[38] Rafael Sánchez, Björn Sothmann, and Andrew N. Jordan. Chiral Thermoelectrics with Quantum Hall Edge States. *Phys. Rev. Lett.*, 114(14):146801, April 2015. doi: 10.1103/PhysRevLett.114.146801. URL http://link.aps.org/doi/10.1103/PhysRevLett.114.146801.

[39] Rafael Sánchez, Björn Sothmann, and Andrew N. Jordan. Heat diode and engine based on quantum Hall edge states. *New J. Phys.*, 17(7):075006, July 2015. ISSN

1367-2630. doi: 10.1088/1367-2630/17/7/075006. URL http://iopscience.iop.org/1367-2630/17/7/075006.

[40] Patrick P. Hofer and Björn Sothmann. Quantum heat engines based on electronic Mach-Zehnder interferometers. *Phys. Rev. B*, 91(19):195406, May 2015. doi: 10.1103/PhysRevB.91.195406. URL http://link.aps.org/doi/10.1103/PhysRevB.91.195406.

[41] Riccardo Bosisio, Geneviève Fleury, Jean-Louis Pichard, and Cosimo Gorini. Nanowire-based thermoelectric ratchet in the hopping regime. *Phys. Rev. B*, 93 (16):165404, April 2016. doi: 10.1103/PhysRevB.93.165404. URL http://link.aps.org/doi/10.1103/PhysRevB.93.165404.

[42] Barbara Szukiewicz, Ulrich Eckern, and Karol I. Wysokiński. Optimisation of a three-terminal nonlinear heat nano-engine. *New J. Phys.*, 18(2):023050, 2016. ISSN 1367-2630. doi: 10.1088/1367-2630/18/2/023050. URL http://stacks.iop.org/1367-2630/18/i=2/a=023050.

[43] Jian-Hua Jiang and Yoseph Imry. Near-field three-terminal thermoelectric heat engine. *Phys. Rev. B*, 97(12):125422, March 2018. doi: 10.1103/PhysRevB.97.125422. URL https://link.aps.org/doi/10.1103/PhysRevB.97.125422.

[44] Holger Thierschmann, Rafael Sánchez, Björn Sothmann, Fabian Arnold, Christian Heyn, Wolfgang Hansen, Hartmut Buhmann, and Laurens W. Molenkamp. Three-terminal energy harvester with coupled quantum dots. *Nature Nanotech.*, 10(10): 854–858, October 2015. ISSN 1748-3387. doi: 10.1038/nnano.2015.176. URL http://www.nature.com/nnano/journal/v10/n10/full/nnano.2015.176.html.

[45] B. Roche, P. Roulleau, T. Jullien, Y. Jompol, I. Farrer, D. A. Ritchie, and D. C. Glattli. Harvesting dissipated energy with a mesoscopic ratchet. *Nat. Commun.*, 6, April 2015. doi: 10.1038/ncomms7738. URL http://www.nature.com/ncomms/2015/150401/ncomms7738/full/ncomms7738.html.

[46] F. Hartmann, P. Pfeffer, S. Höfling, M. Kamp, and L. Worschech. Voltage Fluctuation to Current Converter with Coulomb-Coupled Quantum Dots. *Phys. Rev. Lett.*, 114 (14):146805, April 2015. doi: 10.1103/PhysRevLett.114.146805. URL http://link.aps.org/doi/10.1103/PhysRevLett.114.146805.

[47] H. L. Edwards, Q. Niu, and A. L. de Lozanne. A quantum-dot refrigerator. *Appl. Phys. Lett.*, 63(13):1815–1817, September 1993. ISSN 00036951. doi: doi:10.1063/1.110672. URL http://apl.aip.org/resource/1/applab/v63/i13/p1815_s1.

[48] H. L. Edwards, Q. Niu, G. A. Georgakis, and A. L. de Lozanne. Cryogenic cooling using tunneling structures with sharp energy features. *Phys. Rev. B*, 52(8):5714–5736, 1995. doi: 10.1103/PhysRevB.52.5714. URL http://link.aps.org/doi/10.1103/PhysRevB.52.5714.

[49] J. R. Prance, C. G. Smith, J. P. Griffiths, S. J. Chorley, D. Anderson, G. A. C. Jones, I. Farrer, and D. A. Ritchie. Electronic Refrigeration of a Two-Dimensional Electron Gas. *Phys. Rev. Lett.*, 102(14):146602, April 2009. doi: 10.1103/PhysRevLett.102.146602. URL http://link.aps.org/doi/10.1103/PhysRevLett.102.146602.

[50] CG Smith. Low-dimensional quantum devices. *Reports on Progress in Physics*, 59(2): 235, 1996.

[51] Ian Farrer. In *Thesis: Growth and Application of Self-Assemble Quantum Dots*, page 4. University of Cambridge, 2001.

[52] K v Klitzing, Gerhard Dorda, and Michael Pepper. New method for high-accuracy determination of the fine-structure constant based on quantized hall resistance. *Physical Review Letters*, 45(6):494, 1980.

[53] D. C. Tsui, H. L. Stormer, and A. C. Gossard. Two-dimensional magnetotransport in the extreme quantum limit. *Phys. Rev. Lett.*, 48:1559–1562, May 1982. doi: 10.1103/PhysRevLett.48.1559. URL https://link.aps.org/doi/10.1103/PhysRevLett.48.1559.

[54] B. J. Van Wees, H. van Houten, C. W. J. Beenakker, J. G. Williamson, L. P. Kouwenhoven, D. van der Marel, and C. T. Foxon. Quantized conductance of point contacts in a two-dimensional electron gas. *Phys. Rev. Lett.*, 60:848–850, Feb 1988. doi: 10.1103/PhysRevLett.60.848. URL https://link.aps.org/doi/10.1103/PhysRevLett.60.848.

[55] DA Wharam, Trevor John Thornton, R Newbury, M Pepper, H Ahmed, JEF Frost, DG Hasko, DC Peacock, DA Ritchie, and GAC Jones. One-dimensional transport and the quantisation of the ballistic resistance. *Journal of Physics C: solid state physics*, 21(8):L209, 1988.

[56] CG Smith, M Pepper, H Ahmed, JEF Frost, DG Hasko, DC Peacock, DA Ritchie, and GAC Jones. The transition from one-to zero-dimensional ballistic transport. *Journal of Physics C: Solid State Physics*, 21(24):L893, 1988.

[57] BJ Van Wees, Leo P Kouwenhoven, CJPM Harmans, JG Williamson, CE Timmering, MEI Broekaart, CT Foxon, and JJ Harris. Observation of zero-dimensional states in a one-dimensional electron interferometer. *Physical Review Letters*, 62(21):2523, 1989.

[58] U Meirav, MA Kastner, and SJ Wind. Single-electron charging and periodic conductance resonances in gaas nanostructures. *Physical review letters*, 65(6):771, 1990.

[59] MA Reed, JN Randall, RJ Aggarwal, RJ Matyi, TM Moore, and AE Wetsel. Observation of discrete electronic states in a zero-dimensional semiconductor nanostructure. *Physical Review Letters*, 60(6):535, 1988.

[60] Marc A Kastner. The single-electron transistor. *Reviews of modern physics*, 64(3): 849, 1992.

[61] U Meirav and EB Foxman. Single-electron phenomena in semiconductors. *Semiconductor Science and Technology*, 11(3):255, 1996.

[62] Leo P Kouwenhoven, Charles M Marcus, Paul L McEuen, Seigo Tarucha, Robert M Westervelt, and Ned S Wingreen. Electron transport in quantum dots. In *Mesoscopic Electron Transport*, pages 105–214. Springer, 1997.

[63] Wilfred G Van der Wiel, Silvano De Franceschi, Jeroen M Elzerman, Toshimasa Fujisawa, Seigo Tarucha, and Leo P Kouwenhoven. Electron transport through double quantum dots. *Reviews of Modern Physics*, 75(1):1, 2002.

[64] Ronald Hanson, Leo P Kouwenhoven, Jason R Petta, Seigo Tarucha, and Lieven MK Vandersypen. Spins in few-electron quantum dots. *Reviews of Modern Physics*, 79(4): 1217, 2007.

[65] LP Kouwenhoven, NC Van der Vaart, AT Johnson, W Kool, CJPM Harmans, JG Williamson, AAM Staring, and CT Foxon. Single electron charging effects in semiconductor quantum dots. *Zeitschrift für Physik B Condensed Matter*, 85(3): 367–373, 1991.

[66] Seigo Tarucha, DG Austing, T Honda, RJ Van der Hage, and Leo P Kouwenhoven. Shell filling and spin effects in a few electron quantum dot. *Physical Review Letters*, 77(17):3613, 1996.

[67] CWJ Beenakker. Theory of coulomb-blockade oscillations in the conductance of a quantum dot. *Physical Review B*, 44(4):1646, 1991.

[68] DV Averin, AN Korotkov, and KK Likharev. Theory of single-electron charging of quantum wells and dots. *Physical Review B*, 44(12):6199, 1991.

[69] John H Davies. *The physics of low-dimensional semiconductors: an introduction*. Cambridge university press, 1998.

[70] EB Foxman, U Meirav, PL McEuen, MA Kastner, O Klein, PA Belk, DM Abusch, and SJ Wind. Crossover from single-level to multilevel transport in artificial atoms. *Physical Review B*, 50(19):14193, 1994.

[71] DV Averin and Yu V Nazarov. Virtual electron diffusion during quantum tunneling of the electric charge. *Physical Review Letters*, 65(19):2446, 1990.

[72] LJ Geerligs, DV Averin, and JE Mooij. Observation of macroscopic quantum tunneling through the coulomb energy barrier. *Physical Review Letters*, 65(24):3037, 1990.

[73] S De Franceschi, S Sasaki, JM Elzerman, WG Van Der Wiel, S Tarucha, and Leo P Kouwenhoven. Electron cotunneling in a semiconductor quantum dot. *Physical Review Letters*, 86(5):878, 2001.

[74] Sara M Cronenwett, Tjerk H Oosterkamp, and Leo P Kouwenhoven. A tunable kondo effect in quantum dots. *Science*, 281(5376):540–544, 1998.

[75] J Kondo. Solid state physics vol 23 ed f seitz. *D Turnbull and H Ehrenreich (New York: Academic) p*, 183, 1969.

[76] David Goldhaber-Gordon, Hadas Shtrikman, D Mahalu, David Abusch-Magder, U Meirav, and MA Kastner. Kondo effect in a single-electron transistor. *Nature*, 391(6663):156, 1998.

[77] Jörg Schmid, Jürgen Weis, Karl Eberl, and Klaus v Klitzing. A quantum dot in the limit of strong coupling to reservoirs. *Physica B: Condensed Matter*, 256:182–185, 1998.

[78] Luke William Smith. *Electron interaction effects in quasi-one-dimensional quantum wires*. PhD thesis, University of Cambridge, 2012.

[79] M Büttiker, Y Imry, R Landauer, and S Pinhas. Generalized many-channel conductance formula with application to small rings. *Physical Review B*, 31(10):6207, 1985.

[80] Y Imry. Directions in condensed matter physics, 1986.

[81] KJ Thomas, JT Nicholls, MY Simmons, M Pepper, DR Mace, and DA Ritchie. Possible spin polarization in a one-dimensional electron gas. *Physical Review Letters*, 77(1):135, 1996.

[82] KJ Thomas, JT Nicholls, NJ Appleyard, MY Simmons, M Pepper, DR Mace, WR Tribe, and DA Ritchie. Interaction effects in a one-dimensional constriction. *Physical Review B*, 58(8):4846, 1998.

[83] AP Micolich. What lurks below the last plateau: experimental studies of the $0.7 \times 2e^2/h$ conductance anomaly in one-dimensional systems. *Journal of Physics: Condensed Matter*, 23(44):443201, 2011.

[84] Elliott Lieb and Daniel Mattis. Theory of ferromagnetism and the ordering of electronic energy levels. In *Inequalities*, pages 33–41. Springer, 2002.

[85] KJ Thomas, JT Nicholls, M Pepper, WR Tribe, MY Simmons, and DA Ritchie. Spin properties of low-density one-dimensional wires. *Physical Review B*, 61(20):R13365, 2000.

[86] Sebastien Nuttinck, Katsushi Hashimoto, Sen Miyashita, Tadashi Saku, Yoshihisa Yamamoto, and Yoshiro Hirayama. Quantum point contacts in a density-tunable two-dimensional electron gas. *Japanese Journal of Applied Physics*, 39(7A):L655, 2000.

[87] David J Reilly, Geoffrey R Facer, Andrew S Dzurak, BE Kane, RG Clark, PJ Stiles, AR Hamilton, Jeremy L O'Brien, Nancy E Lumpkin, Loren N Pfeiffer, et al. Many-body spin-related phenomena in ultra low-disorder quantum wires. *Physical Review B*, 63(12):121311, 2001.

[88] KS Pyshkin, CJB Ford, RH Harrell, M Pepper, EH Linfield, and DA Ritchie. Spin splitting of one-dimensional subbands in high quality quantum wires at zero magnetic field. *Physical Review B*, 62(23):15842, 2000.

[89] DJ Reilly. Phenomenological model for the 0.7 conductance feature in quantum wires. *Physical Review B*, 72(3):033309, 2005.

[90] Neil Turner. *Tunnelling spectroscopy in GaAs/AlGaAs double quantum well devices*. PhD thesis, University of Cambridge, 1996.

[91] TJ Gramila, JP Eisenstein, AH MacDonald, LN Pfeiffer, and KW West. Electron-electron scattering between parallel two-dimensional electron gases. *Surface Science*, 263(1-3):446–450, 1992.

[92] LW Smith, AR Hamilton, KJ Thomas, M Pepper, I Farrer, JP Griffiths, GAC Jones, and DA Ritchie. Compressibility measurements of quasi-one-dimensional quantum wires. *Physical Review Letters*, 107(12):126801, 2011.

[93] JA Simmons, SK Lyo, NE Harff, and JF Klem. Conductance modulation in double quantum wells due to magnetic field-induced anticrossing. *Physical Review Letters*, 73(16):2256, 1994.

[94] JP Eisenstein, GS Boebinger, LN Pfeiffer, KW West, and Song He. New fractional quantum hall state in double-layer two-dimensional electron systems. *Physical Review Letters*, 68(9):1383, 1992.

[95] N Turner, JT Nicholls, EH Linfield, KM Brown, GAC Jones, and DA Ritchie. Tunneling between parallel two-dimensional electron gases. *Physical Review B*, 54(15): 10614, 1996.

[96] Lian Zheng and AH MacDonald. Tunneling conductance between parallel two-dimensional electron systems. *Physical Review B*, 47(16):10619, 1993.

[97] JP Eisenstein, TJ Gramila, LN Pfeiffer, and KW West. Probing a two-dimensional fermi surface by tunneling. *Physical Review B*, 44(12):6511, 1991.

[98] Elizabeth Johnson et al. Low-dimensional semiconductor structures: Fundamentals and device applications; page 303. 2001.

[99] Alex L Efros and Michael Pollak. *Electron-electron interactions in disordered systems*, volume 10. Elsevier, 2012.

[100] AG Huibers, M Switkes, CM Marcus, K Campman, and AC Gossard. Dephasing in open quantum dots. *Physical Review Letters*, 81(1):200, 1998.

[101] Lian Zheng and S Das Sarma. Coulomb scattering lifetime of a two-dimensional electron gas. *Physical Review B*, 53(15):9964, 1996.

[102] T Jungwirth and AH MacDonald. Electron-electron interactions and two-dimensional–two-dimensional tunneling. *Physical Review B*, 53(11):7403, 1996.

[103] Gabriele F Giuliani and John J Quinn. Lifetime of a quasiparticle in a two-dimensional electron gas. *Physical Review B*, 26(8):4421, 1982.

[104] A Yacoby, M Heiblum, Hadas Shtrikman, V Umansky, and D Mahalu. Dephasing of ballistic electrons as a function of temperature and carrier density. *Semiconductor Science and Technology*, 9(5S):907, 1994.

[105] AG Huibers, JA Folk, SR Patel, CM Marcus, CI Duruöz, and JS Harris Jr. Low-temperature saturation of the dephasing time and effects of microwave radiation on open quantum dots. *Physical Review Letters*, 83(24):5090, 1999.

[106] SQ Murphy, JP Eisenstein, LN Pfeiffer, and KW West. Lifetime of two-dimensional electrons measured by tunneling spectroscopy. *Physical Review B*, 52(20):14825, 1995.

[107] Neil W Ashcroft, N David Mermin, et al. Solid state physics [by] neil w. ashcroft [and] n. david mermin., 1976.

[108] U Sivan, M Heiblum, and CP Umbach. Hot ballistic transport and phonon emission in a two-dimensional electron gas. *Physical Review Letters*, 63(9):992, 1989.

[109] Keith Barnham and Dimitri Vvedensky. *Low-dimensional semiconductor structures: Fundamentals and device applications*. Cambridge University Press, 2008.

[110] Peter J Price. Hot electrons in a gaas heterolayer at low temperature. *Journal of Applied Physics*, 53(10):6863–6866, 1982.

[111] Andreas Knäbchen. Transport relaxation rate of a two-dimensional electron gas: Surface acoustic-phonon contribution. *Physical Review B*, 55(11):6701, 1997.

[112] YY Proskuryakov, JT Nicholls, DI Hadji-Ristic, A Kristensen, and CB Sørensen. Energy-loss rate of a two-dimensional electron gas measured using a mesoscopic thermometer. *Physical Review B*, 75(4):045308, 2007.

[113] HL Stormer, LN Pfeiffer, KW Baldwin, and KW West. Observation of a bloch-grüneisen regime in two-dimensional electron transport. *Physical Review B*, 41(2): 1278, 1990.

[114] BK Ridley. Hot electrons in low-dimensional structures. *Reports on Progress in Physics*, 54(2):169, 1991.

[115] Cz Jasiukiewicz and V Karpus. Electron energy relaxation rate: the influence of acoustic phonon spectrum anisotropy. *Semiconductor Science and Technology*, 11(12): 1777, 1996.

[116] NJ Appleyard, JT Nicholls, MY Simmons, WR Tribe, and M Pepper. Thermometer for the 2d electron gas using 1d thermopower. *Physical Review Letters*, 81(16):3491, 1998.

[117] A Mittal, RJ Zieve, DE Prober, RG Wheeler, and RN Sacks. Electron-phonon scattering and heat flow in gaas/algaas 2deg samples below 0.5 k. In *APS March Meeting Abstracts*, 1996.

[118] FF Ouali, HR Francis, and HC Rhodes. Acoustic phonon scattering in two dimensional carriers. *Physica B: Condensed Matter*, 263:239–242, 1999.

[119] O Chiatti, JT Nicholls, YY Proskuryakov, N Lumpkin, I Farrer, and DA Ritchie. Quantum thermal conductance of electrons in a one-dimensional wire. *Physical Review Letters*, 97(5):056601, 2006.

[120] R Scheibner, M König, D Reuter, AD Wieck, C Gould, H Buhmann, and LW Molenkamp. Quantum dot as thermal rectifier. *New Journal of Physics*, 10 (8):083016, 2008.

[121] AAM Staring, LW Molenkamp, BW Alphenaar, H Van Houten, OJA Buyk, MAA Mabesoone, CWJ Beenakker, and CT Foxon. Coulomb-blockade oscillations in the thermopower of a quantum dot. *EPL (Europhysics Letters)*, 22(1):57, 1993.

[122] L Molenkamp, AAM Staring, BW Alphenaar, H Van Houten, and CWJ Beenakker. Sawtooth-like thermopower oscillations of a quantum dot in the coulomb blockade regime. *Semiconductor Science and Technology*, 9(5S):903, 1994.

[123] AS Dzurak, CG Smith, CHW Barnes, M Pepper, L Martín-Moreno, CT Liang, DA Ritchie, and GAC Jones. Thermoelectric signature of the excitation spectrum of a quantum dot. *Physical Review B*, 55(16):R10197, 1997.

[124] AS Dzurak, CG Smith, L Martin-Moreno, M Pepper, DA Ritchie, GAC Jones, and DG Hasko. Thermopower of a one-dimensional ballistic constriction in the non-linear regime. *Journal of Physics: Condensed Matter*, 5(43):8055, 1993.

[125] Rolf Landauer. Spatial variation of currents and fields due to localized scatterers in metallic conduction. *IBM Journal of Research and Development*, 1(3):223–231, 1957.

[126] M Büttiker. Four-terminal phase-coherent conductance. *Physical Review Letters*, 57 (14):1761, 1986.

[127] H Van Houten, LW Molenkamp, CWJ Beenakker, and CT Foxon. Thermo-electric properties of quantum point contacts. *Semiconductor Science and Technology*, 7(3B): B215, 1992.

[128] U Sivan and Y Imry. Multichannel landauer formula for thermoelectric transport with application to thermopower near the mobility edge. *Physical Review B*, 33(1):551, 1986.

[129] PN Butcher. Thermal and electrical transport formalism for electronic microstructures with many terminals. *Journal of Physics: Condensed Matter*, 2(22):4869, 1990.

[130] X Zianni. Coulomb oscillations in the electron thermal conductance of a dot in the linear regime. *Physical Review B*, 75(4):045344, 2007.

[131] Björn Kubala, Jürgen König, and Jukka Pekola. Violation of the wiedemann-franz law in a single-electron transistor. *Physical Review Letters*, 100(6):066801, 2008.

[132] SF Godijn, S Möller, H Buhmann, LW Molenkamp, and SA Van Langen. Thermopower of a chaotic quantum dot. *Physical Review Letters*, 82(14):2927, 1999.

[133] M Tsaousidou and GP Triberis. Thermoelectric properties of a weakly coupled quantum dot: Enhanced thermoelectric efficiency. *Journal of Physics: Condensed Matter*, 22(35):355304, 2010.

[134] Mariusz Krawiec and Karol I Wysokiński. Thermoelectric effects in strongly interacting quantum dot coupled to ferromagnetic leads. *Physical Review B*, 73(7):075307, 2006.

[135] Maxim G Vavilov and A Douglas Stone. Failure of the wiedemann-franz law in mesoscopic conductors. *Physical Review B*, 72(20):205107, 2005.

[136] Paolo Andrea Erdman, Francesco Mazza, Riccardo Bosisio, Giuliano Benenti, Rosario Fazio, and Fabio Taddei. Thermoelectric properties of an interacting quantum dot based heat engine. *Physical Review B*, 95(24):245432, 2017.

[137] Markus Buttiker. Coherent and sequential tunneling in series barriers. *IBM Journal of Research and Development*, 32(1):63–75, 1988.

[138] Jonathan Robert Prance. *Cooling an electron gas using quantum dot based electronic refrigeration*. PhD thesis, University of Cambridge, 2009.

[139] RP Taylor, PT Coleridge, M Davies, Y Feng, JP McCaffrey, and PA Marshall. Physical and electrical investigation of ohmic contacts to algaas/gaas heterostructures. *Journal of Applied Physics*, 76(12):7966–7972, 1994.

[140] A. Mittal, R. G. Wheeler, M. W. Keller, D. E. Prober, and R. N. Sacks. Electron-phonon scattering rates in GaAs/AlGaAs 2deg samples below 0.5 K. *Surf. Sci.*, 361-362:537–541, July 1996. ISSN 0039-6028. doi: 10.1016/0039-6028(96)00464-5. URL http://www.sciencedirect.com/science/article/pii/0039602896004645.

[141] Bivas Dutta, Joonas T Peltonen, Daniil S Antonenko, Matthias Meschke, Mikhail A Skvortsov, Björn Kubala, Jürgen König, Clemens B Winkelmann, Herve Courtois, and Jukka P Pekola. Thermal conductance of a single-electron transistor. *Physical Review Letters*, 119(7):077701, 2017.

[142] Effendi Leobandung, Lingjie Guo, Yun Wang, and Stephen Y Chou. Observation of quantum effects and coulomb blockade in silicon quantum-dot transistors at temperatures over 100 k. *Applied physics letters*, 67(7):938–940, 1995.

[143] Jiwoong Park, Abhay N Pasupathy, Jonas I Goldsmith, Connie Chang, Yuval Yaish, Jason R Petta, Marie Rinkoski, James P Sethna, Héctor D Abruña, Paul L McEuen, et al. Coulomb blockade and the kondo effect in single-atom transistors. *Nature*, 417 (6890):722, 2002.

[144] A Mavalankar, SJ Chorley, J Griffiths, GAC Jones, I Farrer, DA Ritchie, and CG Smith. A non-invasive electron thermometer based on charge sensing of a quantum dot. *Applied Physics Letters*, 103(13):133116, 2013.

[145] EB Foxman, PL McEuen, U Meirav, Ned S Wingreen, Yigal Meir, Paul A Belk, NR Belk, MA Kastner, and SJ Wind. Effects of quantum levels on transport through a coulomb island. *Physical Review B*, 47(15):10020, 1993.

[146] M Field, CG Smith, M Pepper, DA Ritchie, JEF Frost, GAC Jones, and DG Hasko. Measurements of coulomb blockade with a noninvasive voltage probe. *Physical Review Letters*, 70(9):1311, 1993.

[147] S Gasparinetti, MJ Martínez-Pérez, S De Franceschi, Jukka P Pekola, and F Giazotto. Nongalvanic thermometry for ultracold two-dimensional electron domains. *Applied Physics Letters*, 100(25):253502, 2012.

[148] Rolf Landauer. R. landauer, ibm j. res. dev. 32, 306 (1988). *IBM J. Res. Dev.*, 32:306, 1988.

[149] M Büttiker. Quantized transmission of a saddle-point constriction. *Physical Review B*, 41(11):7906, 1990.

[150] J Smoliner, E Gornik, and G Weimann. Depletion charge measurements by tunneling spectroscopy gaas-gaalas field-effect transistors. *Applied Physics Letters*, 52(25): 2136–2138, 1988.

[151] W Demmerle, J Smoliner, G Berthold, E Gornik, G Weimann, and W Schlapp. Tunneling spectroscopy in barrier-separated two-dimensional electron-gas systems. *Physical Review B*, 44(7):3090, 1991.

[152] JP Eisenstein, LN Pfeiffer, and KW West. Independently contacted two-dimensional electron systems in double quantum wells. *Applied Physics Letters*, 57(22):2324–2326, 1990.

[153] KJ Thomas, JT Nicholls, MY Simmons, WR Tribe, AG Davies, and M Pepper. Controlled wave-function mixing in strongly coupled one-dimensional wires. *Physical Review B*, 59(19):12252, 1999.

[154] IM Castleton, AG Davies, AR Hamilton, JEF Frost, MY Simmons, DA Ritchie, and M Pepper. Closely separated one-dimensional wires:: coupled ballistic conduction, wave function hybridization and compressibility investigations. *Physica B: Condensed Matter*, 249:157–161, 1998.

[155] KJ Thomas, JT Nicholls, WR Tribe, MY Simmons, AG Davies, DA Ritchie, and M Pepper. Bonding and antibonding states in strongly coupled ballistic one-dimensional wires. *Physica E: Low-dimensional Systems and Nanostructures*, 6(1-4): 581–585, 2000.

[156] Nicholas Howard Balshaw. *Practical cryogenics: an introduction to laboratory cryogenics*. Oxford Instruments, Scientific Research Division, 1996.

Appendix A

The wafer details

A.1 The Wafer W0923

The details of the wafer W0923 used in Chapter 3 are given below. The assessment data is also shown, which includes the carrier density and mobility measured at 1.4 K, in the dark and in the light (after strong illumination with a red LED).

Layer	Material	Thickness (nm)	Doping (cm^{-3})	Description
1	GaAs	10	-	Capping layer
2	AlGaAs	40	7×10^{18}	Doping layer
3	AlGaAs	60	-	Spacer
4	GaAs	1000	-	Buffer
5	GaAs	2.5	-	-
6	AlGaAs	2.5	-	-
7	GaAs	500	-	-
8	AlAs	50	-	
9	GaAs	50	-	

Table A.1 Structure of the wafer W0923.

n_{2D} dark	$1.4 \times 10^{11}\ cm^{-2}$	μ dark	$3.32 \times 10^{6}\ cm^{2}V^{-1}s^{-1}$
n_{2D} light	$2.6 \times 10^{11}\ cm^{-2}$	μ light	$6.19 \times 10^{6}\ cm^{2}V^{-1}s^{-1}$

Table A.2 W0923 assessment data: Carrier density mobility of both layers measured simultaneously, in the dark and light.

A.2 The Wafer W0187

The details of the wafer W0187 used in Chapter 5 are given below. The assessment data is also shown, which includes the carrier density and mobility measured at 1.4 K, in the dark and in the light (after strong illumination with a red LED).

Layer	Material	Thickness (nm)	Doping (cm^{-3})	Description
1	GaAs	10	-	Capping layer
2	AlGaAs	200	7×10^{16}	Doping layer
3	AlGaAs	75	-	Spacer
4	GaAs	15	-	Quantum well
5	AlGaAs	30	-	Barrier
6	GaAs	15	-	Quantum well
7	AlGaAs	75	-	Spacer
8	AlGaAs	200	7×10^{16}	Doping layer
9	AlGaAs	250	-	Lower barrier (33% Al)
10	AlGaAs	250	-	Graded AlGaAs (5% Al to 33% Al)
11	GaAs	1000	-	Buffer
12	AlAs	50	-	
13	GaAs	50	-	
	SI GaAs	500 μm		Substrate

Table A.3 Structure of DQW wafer W0187.

n_{2D} dark	2.4×10^{11} cm^{-2}	μ dark	2.2×10^{6} $cm^2V^{-1}s^{-1}$
n_{2D} light	3.7×10^{11} cm^{-2}	μ light	3.1×10^{6} $cm^2V^{-1}s^{-1}$

Table A.4 W0187 assessment data: Carrier density mobility of both layers measured simultaneously, in the dark and light.

Appendix B

A Dilution Refrigerator

The measurements detailed in Chapter 3 and 4 were made at extremely low temperatures in a ^{3}He/^{4}He dilution refrigerator. Since this set up is critical to the measurements performed, this appendix outlines the working of a dilution fridge. The brief explanation below is taken from the manual by N.H.Balshow [156].

When a mixture of the two stable isotopes of helium is cooled below a critical temperature it separates into two phases. The lighter 'concentrated phase' is rich in ^{3}He and the heavier 'dilute phase' is rich in ^{4}He. The concentration of He in each phase depends upon the temperature. Since the enthalpy of the He in the two phases is different, it is possible to obtain cooling by 'evaporating' the He from the concentrated phase into the dilute phase boundary. This process continues to work even at the lowest temperatures because the equilibrium concentration of He in the dilute phase is still finite, even as the temperature approaches absolute zero. However, the base temperature is limited by other factors, and in particular by the residual heat leak and heat exchanger performance.

When the refrigerator is started the 1 K pot is used to condense the ^{3}He/^{4}He mixture into the dilution unit. It is not intended to cool the mixture enough to set up the phase boundary but only to cool it to 1.2 K. In order to get phase separation, the temperature must be reduced to below 0.86 K (the tri-critical point). The still is the first part of the fridge to cool below 1.2 K. It cools the incoming He before it enters the heat exchangers and the mixing chamber, and phase separation typically occurs after a few minutes. Gradually, the rest of the dilution unit is cooled to the point where phase separation occurs.

In a continuously operating system, the He must be extracted from the dilution phase (to prevent it from saturating) and returned into the concentrated phase keeping the system in a dynamic equilibrium. Figure B shows a schematic diagram of a typical continuously operating dilution refrigerator. The He is pumped away from the liquid surface in the still,

which is typically maintained at a temperature of 0.6 to 1.7 K. At this temperature the vapour pressure of the ^{3}He is about 1000 times higher than that of ^{4}He, so ^{3}He evaporates preferentially. A small amount of heat is supplied to the still to promote the required flow.

The concentration of the He in the dilute phase in the still therefore becomes lower than it is in the mixing chamber, and the osmotic pressure difference drives a flow of ^{3}He to the still. The He leaving the mixing chamber is used to cool the returning flow of concentrated ^{3}He in a series of heat exchangers.

The room temperature vacuum pumping system is used to remove the ^{3}He from the still, and the compress it to a pressure of a few hundred millibar. The gas is then passed through filters and cold traps to remove impurities and returned to the cryostat, where it is pre-cooled in the main helium bath and condensed on the 1 K pot. The primary impedence is used to maintain a high enough pressure in the 1 K pot region for the gas to condense. The experimental apparatus is mounted on or inside the mixing chamber, ensuring that it is in good thermal contact with the dilute phase. All connections to the room temperature equipment must be thermally anchored at various points on the refrigerator to reduce the heat load on the mixing chamber and give the lowest possible base temperature.

The 1K pot system shown at the left top corner of the figure B.1 can reach down to 1.5 K while changing the pressure in the pot via pumping the helium through the 1K pot pump. This is the main principal of the 10T cryostat system used in Chapter 5.

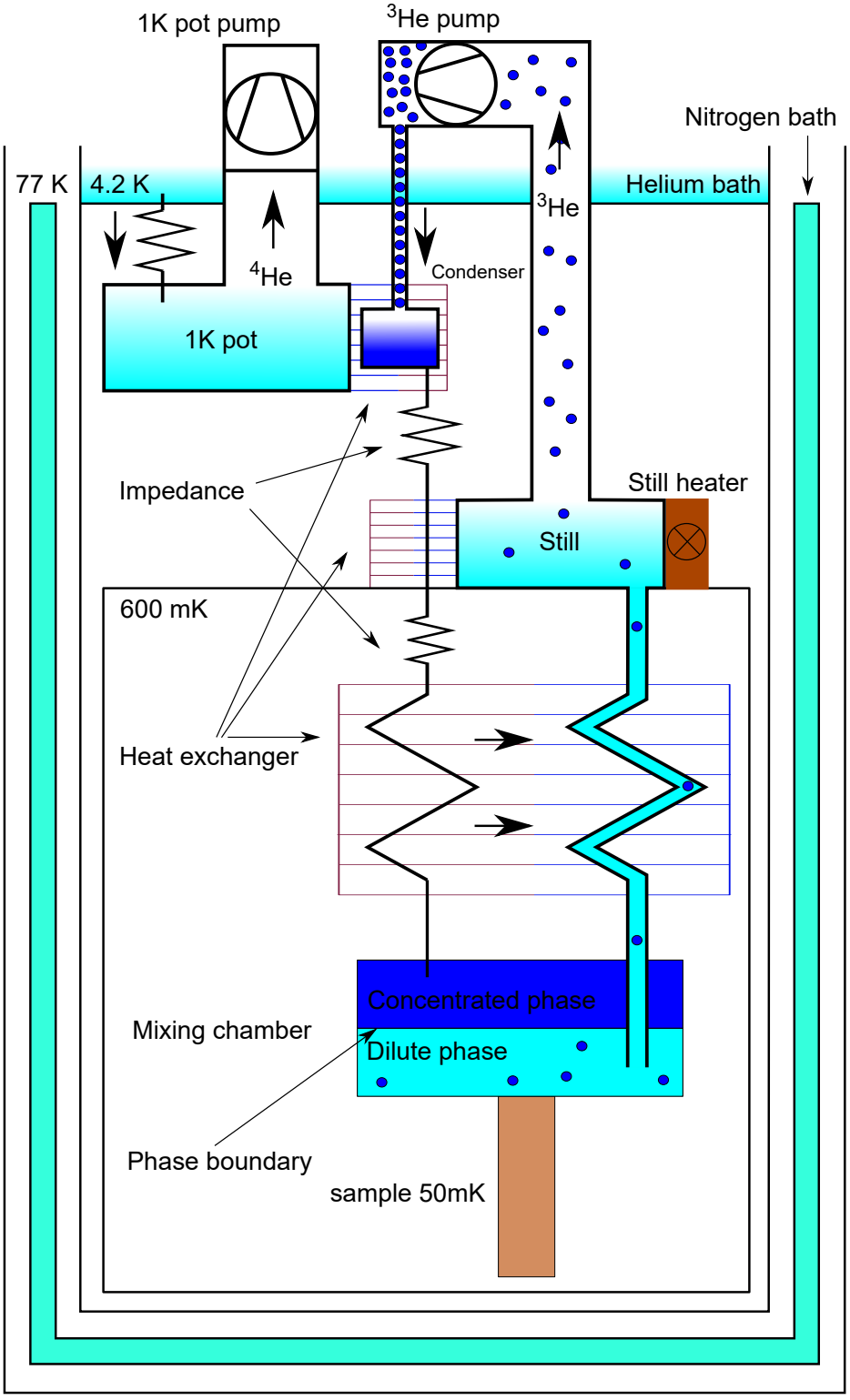

Fig. B.1 Schematic Diagram of a wet ^{3}He/^{4}He dilution refrigerator.